

**Quantitative Characterization of Magnetic Domain Structure
in Near Eutectoid Co₄₀Pt₆₀ Alloys**

Submitted in partial fulfillment of the requirements for
the degree of
Doctor of Philosophy
in
Materials Science and Engineering

Isha Kashyap

Dual Degree (B.Tech and M.Tech), Metallurgical and Materials Engineering, Indian
Institute of Technology Kharagpur
M.S., Materials Science and Engineering, Carnegie Mellon University

Carnegie Mellon University
Pittsburgh, PA

August, 2018

Abstract

Characterization of magnetic domain structure is essential to understand and manipulate the magnetic properties of materials. In this thesis, we have utilized Lorentz Transmission Electron Microscopy (LTEM) in combination with image simulations based on micromagnetic models, to investigate the magnetic domain structure of a unique nano-chessboard structure consisting of $L1_0$ and $L1_2$ phases in a $Co_{40}Pt_{60}$ alloy. We have shown high-resolution LTEM images of nano-size magnetic features acquired through spherical aberration correction in Lorentz Fresnel mode. Phase reconstructions based on the transport of intensity equation has been carried out to fully understand the magnetic domain structure and to extract quantitative information, including direction of magnetic induction and magnetic domain wall width, from the Lorentz TEM images. The experimental Fresnel images of the nano-chessboard structure show zig-zag shaped magnetic domain walls at the inter-phase boundaries between $L1_0$ and $L1_2$ phases. A circular magnetization distribution with vortex and anti-vortex type arrangement is evident in the phase reconstructed magnetic induction maps as well as simulated maps. The magnetic contrast in experimental LTEM images has been properly interpreted with the help of magnetic induction maps simulated for various relative electron beam-sample orientations inside TEM. Apart from the nano-chessboard structure, this alloy shows other interesting microstructural features such as anti-phase boundaries, tweed structure, coarse $L1_0$ plates, and macro-twins all of which have been characterized using conventional bright field/dark field TEM imaging and compared with

their respective Lorentz TEM images. The magnetic domain wall widths obtained for each microstructure has been compared and the influence of microstructure and the particle size on wall widths has been discussed.

Acknowledgements

First and foremost I would like to thank my advisor, Prof. Marc De Graef, without whom this work would not be possible. I am very grateful for his constant support throughout my research and for always encouraging me to do better. I am especially thankful to him for motivating and guiding me through the computational part of my work.

I sincerely acknowledge the financial support for this research work from the department of Materials Science and Engineering at Carnegie Mellon University and the National Science Foundation under grant no. DMR-1564550. I would like to thank my thesis committee members, Prof. David E. Laughlin, Prof. Yoosuf N. Picard, and Dr. Charudatta Phatak for agreeing to be in committee and for providing valuable suggestions to improve my thesis. I learnt a lot from Prof. Laughlin's courses on magnetism, phase transformations, and microstructures. Prof. Picard personally guided me while working on another project during this research period. I really appreciate the insight he shared with me on TEM, FIB, and ECCI imaging. I am also grateful to Dr. Phatak for providing useful suggestions regarding diffraction analysis in Lorentz mode. I would like to thank Prof. Jerrold A. Floro and his research group for providing us the samples and for sharing valuable suggestions.

I consider myself very fortunate to have received training on all the electron microscopy techniques by an expert in the field and a wonderful person, Tom Nuhfer. He assisted me with these techniques whenever I was in trouble, which, unfortunately, was very often. I am deeply grateful for the time he spent in helping me with aberration correction on Titan. His immense knowledge about different sample preparation techniques also helped me greatly throughout my research. The dedication and interest he shows in trying to understand and help solve a student's problem is highly commendable. I am grateful to Marygrace, Kelly, and Suzy for helping me sort with an innumerable amount of things in a timely manner. I take this opportunity to thank all the MSE faculty and staff.

I would like to offer my sincerest thank to my friend and inspiration Dr. Farangis Ram. Her advices on both my work and personal life have always been helpful. I also want to thank Dr. Saransh, Dr. Prabhat, and Dr. Ryan for being there for me everytime I was stuck on a computational problem. I want to thank other group members Ke-Wei, Maxwell, Joseph, Will, Mike, and Shan for all the helpful conversations and for all the good memories.

Finally, I would like to thank all of my family members and my partner, Abhinav, in this long journey for their immense support throughout my research.

List of Publications

The following papers related to the work presented in this document have been submitted or are being prepared:

1. Isha Kashyap, Yongmei M. Jin, Eric P. Vetter, Jerrold A. Floro, and Marc De Graef, Lorentz Transmission Electron Microscopy Image Simulations of Experimental Nano-Chessboard Observations in Co-Pt Alloys, *Microscopy and Microanalysis* (2018).
2. Isha Kashyap and Marc De Graef, “Magnetic microstructure studies in near-eutectoid Co-Pt alloys using Lorentz TEM”, *Journal of Magnetism and Magnetic Materials* (2018 (in preparation)).

Table of Contents

Abstract	ii
Acknowledgements	iv
List of Publications	vi
List of Tables	ix
List of Figures	x
1 Introduction	1
1.1 Motivation	1
1.2 Hypothesis	5
1.3 Experimental Design.....	7
1.3.1 Experimental techniques.....	7
1.3.2 Simulation technique	7
1.3.3 Material	8
1.4 Document Organization	9
2 Phase Transformations and Domain Structures in Co-Pt Alloys.....	10
2.1 Introduction	10
2.2 Atomic Ordering Transformation.....	11
2.2.1 Phase diagram of binary Co-Pt alloy	13
2.2.2 Crystal structure of L1 ₀ and L1 ₂ ordered phases.....	15
2.2.3 Eutectoid phase transformation in Co-Pt alloys	20
2.2.4 Evolution of microstructure.....	24
2.3 Magnetic Ordering Transformation	30
2.3.1 Magnetic moment and magnetization.....	31
2.3.2 Micro-magnetic theory and magnetic domains	33
2.3.3 Exchange coupling in two phase nano-composites.....	45
2.3.4 Magnetic microstructure in L1 ₀ alloys	47
3 Experimental and Simulation Techniques.....	51
3.1 Introduction	51
3.2 Transmission Electron Microscopy.....	52
3.3 Lorentz Transmission Electron Microscopy.....	56
3.3.1 Classical approach to Lorentz microscopy	56
3.3.2 Lorentz Fresnel imaging	58
3.3.3 Quantum mechanical approach to Lorentz microscopy.....	61
3.4 Lorentz Image Simulation.....	63
3.4.1 Computation of magnetic phase shift.....	63
3.4.2 Simulation of magnetic induction maps	69

3.4.3	Lorentz image simulations	70
3.5	Phase Reconstruction Theory	73
3.6	Spherical Aberration Corrected Lorentz Microscopy.....	76
4	Magnetic Domain Structure of Co₄₀Pt₆₀ Alloy	79
4.1	Introduction	79
4.2	Conventional TEM Imaging	80
4.3	Magnetic Domain Structure.....	88
4.4	Magnetic Domain Walls in the Nano-chessboard Structure.....	104
4.5	Phase Shift Simulation of Nano-chessboards.....	114
4.5.1	Micro-magnetic simulations methodology	114
4.5.2	Magnetic contrast at zero beam tilt	115
4.5.3	Beam tilt effect on magnetic contrast	118
4.6	Comparison of Experimental and Simulated Images	120
4.7	Domain Wall Width Measurement from Lorentz Fresnel Images.....	123
4.7.1	Methodology.....	123
4.7.2	Domain wall width results	125
5	Conclusions and Future Work	132
5.1	Conclusions	133
5.2	Future Work.....	137
	Bibliography	140

List of Tables

Table 2-1: Curie temperature and saturation magnetization of Co-Pt alloys [25], [44].	31
Table 2-2: Magnetic energy expressions as a function of the unit magnetization vector $\mathbf{m}(\mathbf{r})$, A (J/m) is the exchange stiffness constant [49].	36
Table 2-3: Magnetic quantities [9], [42], [53], [54].	43
Table 3-1: Microscope and material parameters used for simulation.	65
Table 3-2: Microscope parameters [80].	78
Table 4-1: Summary of specimens used for this work.	80
Table 4-2: Bulk magnetic properties of $\text{Co}_{40}\text{Pt}_{60}$ alloys [1, 3].	103
Table 4-3: Material parameters of $\text{Co}_{40}\text{Pt}_{60}$ alloy [12], [14], [58].	115
Table 4-4: Theoretical and experimental magnetic domain wall widths of $\text{Co}_{40}\text{Pt}_{60}$ alloys.	129

List of Figures

Figure 1.1: Schematic diagram of well-known Materials Science Tetrahedron [1].	1
Figure 1.2: Dark field TEM image showing nano-chessboard structure [11].	4
Figure 2.1: Change in order parameter with the change in reduced temperature, T/T_c in (a) First order phase transformation, (b) Second order phase transformation [20].	12
Figure 2.2: Binary Co-Pt phase diagram [23].	14
Figure 2.3: Phase diagram of Co-Pt alloy bracketing the eutectoid composition, showing crystal structure of disordered and ordered phases [11].	15
Figure 2.4: Crystal structure of the FCC disordered phase with four equivalent sub-lattices, the $L1_0$ phase, and the $L1_2$ phase [30].	17
Figure 2.5: Schematic view of the three orientational variants possible for the $L1_0$ atomic order [30].	17
Figure 2.6: Translational variants in the $L1_0$ structure, Co atoms are shown in black color and Pt atoms are shown in white color.	18
Figure 2.7: Schematic diagram showing formation of an APB [19].	18
Figure 2.8: Phase diagram showing $L1_0$ paramagnetic to ferromagnetic transition.	19
Figure 2.9: Translational variants in $L1_2$ unit cell, filled circles denote Co atoms and open circles denote Pt atoms.	20
Figure 2.10: (a) (110) DF TEM image of the nano-chessboard structure in a near-eutectoid Co-Pt alloy viewed along the [001] zone axis [11]; the bright tiles correspond to the $L1_2$ phase while the dark tiles correspond to the $L1_0$ phase, (b) Schematic, idealized representation of the chessboard structure seen in (a), highlighting the crystallography of the constituent structural domains [13], green arrows represent the c-axis directions of $L1_0$, (c) More accurate depiction of the tile geometry [11].	23
Figure 2.11: Schematic 3-D representation of the nano-chessboard structure where the periodic arrangement of alternate nano-rods of the $L1_0$ and $L1_2$ phases gives the appearance of a chessboard when viewed end-on; different orientations of tetragonal axes shown by straight arrows in $L1_0$ lattice, curved arrows show the rotation direction of $L1_2$ lattice rotated about the rod axis [32].	24
Figure 2.12: Dark Field TEM image (001) showing tweed contrast in a Fe-Pd equiatomic alloy aged for 3 hour at 500°C [33].	26

Figure 2.13: Poly-twinned microstructure in $L1_0$ alloys: (a) Bright Field TEM image showing micro-twins and APBs in Fe-Pd aged for 61 hour at 500°C [33], (b) Two poly-twinned plates containing micro-twins in Fe-Pd alloy [33], (c) Poly-twinned structure in Fe-55%Pd after annealing the sample at 500°C for 36 hour, sample oriented along [130] zone axis [15]. 26

Figure 2.14: Dark Field TEM images of a $Co_{40}Pt_{60}$ alloy aged at 690°C, oriented along [001] axis: left (100) DF, and right (010) DF. The bright and dark domains in the images correspond to X-variants and Y-variants of the $L1_0$ phase, respectively. The dark fringes within the bright domains are anti-phase domain boundaries [11]. 26

Figure 2.15: Dark field images of APBs in $CoPt_3$ ($L1_2$) phase of a $Co_{30}Pt_{70}$ alloy oriented along [001] zone axis: (a) 110 DF, (b) 010 DF, (c) 100 DF [37]. 27

Figure 2.16: Evolution of nano-chessboard structure: (a)-(c) Experimental TEM images of a $Co_{39.5}Pt_{60.5}$ alloy, (d)-(f) Corresponding simulated images [13]. 28

Figure 2.17: Simulated 3-D microstructure development: (a) The tweed structure formed at the initial stage of the phase transformation; green color indicates tetragonal domains with the [100] direction of the c-axis; blue describes the cubic phase and domains of tetragonal phase with other orientations, (b)-(d) Structures formed by decomposition of the tweed structure; their different colors indicate tetragonal phase with different orientations of the tetragonality axes; the black color describes the cubic phase, (e) the filtered ‘low-resolution’ image of green domains of (a), (f)-(h) The composition profile of the structures in (b)-(d) described by different grey levels (black and white are the limiting cases of the equilibrium compositions of the cubic and tetragonal phases) [32]. 29

Figure 2.18: Ordering of magnetic moments leading to paramagnetic-to-ferromagnetic transformation. 31

Figure 2.19: Temperature dependence of the spontaneous magnetization (Order Parameter) of nickel. The Curie point at 628 K is marked [39]. 31

Figure 2.20: Schematic showing the reduction in the demagnetization field as a result of the introduction of magnetic domains into a ferromagnetic sample [42]. 38

Figure 2.21: Crystal structures of Fe, Ni, and Co showing easy and hard magnetization directions with corresponding magnetization (M-H) curves shown below [41]. 40

Figure 2.22: Schematic Bethe Slater curve [40]. 41

Figure 2.23: Magnetic domains separated (a) by an infinitely narrow domain wall, (b) by a domain wall with finite width [42]. 43

Figure 2.24: Schematic figure: (a) a 180° Bloch wall, (b) a Néel wall [39]. 44

Figure 2.25: Schematic model of optimum microstructure suitable for exchange coupling [56]. 46

Figure 2.26: Schematic Hysteresis loops of hard magnetic phase, soft magnetic phase, and exchange coupled composite of the hard and the soft phases [10]. 47

Figure 2.27: Fresnel under-focus image showing macro-domain and micro-domain structures in the aged Fe-Pd alloy [33]. 48

Figure 2.28: The magnetic domain structure of Fe-55%Pd after annealing: (a) & (b) Lorentz under-focus and over-focus Fresnel image of tweed microstructure, (c) Lorentz under-focus Fresnel image of poly-twinned microstructure, (d) Lorentz under-focus Fresnel image of coarsened L1 ₀ grains [15].	50
Figure 3.1: Schematic illustration of (a) Bright field mode, (b) Dark field mode.	55
Figure 3.2: Schematic of a magnetic thin foil and the resulting deflection of an incident electron beam [70].	58
Figure 3.3: Schematic illustration of the Fresnel imaging mode [70].	60
Figure 3.4: Lorentz Fresnel through-focus images of a thin permalloy island [71].	60
Figure 3.5: Schematic illustration of phase computation: a) Infinitely narrow domain wall, b) Finite domain wall width [2].	62
Figure 3.6: Schematic figure showing rotation of magnetization vector from one domain through a 180° Bloch wall, to the other domain in an infinite uniaxial material [49].	64
Figure 3.7: (a) Periodic 2D magnetization configuration with two different domain orientations; magnetization vectors are along [010] and [0-10] directions; domain walls have a width of 50.24 nm, (b) The calculated A-B phase shift for the configuration in (a), (c) Shaded surface representation of the phase shift.	68
Figure 3.8: Schematic illustration of image formation in Lorentz TEM.	70
Figure 3.9: Reconstructed phase map, Induction maps: $B_{x,t}$ and $B_{y,t}$, Color map [71].	75
Figure 3.10: Schematic showing spherical aberration of electron beams [2].	77
Figure 4.1: Conventional TEM images from Specimen S-80 of Co ₄₀ Pt ₆₀ alloy. (a) Bright field TEM image, (b) (110) dark field TEM image showing nano-chessboard structure; solid white arrows in (a) and (b) are pointing to rods corresponding to nano-chessboard colony along the [010] crystallographic axis, (c) [001] zone axis diffraction pattern of region imaged in (a) and (b); the blue circle indicates fundamental reflection, the yellow circle indicates (110) superlattice reflection, the red circle indicates (010) superlattice reflection, and the green circle indicates (100) superlattice reflection, the white 'X' indicates the transmitted beam or (000) which has been blocked by the beam blocker in TEM. The relevant directions are marked in (b).	84
Figure 4.2: (110) Dark field TEM image from Specimen S-80 of Co ₄₀ Pt ₆₀ alloy showing nano-chessboard colonies, red arrows point to coarsened L1 ₀ plates while blue arrows point to APBs, marked circular area is showing a different distribution of L1 ₀ plates; sample is oriented along [001] zone axis.	86
Figure 4.3: (110) Dark field TEM images of Co _{38.5} Pt _{61.5} alloy: (a) Fine L1 ₀ platelets along <110> directions in the L1 ₂ matrix, (b) Thick L1 ₀ platelets in the L1 ₂ matrix [11].	87
Figure 4.4: (110) Dark field TEM image from Specimen S-80 of Co ₄₀ Pt ₆₀ alloy displaying all the possible crystallographic features possible in this alloy including nano-chessboards along all the three crystallographic axes, coarsened L1 ₀ bands/plates, and anti-phase boundaries; sample is oriented along [001] zone axis, diffraction pattern is shown in inset and relevant directions are marked in the figure.	88

- Figure 4.5: (a)-(c) Lorentz Fresnel through-focus series of images of $\text{Co}_{40}\text{Pt}_{60}$ alloy, the dark and white lines as shown by black arrows in (b) and (c) correspond to magnetic domain walls, (d) Reconstructed phase map, (e) Color legend, (f)-(g) Integrated B_{xt} and B_{yt} induction maps, (h) Color map with the arrows showing the magnetic configuration across 180° walls and 90° walls. 90
- Figure 4.6: (a)-(b) Dark field TEM images of $\text{Co}_{40}\text{Pt}_{60}$ alloy from a region of coarsened L1_0 plates, marked rectangular area in (a) is highlighting two coarse L1_0 plates separated by a thin slice of L1_2 phase. 93
- Figure 4.7: (a) Lorentz Fresnel in-focus image, white dashed lines show twin boundaries, (b) Under-focus image, white arrows point to nano-scale fine magnetic features, (c) Color induction map, (d) Magnified color induction map of twinned region, (e) Schematic idealized representation of magnetization orientation of macro-twinned plates. 96
- Figure 4.8: (a) Bright field image showing tweed microstructure, white dashed lines indicate striated features, (b) Dark field image corresponding to (a); inset shows diffraction condition used for imaging, (c) Magnified image of striated features, (d) $[001]$ ZADP, (e)-(f) Bright field-dark field image pairs showing other microstructural features. 97
- Figure 4.9: (a)-(c) Fresnel through focus series of images; black and white straight lines are domain walls, (d) Phase reconstructed color map, showing various magnetic domains, (e) Color legend. 99
- Figure 4.10: (a)-(c) Fresnel through-focus images; black and white straight lines are domain walls, (d) Phase reconstructed color map, showing various magnetic domains, (e) Color legend. 101
- Figure 4.11: (a) In-focus image, (b) Over-focus image, (c) Color induction map of marked rectangular area in (a), (d) Magnified view of marked rectangular area in (c), (e) Phase shift profile of line/region marked in (d). 102
- Figure 4.12: (a) In-focus image, (b) Under-focus image showing zig-zag domain walls, (c) Phase map, arrows point to nano-rods aligned along $[100]$ and $[010]$, (d)-(e) B_{xt} and B_{yt} maps, (f) Color induction map, (g) Color legend, (h) (-110) Dark field TEM image of nano-chessboard [12]. 105
- Figure 4.13: Magnified images of marked rectangular area in Fig. 4.12(f). 107
- Figure 4.14: Idealized figure showing formation of inter phase magnetic domain wall (IPMDW) between L1_0 and L1_2 phases in the nano-chessboard structure. 110
- Figure 4.15: (a) Over-focus image, (b) Phase map, (c)-(d) B_{xt} and B_{yt} maps, (e) Color map, (f) Color legend, (g)-(h) Magnified color map and phase map of rectangular area marked in (e), color map shows anti-vortex pattern and vortex pattern, white dashed lines show position of anti-vortex domain wall, (i) Phase shift profile of region marked by white solid line in (h), pixel size is calibrated as 0.45 nm. 112
- Figure 4.16: Simulated images: (a)-(c) M_x , M_y , M_z extracted from micro-magnetic simulation of nano-chessboard, (d) Simulated phase map, (e)-(f) B_{xt} and B_{yt} maps, (g) Color map, white and black arrows showing vortex and anti-vortex pattern, respectively, (h)-(j) Fresnel through focus images. All images are 256×256 pixel, $256 \text{ pixel} = 400 \text{ nm}$ 117

Figure 4.17: Color induction maps showing beam/sample tilt effect on magnetic contrast of the nano-chessboard structure as the beam is tilted around the x -axis, beam tilt angle marked in each figure.....	119
Figure 4.18: Color induction maps showing beam/sample tilt effect on magnetic contrast of the nano-chessboard structure as the beam is tilted around the y -axis, beam tilt angle marked in each figure.....	119
Figure 4.19: Comparison of Lorentz Fresnel images: (a) Experimental image, green arrow points to repetitive S-shaped domain walls, (b) Simulated image, red box encloses a $L1_0$ - $L1_2$ - $L1_0$ three particle system, green arrows point to two domain walls within this system.....	120
Figure 4.20: Comparison of Phase reconstructed color induction maps: (a) Experimental image, (b) Simulated image. White arrows in both images show vortex-type magnetic configuration.	121
Figure 4.21: Comparison of experimental (above) and simulated images (below): (a) & (d) Over-focus Fresnel images, (b) & (e) Phase maps, (c) & (f) Color induction maps.....	122
Figure 4.22: Experimental Lorentz images of Specimen S-80: (a) & (d) Under-focus Fresnel images, (b) & (e) Phase maps, (c) & (f) Color induction maps.	123
Figure 4.23: (a) Phase map and phase shift profile, (b) Schematic showing calculation of domain wall width from the first order derivative of phase shift profile.....	125
Figure 4.24: Phase shift profile of regions marked by white lines in color induction map of macro-domain walls in Specimen S-40, pixel size is calibrated as 3.70 nm.	126
Figure 4.25: Color induction maps and phase shift profiles: (a) 180° domain wall in macro-twins in Specimen S-40, (b) 180° domain walls in nano-chessboard in Specimen S-40, (c) 180° domain wall in nano-chessboard in Specimen S-80, (d) 90° domain walls in nano-chessboard in Specimen S-80. Pixel size shown in each figure.	128
Figure 4.26: Schematic showing rotation of magnetization across a 180° domain wall and a 90° domain wall.....	131

1 Introduction

1.1 Motivation

Characterization is an important part of materials science and engineering and one that affects all four aspects of the “materials science tetrahedron” (Fig. 1.1). Characterization of materials using techniques such as X-ray Diffractometer (XRD), or Transmission Electron Microscope (TEM) can provide us information about the internal structure all the way down to the arrangement of atoms inside a crystal. Most properties of materials can be directly linked to their crystal structure. For example, in magnetic materials the tetragonal crystal structure is associated with hard magnetic properties because of its high uniaxial magneto-crystalline anisotropy, whereas a magnetic material with a cubic crystal structure is usually a soft magnet. Knowing the microstructure, and the structure-property interrelations, modifications can be made to the microstructure through suitable processing techniques to develop unique materials properties or to improve existing properties.

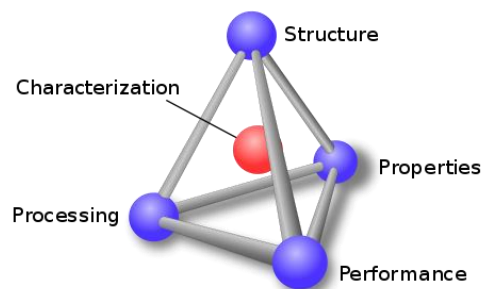


Figure 1.1: Schematic diagram of well-known Materials Science Tetrahedron [1].

In the case of magnetic materials, the Vibrating Sample Magnetometer (VSM) is a useful tool for measuring bulk magnetic properties including Curie temperature, saturation magnetization, and magnetic coercivity. However, this technique can only provide information about the properties averaged over the entire sample. To engineer magnetic materials to suit specific requirements, it is necessary to understand the relationship between the magnetic properties and microstructure of materials, which in turn requires a thorough analysis of the magnetic domain structure. The study of submicron sized magnetic features requires specialized characterization tools and techniques. Lorentz Transmission Electron Microscopy (LTEM) is a powerful tool for studying the magnetic domain structure in conjunction with the crystallographic microstructure [2]. However, one limitation of the conventional Lorentz TEM is the rather low attainable magnification and resolution due to a high spherical aberration, which limits studies of magnetic domain structure to length-scales of several hundred nanometers. Several new age magnetic materials (used in magnetic storage devices) have been found to have magnetic features or defects at length-scales of a few nanometers. To overcome these limitations a spherical aberration corrected Lorentz TEM is required, that can resolve nano-scale magnetic features so that systematic quantitative imaging and analysis can be done. More often, magnetic materials are found to exhibit very complex internal magnetization distributions that are difficult to interpret fully by observing the experimental images. A clear understanding of such domain structures requires a thorough analysis with the help of mathematical modeling and micro-magnetic simulations based on existing magnetic theory and principles. By correlating the experimental characterization data with numerical simulations, quantitative analysis of nano-scale magnetic features is possible.

The $L1_0$ based ordered magnetic alloys including Fe-Pt, Fe-Pd and Co-Pt alloys have long been studied for their applications as hard magnetic materials and in storage devices primarily due to their high coercivity (H_c) and high energy product (BH_{max}) [3]–[5]. It is also well documented that the magnetic properties of these alloys are strongly dependent on composition and thermal history due to the influence of each on the atomic ordering and the anisotropy of the tetragonal $L1_0$ phase [6], [7]. Nano-composite magnetic materials are also increasingly studied in the development of present generation magnetic devices [8]–[10]. These magnetic alloys usually go through a suitable thermal processing resulting in optimum microstructures that provide large magnetic anisotropy and higher coercivity. One such microstructure is the novel nano-chessboard structure (Fig. 1.2), first discovered by Leroux et al. in 1991 [11]. Co-Pt alloys with compositions in the narrow eutectoid range ($\sim\text{Co}_{40}\text{Pt}_{60}$) can undergo a eutectoid transformation via pseudo-spinodal decomposition to produce a unique self-assembled nano-chessboard structure. This microstructure consists of a hard magnetic $L1_0$ phase (CoPt) and a soft magnetic $L1_2$ phase (CoPt_3) interleaved at the nano-scale. The resulting periodic nano-composite is expected to exhibit exchange coupling between its hard and soft ferromagnetic constituents, making it a potential candidate for high-density magnetic storage devices and permanent magnets. When viewed end-on in dark field TEM mode, the structure appears as a nano-chessboard with alternate dark and bright tiles with length-scales of 10-20 nm. The dark tiles correspond to the tetragonal $L1_0$ phase while the bright tiles are the cubic $L1_2$ phase. Detailed TEM microstructural studies and bulk magnetic properties studies (VSM) of these microstructures have been performed by [12], [13]. Recent work has focused on micro-magnetic simulations to understand the length-scale effect of $L1_0$ - $L1_2$ chessboard on the exchange coupling behavior [14]. However, none of these studies have reported any sort of magnetic

domain structure analysis in these alloys, which is pivotal to understanding the underlying magnetic properties.

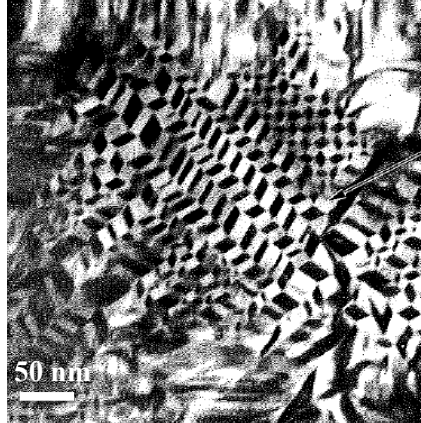


Figure 1.2: Dark field TEM image showing nano-chessboard structure [11].

Co-Pt alloys go through a range of transformations, as they are heat-treated to obtain the nano-chessboard structure. Firstly, the eutectoid decomposition transforms a high symmetry FCC (Face centered cubic) disordered phase into two low symmetry ordered phases: $L1_0$ (tetragonal phase) and $L1_2$ (cubic phase). This ordering transformation gives rise to various crystallographic boundaries including anti-phase boundaries (APB), $L1_0$ structural boundaries and twin boundaries. In addition, the alloy goes through a paramagnetic to ferromagnetic transformation as it is cooled below the Curie temperature. The ordering of magnetic moments results in the formation of magnetic domains and domain walls. Magnetic domains are coupled to the crystallographic domains through magneto-crystalline anisotropy energy. Thus, the interplay between crystal domains and magnetic domains dictates the magnetic domain structure and hence the magnetic properties. The primary cause for an increased coercivity in $L1_0$ -type alloys is believed to be magnetic domain wall pinning during the magnetization process [15]. The

different crystallographic defects mentioned above can act as pinning centers for the motion of domain walls under the influence of an applied field. However, the degree or extent of pinning varies across various defects. For example, an APB is a weak pinning center whereas a twin boundary is a relatively strong pinning center [16], [17]. It will be interesting to investigate the pinning effect of $L1_0$ - $L1_2$ phase boundaries in the nano-chessboard structure. From these studies, it is clear that the interaction between magnetic and microstructural features plays a major role in influencing the magnetic properties of these alloys. The present work is an effort to understand the nature of such interactions. A direct characterization of these types of interactions has not been done before at such fine length scales. The primary motivation and objective of this work is to address the lack of understanding in the following areas:

1. Analysis of magnetic domain structure in $Co_{40}Pt_{60}$ alloys.
2. Study of interaction between magnetic and crystallographic features in $Co_{40}Pt_{60}$ alloys.
3. Quantification and characterization of different types of magnetic domain walls.
4. Correlating magnetic domain structure with the observed bulk magnetic properties.

In summary, this work focuses on the quantitative characterization of magnetic domains and domain walls in near-eutectoid $Co_{40}Pt_{60}$ alloys.

1.2 Hypothesis

The objective of this thesis is to characterize the magnetic domain structure in near eutectoid $Co_{40}Pt_{60}$ alloys. The main hypotheses of this work are as follows:

1. The structure and width of magnetic domain walls in the nano-chessboard structure is dependent on the magnetic interaction between the $L1_0$ and $L1_2$ phases and the

length-scales of individual phases.

2. Aberration corrected Lorentz microscopy can be used to obtain more reliable magnetic inductions maps and quantitative results such as magnetic domain wall width.
3. The magnetic contrast in the experimental Lorentz images at unknown sample orientations can be interpreted with the help of Lorentz images simulated at different electron beam tilts.

To validate these hypotheses, we will be focusing on studying following areas. Firstly, magnetic domain structure of different crystallographic microstructures in Co-Pt alloys will be characterized; the morphology of magnetic domains and the size/shape of magnetic domain walls will be analyzed for each microstructure to establish a relation between the observed magnetic domain structure and the crystallographic microstructure. Secondly, the structure/width of magnetic domain walls in the nano-chessboard structure will be compared to the wall widths obtained in other microstructures; this will allow us to predict the effect of length-scale of $L1_0$ and $L1_2$ phases on the magnetic domain structure, this observation will also enlighten us regarding magnetic behavior of different crystallographic phases as their size decrease below a critical value. Nano-chessboard structure will be examined by both the uncorrected Lorentz microscopy as well as aberration corrected Lorentz Microscopy and the results will be compared. The Lorentz images will be simulated for various relative beam-sample tilt orientations and compared with the experimental Lorentz images across different regions in multiple samples. This will allow us to correlate the magnetic contrast of the experimental Lorentz images with the sample orientation.

1.3 Experimental Design

1.3.1 Experimental techniques

Transmission Electron Microscopy (TEM) is used as the principal technique to carry out the experimental observations reported in this document. The following experiments are used to investigate domains in the alloys under consideration:

1. Lorentz mode TEM: Fresnel mode (defocussed mode) imaging of magnetic domain walls in $\text{Co}_{40}\text{Pt}_{60}$ alloys in the demagnetized state.

Instrument used: FEI Tecnai F20, operated at 200 kV and equipped with dedicated Lorentz pole piece.

2. Spherical aberration corrected Lorentz TEM: Fresnel mode (defocussed mode) imaging of magnetic domain walls of nano-chessboard structure in $\text{Co}_{40}\text{Pt}_{60}$ alloys in the demagnetized state.

Instrument used: FEI Titan 80-300, operated at 300 kV and equipped with dedicated Lorentz pole piece.

3. Phase reconstruction: Phase reconstruction of Lorentz Fresnel images using IDL code.
4. Conventional mode TEM: Bright field/Dark field imaging of crystallographic microstructures in $\text{Co}_{40}\text{Pt}_{60}$ alloys.

Instrument used: FEI Tecnai F20, operated at 200 kV and FEI Titan 80-300, operated at 300 kV.

1.3.2 Simulation technique

1. MATLAB: Simulation of magnetic phase shift, magnetic induction maps, and Lorentz Fresnel TEM images of nano-chessboard structure in $\text{Co}_{40}\text{Pt}_{60}$ alloys.

1.3.3 Material

The experimental observations are carried out on the following material system:

1. Co-Pt alloys: Polycrystalline samples of near-eutectoid $\text{Co}_{40}\text{Pt}_{60}$ alloys are analyzed in this study. The samples were synthesized at the University of Virginia by Priya Ghatwai [12] and Eric Vetter [14]. Two alloys subjected to different annealing conditions are chosen for comparative experimental study. They are different in the sense that the second sample (S-80) produces a relatively finer nano-chessboard structure as compared to the first sample (S-40). The details about the sample fabrication and processing are provided in Section 4.2.

The Fresnel mode of imaging is employed to study magnetic domain walls in $\text{Co}_{40}\text{Pt}_{60}$ alloys. The magnetic domain walls appear as bright and dark features in the defocussed images, as described in more detail in Chapter 3 and Chapter 4. The phase shift of the electron waves are reconstructed from Fresnel through-focus series using transport-of-intensity equation. The phase maps are converted to magnetic induction maps, which give the direction of integrated in-plane magnetization directions inside the sample. Domain wall width is also measured from the phase shift profile for a particular domain wall. The experimentally obtained magnetic induction data is quantitatively interpreted by computing electron phase shift on simulated nano-chessboard structures. The experimental phase maps in conjunction with simulated phase maps provide a better understanding of magnetic configurations in the nano-chessboard structure. Bright field/Dark field imaging in the conventional TEM mode (with objective lens switched on) is utilized to characterize the crystallographic microstructure for subsequent comparison with the Lorentz TEM images. In summary, magnetic domain structure of near-eutectoid Co-Pt alloys

are characterized by utilizing Lorentz Fresnel mode imaging, conventional Bright field/Dark field imaging, phase reconstruction, and image simulations based on micro-magnetic models.

1.4 Document Organization

This document is divided into five different chapters. In Chapter 2, we introduce the background literature relevant to the Co-Pt alloy system. Chapter 3 summarizes experimental and simulation techniques applied to this work. In Chapter 4, we present experimental and simulation results along with analysis and discussions. Finally, the conclusions from our observations and potential avenues for future work in this area are outlined in Chapter 5.

2 Phase Transformations and Domain Structures in Co-Pt Alloys

2.1 Introduction

Solid-state phase transformations such as atomic ordering and ferromagnetic transformations, result in domains/variants due to a reduction in symmetry. The atomic ordering transformation results in anti-phase domains and anti-phase boundaries while the ferromagnetic transformation results in magnetic domains and magnetic domain walls. An understanding of the different phase transformations and their characteristics is required in order to fully understand the interactions between multiple domain structures.

In this chapter, the characteristic features of the multiple phase transformations in Co-Pt alloys are reviewed. The first half of this chapter focuses on the atomic ordering transformation. The phase diagram of a binary Co-Pt alloy is introduced followed by the description of crystallographic properties of the disordered and the ordered phases as well as the resultant domains. Thereafter eutectoid transformations and the formation of nano-chessboard structures are explained. The second half of this chapter focuses on the magnetic ordering transformation. The origin of magnetic moments is discussed followed by the micro-magnetic theory and a description of magnetic domains. Several magnetic concepts and quantities are discussed in

detail. Then the exchange coupling in nano-composite materials is discussed. In the end, studies done previously on the magnetic domain structure of alloy systems similar to Co-Pt alloys are discussed.

2.2 Atomic Ordering Transformation

Disorder-order transformations are characterized by an ordered arrangement of atoms at low temperatures, which becomes progressively disordered as the temperature is raised, until the long-range order disappears at a critical temperature. Atomic or chemical ordering refers to the arrangement of atoms on distinct sub-lattices of an intermetallic alloy. In the disordered state, the different atoms of the intermetallic randomly occupy these sub-lattices. The degree of ordering can be described by the order parameter, $\eta = (R-W) / (R+W)$, where R is the number of atoms occupying the correct atomic sites and W is the number of atoms occupying the incorrect atomic sites in the ordered structure [18]. In stoichiometric alloys, the maximum order parameter is 1 whereas in non-stoichiometric alloys this is $2g$, g being the atomic fraction of solute atoms in the alloy. The proportion of atoms occupying wrong sites increases with increasing temperature [19], [20].

The ordering transformations can be further characterized as first order or second order phase transformation depending on the ordering mechanism. In the case of first order transformations, the ordered domains form by the nucleation and growth upon overcoming the thermodynamic energy barrier for the formation of these domains [19]. This type of ordering occurs in FCC \rightarrow L1₀ or FCC \rightarrow L1₂ transformation where the order parameter η drops slightly upon heating up to the critical temperature T_c and then precipitously to 0 at T_c , as shown in Fig. 2.1(a). A steep

change in order occurs at the critical temperature. Second order phase transformations occur by a continuous change in the short-range order via local atomic rearrangement within the crystal, without an associated energy barrier, eventually resulting in long-range order [19]. Thus, no nucleation event is required. This type of ordering is observed in the A2 \rightarrow B2 ordering transformation, where the long-range order parameter η changes continuously from 0 at the critical temperature T_c , to 1 at 0 K, as shown in Fig. 2.1 (b).

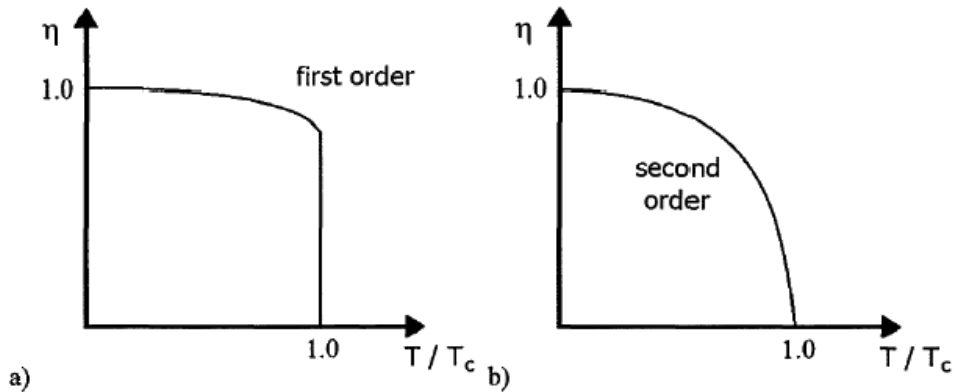


Figure 2.1: Change in order parameter with the change in reduced temperature, T/T_c in (a) First order phase transformation, (b) Second order phase transformation [20].

Several binary alloys exhibit ordered structures based on the parent lattice. When the disorder-order transition takes place, the high symmetry parent lattice is transformed to the low symmetry products giving rise to domains/variants. The number of domains/variants depends on the type of reduction in symmetry and will be explained further in Section 2.2.2. The two most common ordered structures based on the FCC lattice are the $L1_0$ and $L1_2$ structures. Alloys with these ordered structures are studied because of their unique properties. For example, $L1_0$ binary alloys such as Co-Pt [4], Fe-Pt [5], Fe-Pd [21] are studied because of their applications as magnetic materials for high-density magnetic storage and permanent magnets. Alloys with low-symmetry

crystal structures, such as the $L1_0$ tetragonal structure, possess a large uniaxial magnetocrystalline anisotropy, K_u that can be exploited to yield high coercivity, H_c and high magnetic energy product, BH_{max} in appropriate microstructures. The anisotropy is believed to come from the atomic ordering as well as the tetragonality, c/a ratio [22]. The $L1_2$ counterparts ($CoPt_3$, $FePt_3$, $FePd_3$) of these alloys are known for their soft magnetic behavior. Only few binary alloys show coherent phase diagrams with both the $L1_0$ and $L1_2$ phases, including Co-Pt, Fe-Pt and Fe-Pd alloys.

2.2.1 Phase diagram of binary Co-Pt alloy

The equilibrium phase diagram for the binary Co-Pt system is shown in Fig. 2.2 [23]. At temperatures above 1400 K, an A1 (FCC) solid solution forms across the entire composition range. Co-Pt alloys of appropriate composition can undergo a disorder-order transformation upon cooling, or conversely, an order-disorder transformation upon heating, and the phase diagram indicates the regions over which the ordered phases persist. The $L1_0$ ordered phase forms upon cooling the equiatomic CoPt disordered A1 phase, with a maximum ordering temperature of 1100 K [6]. The $L1_0$ phase has excellent intrinsic magnetic properties, including a high uniaxial magnetocrystalline anisotropy approaching that of rare earth magnets, K_u of 4.9×10^7 ergs/cc, saturation magnetization, M_s of 800 emu/cc, and Curie temperature, T_c of 840 K [24], [25]. The equiatomic Co-Pt is found to possess the largest K_u . Hence, most investigations of ordering and magnetism in the Co-Pt binary system have generally been based on the 1:1 composition. A 1:3 atomic ratio of Co and Pt results in a disorder to order transformation from the disordered A1 (FCC) phase to the ordered, magnetically soft $L1_2$ phase, $CoPt_3$. $L1_2$ has a maximum atomic ordering temperature of 1000 K [6]. Both the $L1_0$ and $L1_2$ phases are paramagnetic at high

temperatures and become ferromagnetically ordered at lower temperatures.

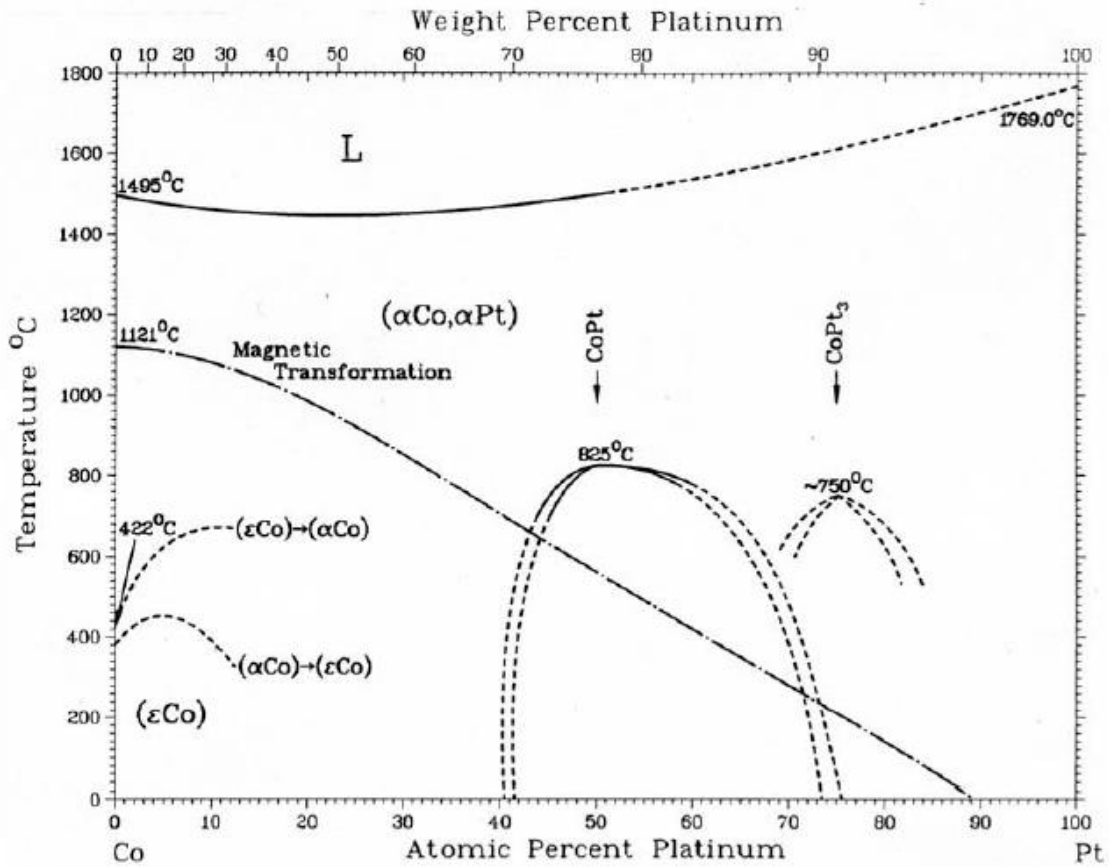


Figure 2.2: Binary Co-Pt phase diagram [23].

Fig. 2.3 shows the Co-Pt phase diagram in compositions bracketing the eutectoid composition. The coherent phase diagram was first determined by Leroux et al. [11] on the basis of TEM microstructural studies in the vicinity of the eutectoid composition. Eutectoid decomposition refers to the transformation of a solid phase into two other solid phases upon cooling [26]. In the case of Co-Pt alloy, the α solid phase (A1, FCC) transforms to two solid phases with composition CoPt_3 and CoPt . The crystal structures corresponding to the A1, L1₀, and L1₂ phases are schematically depicted in the figure. The eutectoid temperature is around 725°C.

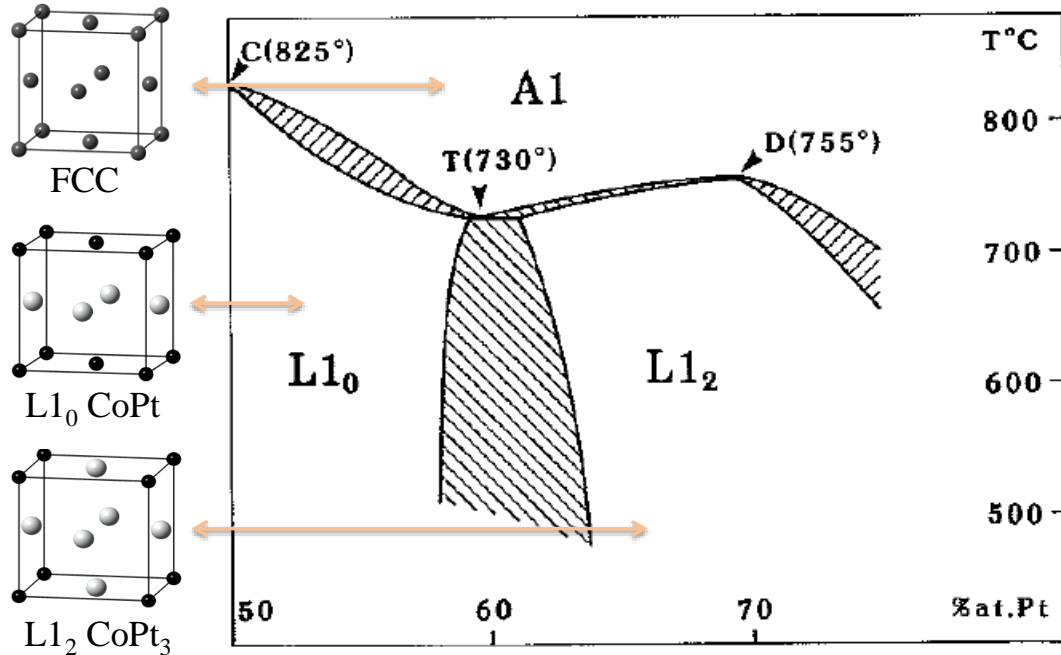


Figure 2.3: Phase diagram of Co-Pt alloy bracketing the eutectoid composition, showing crystal structure of disordered and ordered phases [11].

2.2.2 Crystal structure of L1₀ and L1₂ ordered phases

In the disordered A1 phase (FCC) of the binary Co-Pt alloy, Co and Pt atoms randomly occupy all the FCC lattice sites, namely (0,0,0), (1/2,1/2,0), (1/2,0,1/2), and (0,1/2,1/2). The lattice parameter is $a = 0.3751$ nm [27] and the space group is Fm-3m. The ordered L1₀ and L1₂ structures can be crystallographically derived from the FCC structure as explained below.

The FCC lattice can be divided into four simple cubic sub-lattices namely α_1 , α_2 , α_3 , α_4 as shown in Fig. 2.4. In the ordered, stoichiometric L1₀ phase, Co atoms occupy α_1 and α_2 sub-lattices ($\alpha_1 = \alpha_2$) while Pt atoms occupy α_3 and α_4 sub-lattices ($\alpha_3 = \alpha_4$). In other words Co atoms and Pt atoms occupy alternate (001) planes. The L1₀ phase corresponds to a Face Centered Tetragonal (FCT) unit cell, with lattice parameters $a = 0.3803$ nm and $c = 0.3701$ nm and space group

P4/mmm [27]. The structure has a slight tetragonal distortion in the [001] direction, with a tetragonality ratio of $c/a = 0.97$.

The transformation of FCC to $L1_0$ changes the symmetry of the crystal since the space group changes from Fm-3m to P4/mmm. Initially equivalent sites become non-equivalent. Because of tetragonalization, the concentration modulation direction (c-axis) is no longer equivalent to the other two $\langle 100 \rangle$ -type axes. This decrease in symmetry gives rise to domains/variants. Two types of crystallographic domains are observed depending on the change in the point group, the Bravais lattice or both. In $FCC \rightarrow L1_0$, the change in point group results in the orientational/structural domains in this alloy. There is a decrease in the number of point group symmetry elements from 48 for FCC to 16 for $L1_0$. The symmetry is lowered by a factor of 3, hence three orientational/structural variants are obtained as shown in Fig. 2.5. The orientational variants are separated by $\{101\}$ -type planes. They are called the X, Y and Z variants depending on whether the half plane is (100), (010), or (001) [28]–[30]. The lattice parameter of the unit cell is ‘c’ along the tetragonal axis, i.e., along the normal to the ordering half plane, and ‘a’ along the remaining two cube axes.

Furthermore, the Bravais lattice changes in $FCC \rightarrow L1_0$; the number of equivalent site decreases from 4 for FCC to 2 for $L1_0$. This gives rise to two translational domains. For example, in Fig. 2.6 (a), Co atoms are located at (0,0,0) and (1/2,1/2,0) sites while Pt atoms are located at (1/2,0,1/2) and (0,1/2,1/2) sites. On the other hand, in the variant shown in Fig. 2.6 (b), Pt atoms are located at (0,0,0) and (1/2,1/2,0) sites while Co atoms are located at the (1/2,0,1/2) and (0,1/2,1/2) sites. Each orientational variant has two translational variants making a total of six

possible crystallographic variants in this $L1_0$ structure. It should be noted that the lost symmetry operation transforms one domain to another domain [28]. The differently oriented ordered/translational domains are called anti-phase domains. The boundary between different translational domains is called an anti-phase boundary (APB). The atoms have wrong kind of neighbors across an APB, therefore APBs are high-energy regions of the lattice and are associated with an APB energy. APBs resulting from atomic/chemical ordering are called thermal APBs. Fig 2.7 shows the formation of an APB as two differently ordered domains nucleate and grow [19].

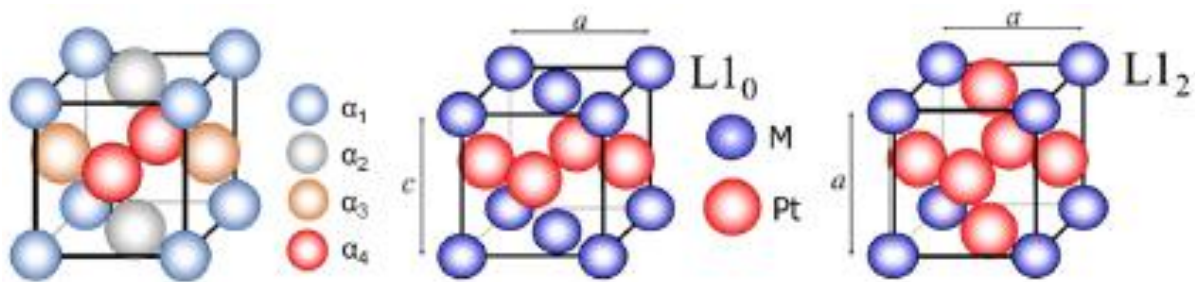


Figure 2.4: Crystal structure of the FCC disordered phase with four equivalent sub-lattices, the $L1_0$ phase, and the $L1_2$ phase [30].

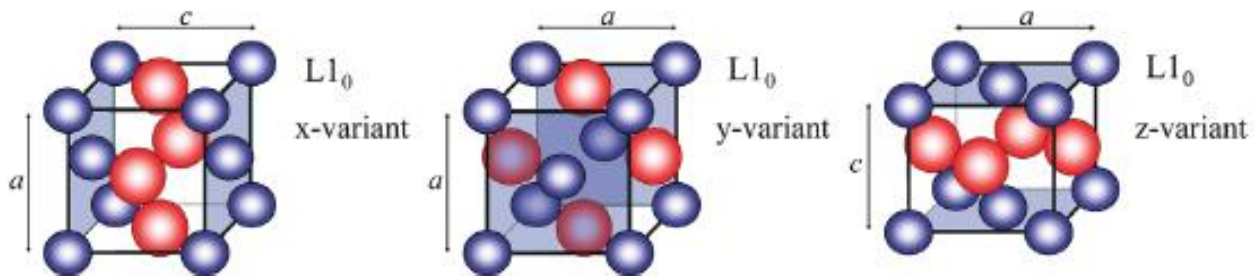


Figure 2.5: Schematic view of the three orientational variants possible for the $L1_0$ atomic order [30].

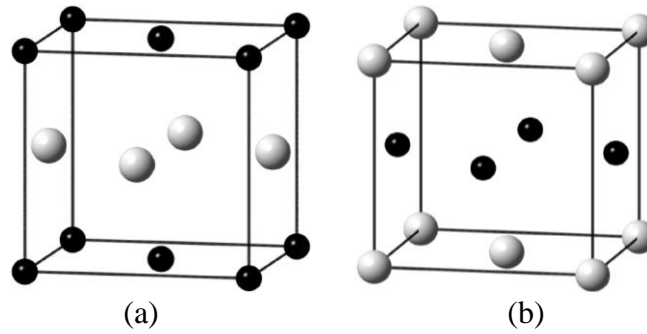


Figure 2.6: Translational variants in the $L1_0$ structure, Co atoms are shown in black color and Pt atoms are shown in white color.

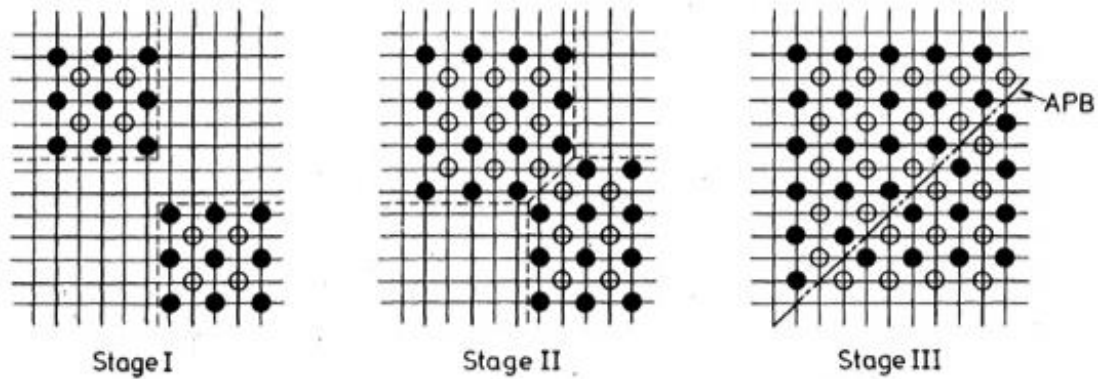


Figure 2.7: Schematic diagram showing formation of an APB [19].

In addition, if the $L1_0$ phase goes through the paramagnetic to ferromagnetic transition, as shown in Fig. 2.8, the decrease in magnetic symmetry would give rise to magnetic domains. In tetragonal crystals, the easy axis of the magnetization/magnetic moment lies along the tetragonal/c-axis, $M//[001]$. Hence, each of the above six crystallographic domains could have two directions of the magnetic moment: $[001]$ and $[00-1]$. This gives rise to a total of 12 domains in an atomically and magnetically ordered $L1_0$ phase. However, there are only 6 distinguishable magnetic domains. Each of the magnetic domains has an anti-phase partner. Also note that in this case, the structural domains coincide with the magnetic domains because the c-axes correspond to the magnetic axes [28].

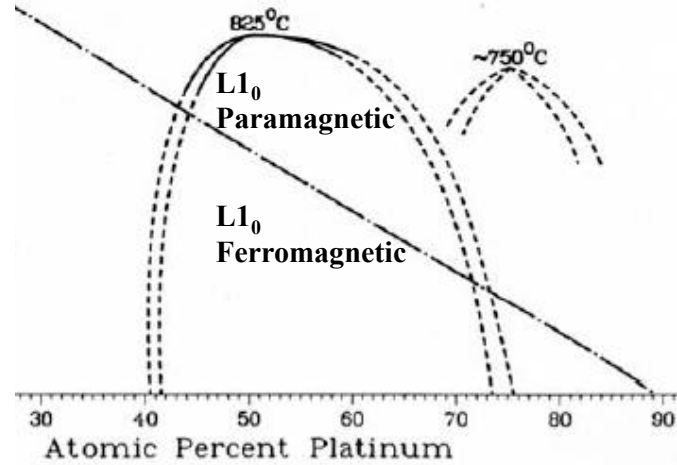


Figure 2.8: Phase diagram showing L1₀ paramagnetic to ferromagnetic transition.

In the ordered, stoichiometric L1₂ phase, CoPt₃, Co atoms occupy the α_1 sub-lattice while Pt atoms occupy the α_2 , α_3 and α_4 sub-lattices ($\alpha_2 = \alpha_3 = \alpha_4$), Fig. 2.4. The space group of the L1₂ phase is Pm-3m and lattice parameter $a = 0.3854$ nm [27]. The transformation of FCC to L1₂ changes the symmetry of the crystal from Fm-3m to Pm-3m. Since the point group remains unchanged, there is no tetragonality and all three $\langle 100 \rangle$ -type directions remain equivalent. However, the Bravais lattice changes from face-centered to primitive cubic lattice which results in four translational domains depending on the position of the four atoms at different sub-lattices (Fig. 2.9). These domains are separated by APBs, characterized by the displacement vector $R = [1/2, 0, 1/2]$, or $R = [0, 1/2, 1/2]$, or $R = [1/2, 1/2, 0]$. R can be determined using TEM in two-beam conditions in the dark field imaging mode, using super-lattice reflections that arise due to the L1₂ ordering [11].

In the case of the L1₂ phase, the magnetization lies along the $\langle 100 \rangle$ axis, $M // \langle 100 \rangle$, and six distinguishable magnetic domains can be expected from the para-to-ferro transition. Each of the magnetic domains has four translational domains, hence 24 domains emerge in an atomically and

magnetically ordered $L1_2$ phase. It has been reported that in equiatomic Co-Pt alloys, the coercivity is highest at an intermediate state of order with coherent ordered and disordered phases and decays as the lattice becomes completely ordered [31].

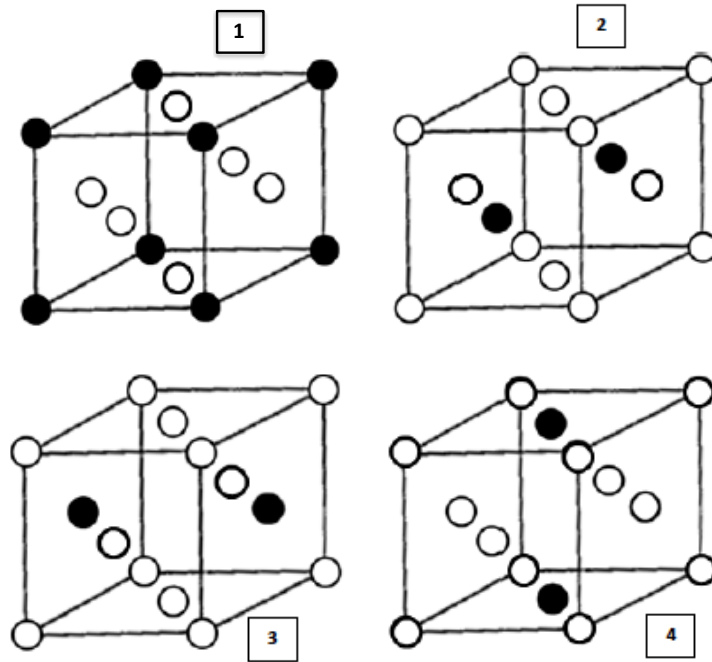


Figure 2.9: Translational variants in $L1_2$ unit cell, filled circles denote Co atoms and open circles denote Pt atoms.

2.2.3 Eutectoid phase transformation in Co-Pt alloys

As described in Section 2.2.1, Co-Pt alloys with appropriate composition and thermal treatments can result in ordered phases $L1_0$ or $L1_2$ based on the stoichiometry of the alloy, by the disorder-order mechanism. The region of the phase diagram where two ordered phases co-exist has not been fully investigated. Compositions near the eutectoid region (~60% Pt) can undergo eutectoid decomposition, $A1 \rightarrow L1_0 + L1_2$ upon cooling through the eutectoid temperature, to produce a mixture of the $L1_0$ and $L1_2$ ordered phases. This region was first explored by Leroux et al. in

which they reported the formation of an interesting microstructure obtained by appropriate heat treatment of Co-Pt alloys in the near-eutectoid region [11]. This microstructure was reported to look like a “nano-chessboard” structure that consisted of both the ordered phases $L1_0$ and $L1_2$ simultaneously as shown in the (110) Dark Field (DF) TEM image in Fig. 2.10 (a). In this DF image, the black tiles correspond to the $L1_0$ phase and the bright tiles correspond to the $L1_2$ phase. They demonstrated the composition and temperature range for the co-existence of the two-phase mixture with the help of TEM studies. Although the Co-Pt phase diagram was known in various regions, the region around the triple point ($A1$, $L1_0$, $L1_2$) was not accurately known until Leroux et al. studied the phase diagram in the 58%-63% Pt region and determined the accurate points utilizing TEM studies. The phase diagram bracketing eutectoid region was approximately determined as shown in Fig. 2.3. The Co-Pt samples were first annealed at an elevated temperature, 930°C , and then water quenched to retain the disordered FCC phase. This was followed by continuous cooling from 740°C at the rate of $20^\circ\text{C}/\text{day}$ up to the temperature of interest followed by annealing at this temperature, ranging from ‘few days’ at 700°C to three weeks at 530°C . A eutectoid reaction was located at $730^\circ\text{C} \pm 5^\circ\text{C}$ and $59.5\% \pm 0.5\%$ Pt. According to this phase diagram, the eutectoid reaction isotherm spans a very narrow composition range, 59.5% to 61.5% Pt ($\pm 0.5\%$ Pt) and the two-phase region extends from 58% to 63% Pt at low temperature.

A schematic diagram of an ideal nano-chessboard structure is shown in Fig. 2.10 (b). The nano-chessboard structure is composed of well-aligned alternating rods of single crystal $L1_2$ and $L1_0$ phases. The $L1_2$ and $L1_0$ rods share a common parent lattice and a coherent interface and typically exist in packed structures aligned along one of the three cube axes of the parent phase.

So, three spatial orientations of the chessboard are possible within a given grain of the parent phase, A1. The checkered pattern is observed when the structure is viewed end-on with respect to the axis of rod alignment, in the DF mode of a TEM, seen in Fig. 2.10(a). There are two orientational variants of the L1₀ phase present, both are visible as dark tiles, while the L1₂ phase is visible as the bright contrast in the DF image. The two variants of the L1₀ phase have mutually perpendicular c-axes that are also perpendicular to the rod axis along which the nano-rods are aligned. The side-on view of the chessboard would reveal nano-rods instead of tiles as schematically shown in Fig. 2.11.

The orientation relationship between the L1₀ and L1₂ tiles is (110) L1₀ || (110) L1₂ and [100] L1₀ || [100] L1₂. The L1₀/L1₂ interfaces are close to the {110} planes, having a deviation of ± 11°. The ‘tiles’ form zigzag bands along <110> with alternate bands containing tiles of L1₂ + X variant of L1₀ and L1₂ + Y variant of L1₀ respectively. It should be noted that only L1₀ and L1₂ phases share interfaces; L1₀ orientation variants do not share common interfaces [11].

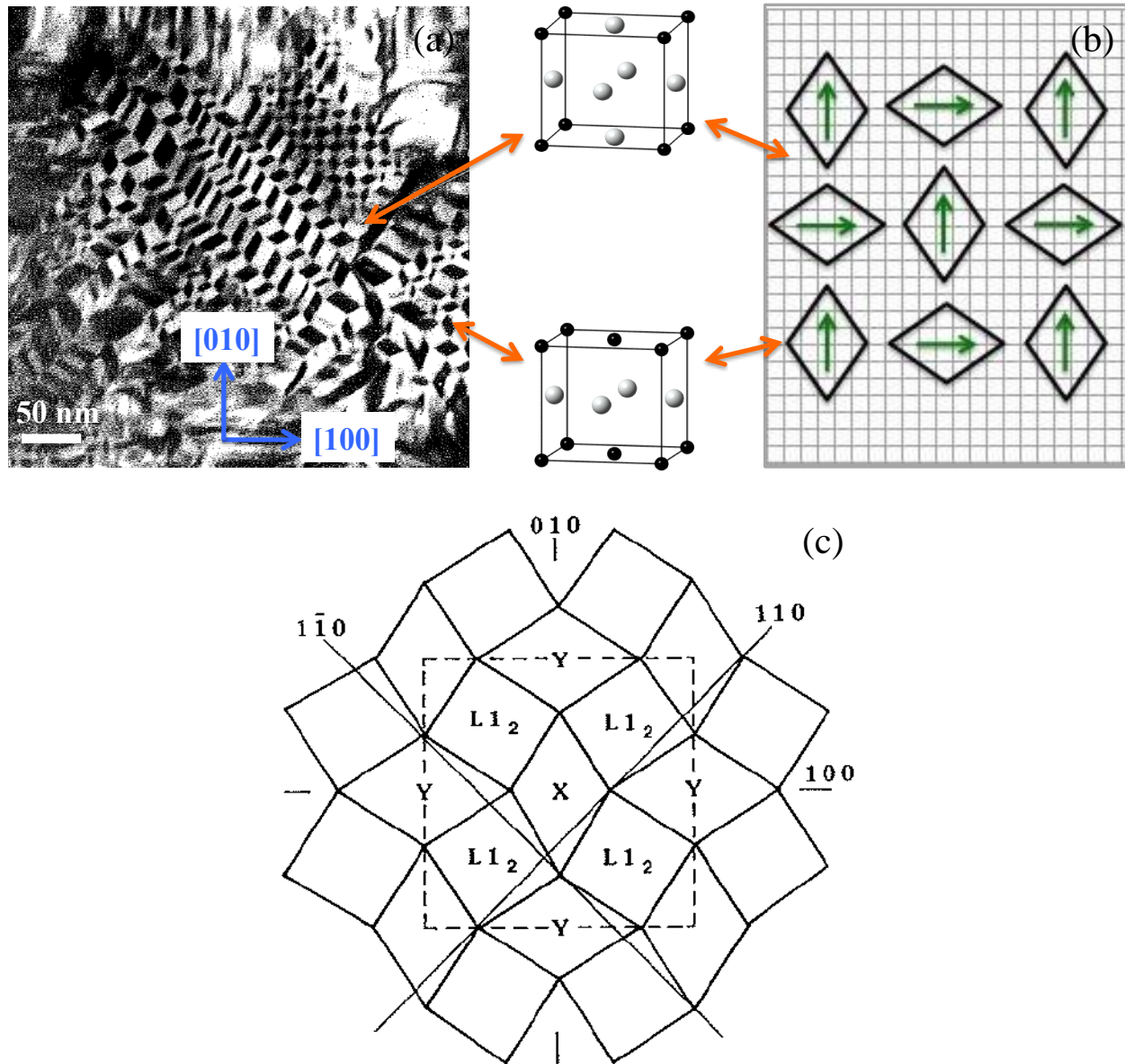


Figure 2.10: (a) (110) DF TEM image of the nano-chessboard structure in a near-eutectoid Co-Pt alloy viewed along the [001] zone axis [11]; the bright tiles correspond to the $L1_2$ phase while the dark tiles correspond to the $L1_0$ phase, (b) Schematic, idealized representation of the chessboard structure seen in (a), highlighting the crystallography of the constituent structural domains [13], green arrows represent the c-axis directions of $L1_0$, (c) More accurate depiction of the tile geometry [11].

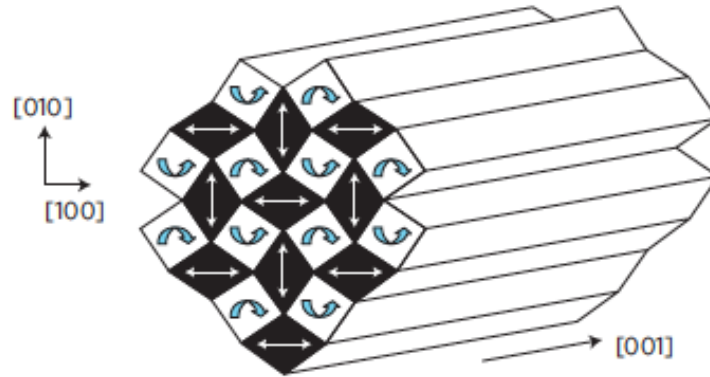


Figure 2.11: Schematic 3-D representation of the nano-chessboard structure where the periodic arrangement of alternate nano-rods of the $L1_0$ and $L1_2$ phases gives the appearance of a chessboard when viewed end-on; different orientations of tetragonal axes shown by straight arrows in $L1_0$ lattice, curved arrows show the rotation direction of $L1_2$ lattice rotated about the rod axis [32].

2.2.4 Evolution of microstructure

The ordering transformation is accompanied by the formation of several interface/inter-phase boundaries due to the existence of multiple variants of the ordered phase. Depending on the thermal treatments and the composition of the Co-Pt alloys, the ordering can be of three types:

1. FCC A1 \rightarrow $L1_0$
2. FCC A1 \rightarrow $L1_2$
3. FCC A1 \rightarrow $L1_0 + L1_2$

The resulting microstructure due to the different ordering mechanisms is described next.

FCC A1 \rightarrow $L1_0$: The microstructural evolution of $L1_0$ ordering has been studied in many binary alloys including Co-Pt [11], Fe-Pd [15], [33]–[35], Fe-Pt [33], [36] alloys. Two types of microstructure have been observed in such alloys: tweed microstructure and poly-twinned structure. The transformation starts with the formation and alignment of the $L1_0$ nuclei on the $\{110\}$ planes, along $\langle 1-10 \rangle$ directions in the disordered matrix [33]. During aging the ordered

and disordered regions remain fully coherent until the disordered phase is finally consumed. Any of the three orientational variants of the $L1_0$ phase can form within a single grain of the parent phase. The ordered particles/variants arrange themselves along different directions in order to accommodate the lattice mismatch strain produced during ordering; this in turn results in a “tweed contrast” or “tweed microstructure” containing plates of $L1_0$ variants, as shown in Fig. 2.12.

Initially, particles of all the three $L1_0$ orientation variants are formed. But, as the transformation proceeds, generally two variants persist through preferential growth and coarsening. This process produces alternating bands along the $\{110\}$ planes comprised of orthogonal variants (microtwins) that are twin related. With further aging, the growing particles impinge and coalesce to form the poly-twinned structure as shown in Fig 2.13. This impingement and coalescence of particles result in a very high density of APBs within the twin plates as shown in Fig. 2.13(a). The density of APBs is believed to play a central role in the mechanism of coercivity controlling magnetization reversal. The tetragonality of the plates causes a mutual rotation of the c-axes, to produce coherent twin boundaries. After long time annealing, coarsened $L1_0$ grains are formed [15], [33].

Fig. 2.14 shows DF TEM images of poly-twinned microstructures in a $Co_{40}Pt_{60}$ alloy. The microstructure consists of X-variants and Y-variants. In the (100) DF image, the bright plates correspond to the X-variant while the dark plates are the Y-variants. The (010) DF image can be seen reversing the contrast of the X-variants and Y-variants.

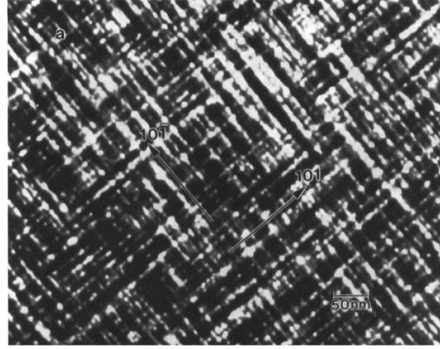


Figure 2.12: Dark Field TEM image (001) showing tweed contrast in a Fe-Pd equiatomic alloy aged for 3 hours at 500°C [33].

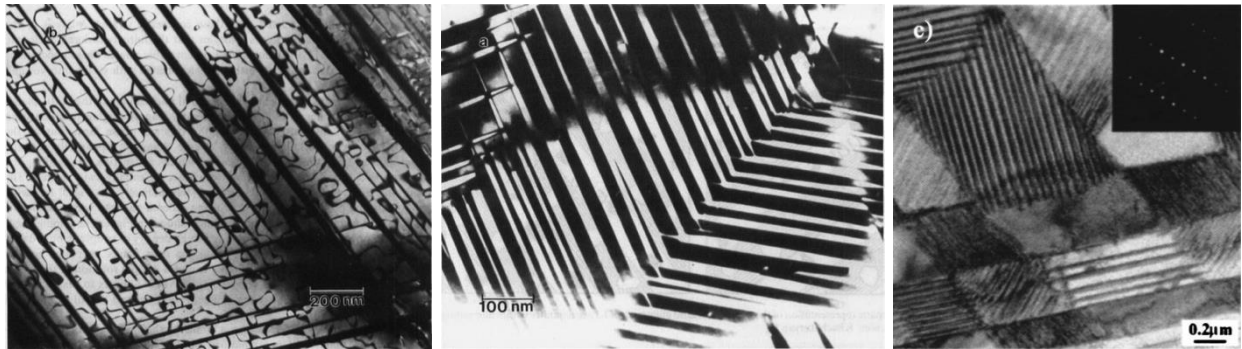


Figure 2.13: Poly-twinned microstructure in $L1_0$ alloys: (a) Bright Field TEM image showing micro-twins and APBs in Fe-Pd aged for 61 hours at 500°C [33], (b) Two poly-twinned plates containing micro-twins in Fe-Pd alloy [33], (c) Poly-twinned structure in Fe-55%Pd after annealing the sample at 500°C for 36 hours, sample oriented along [130] zone axis [15].

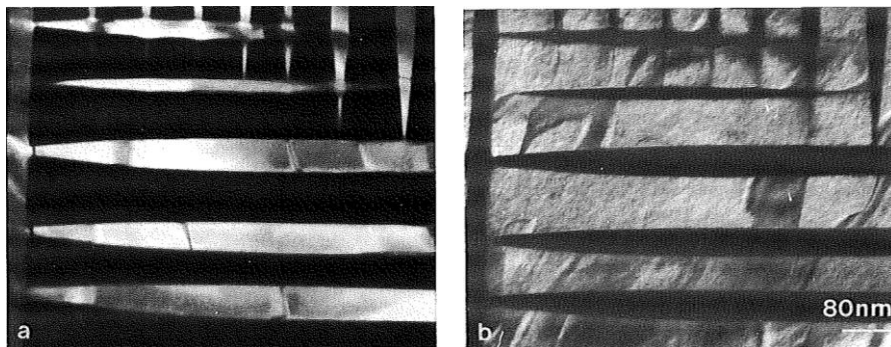


Figure 2.14: Dark Field TEM images of a $Co_{40}Pt_{60}$ alloy aged at 690°C, oriented along [001] axis: left (100) DF, and right (010) DF. The bright and dark domains in the images correspond to X-variants and Y-variants of the $L1_0$ phase, respectively. The dark fringes within the bright domains are anti-phase domain boundaries [11].

FCC A1 \rightarrow L1₂: When the FCC to L1₂ transformation takes place, large L1₂ domains form with anti-phase boundaries separating the L1₂ anti-phase domains as shown in Fig. 2.15. Note that the microstructure shows three types of APBs that are visible/invisible in DF images taken with different g-beam/diffraction spot, according to the defect-visibility criterion.

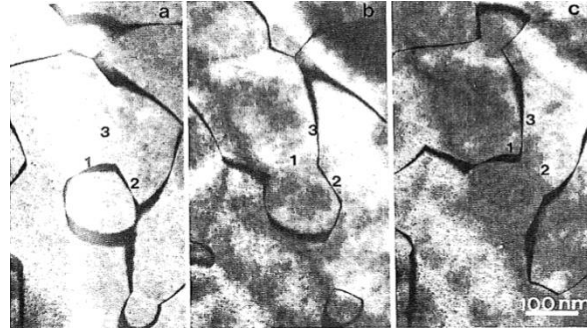


Figure 2.15: Dark field images of APBs in CoPt₃ (L1₂) phase of a Co₃₀Pt₇₀ alloy oriented along [001] zone axis: (a) 110 DF, (b) 010 DF, (c) 100 DF [37].

FCC A1 \rightarrow L1₀ + L1₂: As mentioned previously, the eutectoid decomposition of Co-Pt: FCC \rightarrow L1₀ + L1₂, can lead to the formation of the nano-chessboard microstructure. This coherent microstructure results from strain-driven self-arrangement of the L1₀ and L1₂ phases. Microstructural evolution is dictated by the minimization of the surface energy and the coherency strain energy arising from the disorder-order transformation [13]. It has been shown that the formation of the nano-chessboard structure via eutectoid decomposition in Co-Pt alloys proceeds by a pseudo-spinodal decomposition reaction in which the composition of the product phases gradually changes to achieve their final equilibrium composition [13], [32], [38].

Le Bouar et al. [13] investigated this phase transformation both theoretically and experimentally. Their results suggest that the phase transformation starts with the formation of L1₀ nuclei aligned

along the $\langle 110 \rangle$ directions giving rise to tweed contrast as shown in Fig. 2.16 (a), (d). In the next stage, $L1_0$ structural domains of irregular shape and size can be seen, aligned along $\langle 110 \rangle$ direction, as shown in Fig. 2.16 (b), (e). They predicted that the APBs would be destroyed in the initial stages of thermal aging, being energetically unfavorable compared to the matrix-precipitate interfaces. Upon further aging, the structural domains finally assume a diamond-shape with facets normal to elastically soft directions, as shown in Fig. 2.16 (c), (f). These diamond-shaped $L1_0$ tiles are arranged in alternating bands/rows. In each row, the $L1_0$ tiles have same c -axis orientation while the tiles in the adjacent rows alternate the c -axis orientation indicated by black arrows in Fig. 2.16 (c); these bands/rows of tiles vary in size. Ideally, with continued annealing, the tiles become nearly homogeneous in size and shape. This is a metastable state that can be destroyed by coarsening, which proceeds by the disappearance of rows of tiles. The theory of Le Bouar et al. does not explain how the disordered cubic matrix transforms to $L1_2$ but focuses on annealing in the $A1 + L1_0$ coexistence region.

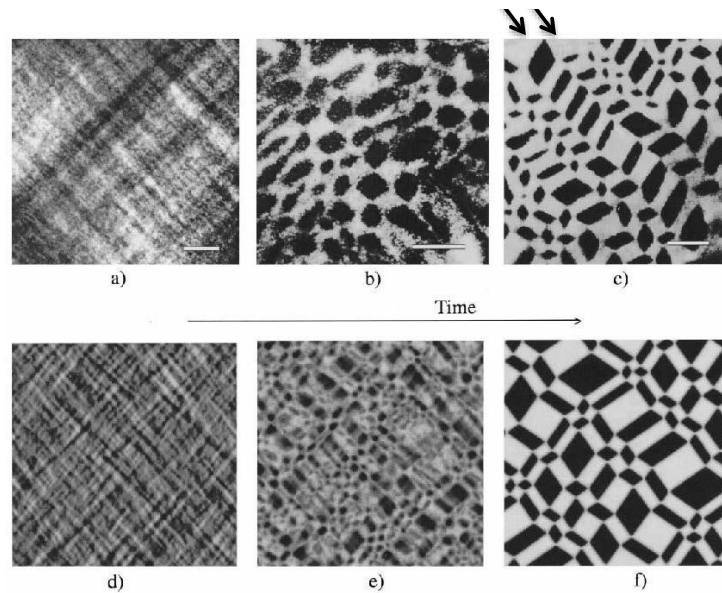


Figure 2.16: Evolution of nano-chessboard structure: (a)-(c) Experimental TEM images of a $\text{Co}_{39.5}\text{Pt}_{60.5}$ alloy, (d)-(f) Corresponding simulated images [13].

Yong Ni et al. [32] specifically studied the pseudo-spinodal decomposition of the homogeneous cubic phase into cubic-tetragonal two-phase chessboard structure. They established that the pseudo-spinodal decomposition is a necessary thermodynamic condition for the stress-minimizing nucleation of the tetragonal phase required to produce the compositionally inhomogeneous tweed structure. And, the tweed structure, in turn, is a pre-requisite for the formation of the chessboard nano-rods. As a result, the formation of the chessboard structure is sensitively dependent on temperature and composition. Their simulations show that at the later stage of annealing, the tweed structure decomposes by precipitation of the equilibrium cubic phase, which eventually produces the two-phase chessboard structure as shown in Fig. 2.17.

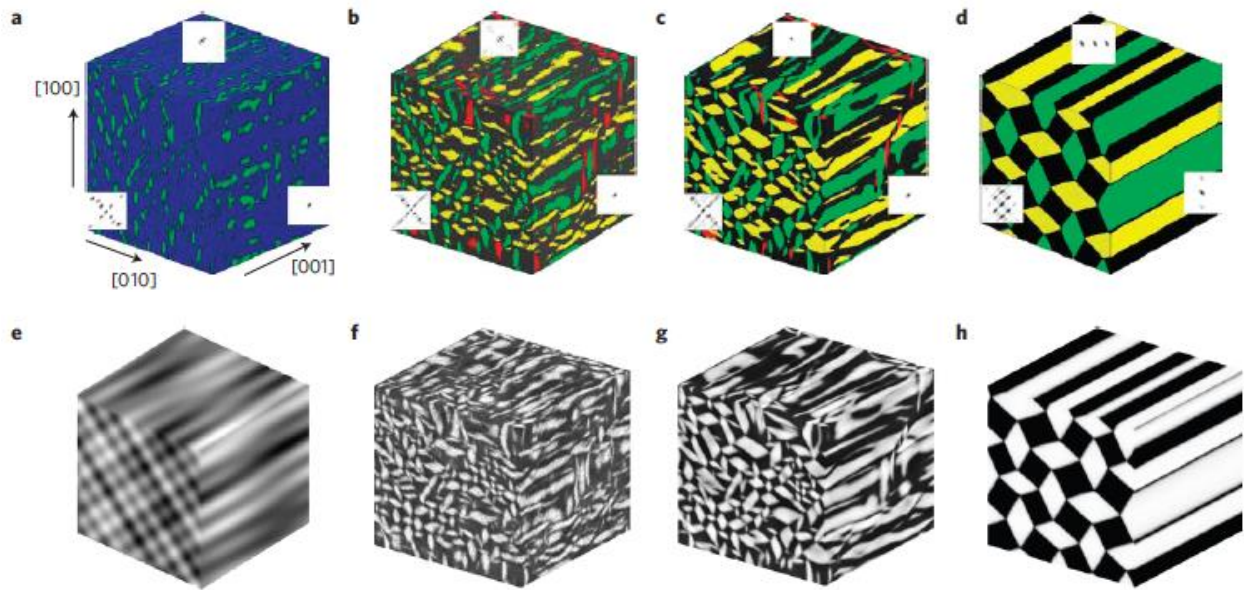


Figure 2.17: Simulated 3-D microstructure development: (a) The tweed structure formed at the initial stage of the phase transformation; green color indicates tetragonal domains with the [100] direction of the c-axis; blue describes the cubic phase and domains of tetragonal phase with other orientations, (b)-(d) Structures formed by decomposition of the tweed structure; their different colors indicate tetragonal phase with different orientations of the tetragonality axes; the black color describes the cubic phase, (e) the filtered ‘low-resolution’ image of green domains of (a), (f)-(h) The composition profile of the structures in (b)-(d) described by different grey levels (black and white are the limiting cases of the equilibrium compositions of the cubic and tetragonal phases) [32].

2.3 Magnetic Ordering Transformation

The magnetic ordering transformation takes place when the magnetic material is cooled down below a temperature known as the Curie temperature (T_c). For ferromagnetic materials this transformation is also called the paramagnetic to ferromagnetic transformation (Fig. 2.18). Ordering of atomic moments reduces the magnetic symmetry of the material, which leads to the formation of magnetic domains and domain walls. The origin of magnetic domains will be explained in detail in Section 2.3.2. The order parameter for this transformation is the reduced magnetization, $m(T) = M_s(T)/M_s(0)$, where $M_s(T)$ is the spontaneous magnetization of the material at a given temperature T . Above T_c , magnetic moments point in random directions due to thermal energy and the net magnetization is zero. However, M increases as the temperature decreases and achieves a maximum value $M_s(0)$ at 0 K, as shown in Fig. 2.19 [39]–[42].

Cobalt metal is known to exhibit the highest Curie temperature of 1388 K [41]. The Curie temperature depends on factors including the composition of the material/alloy, magnetic and chemical interactions between atoms, as well as the prior thermal treatments. For example, the Curie temperature of a disordered alloy can be substantially different from that of the ordered or partially ordered alloy [6], [43], [44]. Similarly, the saturation magnetization also varies with chemical composition. Table 2.1 summarizes the Curie temperature and saturation magnetization of the ordered phases of Co-Pt alloys.

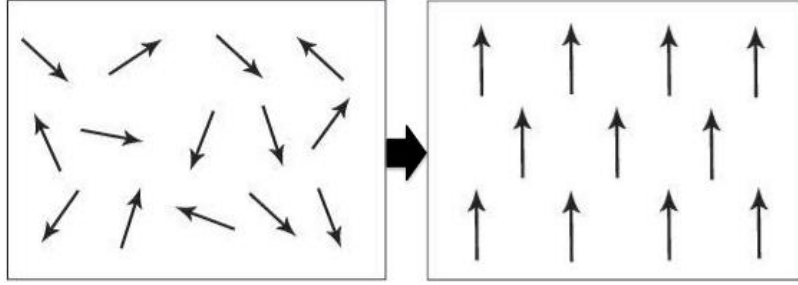


Figure 2.18: Ordering of magnetic moments leading to paramagnetic-to-ferromagnetic transformation.

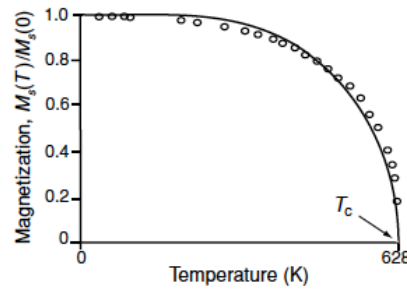


Figure 2.19: Temperature dependence of the spontaneous magnetization (Order Parameter) of nickel. The Curie point at 628 K is marked [39].

Table 2-1: Curie temperature and saturation magnetization of Co-Pt alloys [25], [44].

Phase	M_s (emu/cm ³)	T_c (K)
CoPt L1 ₀	800	840
CoPt ₃ L1 ₂	1140	292

2.3.1 Magnetic moment and magnetization

The magnetic dipole moment is an intrinsic property of a magnet and it has its origin in circulating electrical charge. It has two major contributions:

1. Moment due to the spin of the electron about its axis (spin angular momentum).

2. Moment due to the orbital motion of the electron around the nucleus of the atom (orbital angular momentum).

In addition, the electrons can interact with each other as well as with the nucleus, leading to “coupling”. Coupling can be of three types:

1. Spin-Orbit Coupling: the magnetic field from the electron’s spin interacts with the magnetic field from its movement around the nucleus;
2. Spin-Spin Coupling: the spin of the neighboring electrons interact;
3. Orbit-Orbit Coupling: the electrons of neighboring orbitals interact.

The total magnetic moment of a magnetic material is the sum of the contributions from all types of coupling. The unit for electron magnetic moment is the Bohr magneton (μ_B), defined as:

$$\mu_B = \frac{e\hbar}{2m_e}, \quad (2.1)$$

$$1\mu_B = 9.274 \times 10^{-24} \text{ A}\cdot\text{m}^2 \text{ [39].}$$

The magnetization (M) is given as the vector sum of the dipole moments of all the atoms divided by the volume, $M = \frac{\sum \text{Dipole moments}}{\text{Volume}}$. It is an extrinsic property of a magnetic material and it depends on the constituent atoms, their respective dipole moments and how the dipole moments add together [45]. The value of the magnetization, M , when all of the dipoles are aligned is called the saturation magnetization, M_s . Another fundamental quantity in magnetism is the magnetic flux density or magnetic induction, denoted as “ B ” and it represents the magnitude of the internal field strength within a substance that is subjected to an external field H . B and M are related as $B = \mu_0(H + M)$, where μ_0 is the permeability of vacuum. Furthermore, the permeability of the

material is described as the response of the material to the applied field H and is expressed as $\mu = B/H$. Permeability is strongly structure sensitive and so depends on composition, thermal treatments, deformation etc. [39].

In Co-Pt alloys, the bulk of the magnetic moment is concentrated on Co atoms ($\mu_{Co} = 1.76 \mu_B$ per atom) [46]. Pt is paramagnetic, but in structures where Pt is in contact with ferromagnetic species, it can also have an appreciable moment. Large induced moments on Pt atoms ($\mu_{Pt} = 0.35 \mu_B$ per atom) have been observed in Co-Pt alloys [46]. The dipole moment for Pt atoms is induced by polarization effects mediated by conduction electrons and through direct exchange interaction with Co atoms [47]. It should be noted that the induced magnetic moment of Pt atoms in Co-Pt alloys depends sensitively on composition and local chemical environment [6]. Such induced moments on non-magnetic atoms have also been observed in other ordered alloys, for example an induced moment of $0.32 \mu_B$ is observed in Pt atoms in the Fe-Pt ordered alloy while the Fe atoms contribute a moment of $2.78 \mu_B$ per atom [48].

2.3.2 Micro-magnetic theory and magnetic domains

In the demagnetized state, a ferromagnetic sample is divided into domains/regions in which each of the domains has the same spontaneous magnetization magnitude. However, the net magnetization of the sample is zero since the magnetization vectors are randomly aligned in various regions. We can define magnetic domains as regions with a uniform direction of the magnetization; the boundary between different magnetic domains is called a magnetic domain wall. Magnetic domains form due to the reduction of symmetry associated with the ordering of magnetic moments as a result of the paramagnetic-to-ferromagnetic transition. However, the

specific arrangement of domains, i.e., the size, shape of domains and domain walls, is dependent on the various energies associated with the ferromagnetic state. This can be explained using the static micro-magnetic domain theory described below [49], [50]. The concept of static micro-magnetism is based on the following principles:

1. the local direction of the atomic magnetic moments is described by the magnetization $\mathbf{M}(\mathbf{r})$ which is a continuous function of position. The amplitude of the magnetization vector $\mathbf{M}(\mathbf{r})$ has to be constant but its orientation may change with position,

$$|\mathbf{M}(\mathbf{r})| = M_s |\mathbf{m}(\mathbf{r})| = M_s, \quad (2.2)$$

where M_s is the saturation magnetization and $\mathbf{m}(\mathbf{r})$ is the unit vector of magnetization.

2. the magnitude of the magnetization is a function of temperature only. The modulus of the magnetization,

$$|\mathbf{M}(\mathbf{r}, T)| = M_s(\mathbf{r}, T) \quad (2.3)$$

is assumed to be a function of temperature and to be independent of the local magnetic field. M_s may depend on position as in a two-phase nanostructured magnet [8].

The contributions to the total magnetic Gibbs free energy can be expressed as the continuous energy expressions that describe the interactions of the spins with the external field, the crystal lattice, and the interactions of the spins with one another. These energies are:

1. Exchange energy (E_{ex}),
2. Magnetostatic energy (E_d),
3. Magnetocrystalline anisotropy energy (E_{ani})
4. Zeeman energy (E_z)

The first three energies are always present to some extent in a ferromagnet. The fourth is the response to an applied field, and it defines the magnetization process and hysteresis loop. There are two other contributions to the magnetic energy, namely the energy due to an applied stress (E_s), and magnetostriction (E_{ms}), which are neglected for now because the associated energies are small.

Exchange energy (E_{ex}) arises due to the interaction between the spins of neighboring atoms and it is an energy penalty generated by the deviation of magnetization directions of adjacent atoms. Magnetostatic energy (E_d) is the energy associated with the stray field/demagnetizing field (\mathbf{H}_d), which originates due to the continuity of magnetic flux in a magnet. In general, a ferromagnetic material does not show isotropic magnetization behavior. Certain directions favor magnetization (easy axes) and others do not (hard axes). This leads to a new energy term called magnetocrystalline anisotropy energy (E_{ani}), which arises when the magnetization is not oriented along the easy axes. It is expressed as a direction dependent energy term f_{ani} . For example, in the case of hexagonal systems (e.g., Co) a uniaxial anisotropy is found. Therefore f_{ani} can be expressed as a series expansion [41]:

$$f_{ani}(\theta) = K_0 + K_1 \sin^2 \theta + K_2 \sin^4 \theta + \dots \quad (2.4)$$

The angle θ denotes the angle between \mathbf{M} and the easy axis (c-axis) of the hexagonal system and K_0 , K_1 , K_2 etc., are the so called anisotropy constants. In practice, all higher order terms are neglected. K_0 can be neglected since it is not dependent on angle and is therefore a constant term. In most cases, including up to second-order terms of this expansion is sufficient to evaluate the anisotropy energy and it has different forms for different crystal systems. The Zeeman energy (E_z) is the energy associated with a magnetized body in the presence of an external field (\mathbf{H}_{ext})

and is minimized when the magnetization direction aligns itself along the direction of the external field. The expressions of these energy densities are summarized in Table 2.2 [49].

Table 2-2: Magnetic energy expressions as a function of the unit magnetization vector $\mathbf{m}(\mathbf{r})$, A (J/m) is the exchange stiffness constant [49].

Energy term	Energy expression
Exchange energy	$E_{ex} = A(\nabla\mathbf{m})^2$
Magnetostatic energy	$E_d = -\frac{1}{2}\mu_0 M_s(\mathbf{m} \cdot \mathbf{H}_d)$
Magnetocrystalline anisotropy energy	$E_{ani} = f_{ani}(\mathbf{m})$
Zeeman energy	$E_z = -\mu_0 M_s(\mathbf{m} \cdot \mathbf{H}_{ext})$

The total Gibbs free energy, which is an integral over the total volume of the magnetic sample, can be written as:

$$E_{total} = E_{ex} + E_d + E_{ani} + E_z = E(\mathbf{m}(\mathbf{r})), \quad (2.5)$$

$$E(\mathbf{m}(\mathbf{r})) = \int [A(\nabla\mathbf{m})^2 - \frac{1}{2}\mu_0 M_s(\mathbf{m} \cdot \mathbf{H}_d) + f_{ani}(\mathbf{m}) - \mu_0 M_s(\mathbf{m} \cdot \mathbf{H}_{ext})] dV, \quad (2.6)$$

The competitive effects of the micro-magnetic energy contributions upon minimization determine the equilibrium distribution of the magnetization. The minimization of the ferromagnetic exchange energy aligns the magnetic moments parallel to each other, whereas the minimization of the magnetostatic energy favors the existence of magnetic domains. The magnetocrystalline anisotropy energy minimization orients the magnetization preferably along certain crystallographic directions. The minimization of the Zeeman energy of the magnetization in an external field rotates the magnetization parallel to the applied field.

The arrangement of a magnetic domain structure can be explained using Fig. 2.20. Due to exchange coupling, all the atomic moments would like to align themselves in one direction and as a result, a single magnetic domain is preferred; this configuration reduces the exchange energy. The magnetization lies along an easy axis to reduce the magnetocrystalline anisotropy energy (MAE). However, if a material consists of a single magnetic domain there is a strong “demagnetizing field” around it giving rise to very high magnetostatic energy. This energy needs to be minimized in order to reduce the total magnetic energy. This can be achieved by forming two domains with opposite direction of magnetization separated by a 180° domain wall. Adding extra domains increases the exchange energy since the moments cannot align parallel. Furthermore, the demagnetizing field can be completely reduced to zero if the symmetry of the crystal allows for 90° domain walls. For example, cubic crystals have easy axes along $\langle 100 \rangle$. Since both the 180° and 90° domains are along the easy axes, the MAE is minimized for this configuration. However, this configuration will lead to more domain walls inside the sample increasing the domain wall energy or exchange energy. In the case of uniaxial crystals, such as hexagonal or tetragonal, the dipole moment of the closure domain will lie along the hard direction, which will increase the MAE. In addition, the direction of magnetization gradually changes in the regions bounding the domains, the domain walls. Therefore, moments inside domain walls cannot be aligned along easy axes and so large magnetic domains with few domain walls minimize the MAE. In conclusion, the final magnetic microstructure will be decided by the combined minimization of the above-mentioned energies.

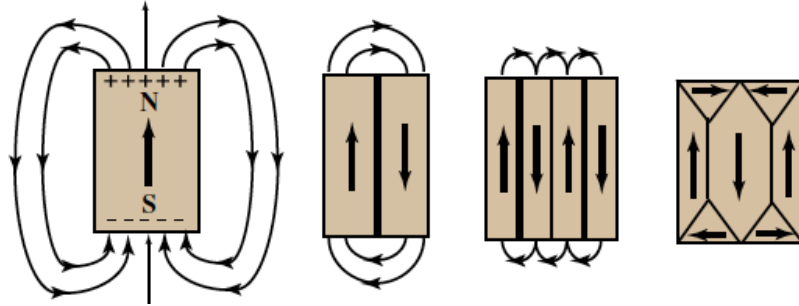


Figure 2.20: Schematic showing the reduction in the demagnetization field as a result of the introduction of magnetic domains into a ferromagnetic sample [42].

The detailed description of magnetic concepts and quantities that are relevant to this work is given below.

Magnetocrystalline anisotropy: The magnetocrystalline anisotropy arises from the fact that crystalline materials tend to magnetize easily along some crystallographic directions while it is hard to magnetize the crystal in other directions. These directions are called easy and hard axes of magnetization. Magnetocrystalline anisotropy energy (MAE) is the energy difference between material magnetized along the easy and hard directions. It should be noted that the saturation magnetization is the same for both directions but the external applied field required to reach this value is different. Fig. 2.21 shows the easy and hard directions along with M-H curves for three ferromagnetic materials Iron (BCC), Nickel (FCC) and Cobalt (HCP).

When a magnetic field is applied to a material, the atomic orbitals must reorient themselves in order to reorient the direction of the electron spin along the applied field; this is due to the spin-orbit coupling (SOC). However, the atomic orbitals are strongly coupled to the crystal lattice and so resist the change in orientation. The spin-orbit coupling is weak in most of the magnetic

materials. However, in some materials, the coupling is strong and the resistance to re-orientating the domains away from the easy crystallographic directions is high and requires a large coercive field. Hence, SOC is dominant in determining the easy axis of magnetization as well as the MAE in most magnetic materials [39], [51], [52].

Strong uniaxial magnetic anisotropy is a prerequisite for hard magnetism while a near-zero anisotropy is desirable for soft magnets. Magnetocrystalline anisotropy decreases with increasing temperature, until at temperatures approaching the Curie temperature there is no preferred orientation of the magnetization. In ferromagnetic solids, MAE is known to closely depend on composition, atomic ordering, and magnetic interactions between atoms [43], [51]. The disordered Co-Pt phase has the easy axis along $\langle 111 \rangle$ direction and is a soft ferromagnet. The L_{12} ordered phase is known to be a soft ferromagnet with easy axis along $\langle 100 \rangle$ direction while the L_{10} tetragonal phase is a uniaxial hard ferromagnet with easy axis along $[001]$ direction and uniaxial anisotropy constant K_u of 4.9×10^7 ergs/cm³ [24]. The MAE of Co-Pt alloys is strongly dependent on the Pt concentration due to a strong SOC between Pt and Co atoms [7], [43], [51]. The maximum anisotropy has been reported for the equiatomic Co-Pt alloy [24]. The FCC \rightarrow FCT transformation also contributes to an increased anisotropy in uniaxial alloys [43].

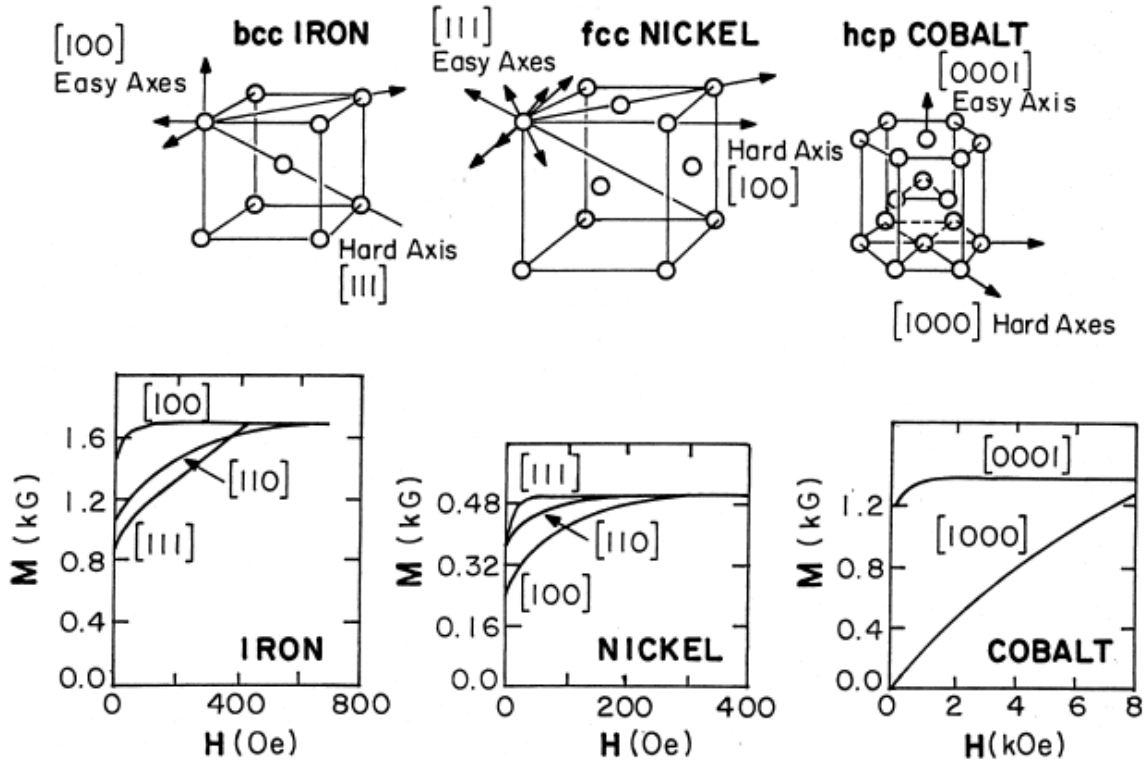


Figure 2.21: Crystal structures of Fe, Ni, and Co showing easy and hard magnetization directions with corresponding magnetization (M-H) curves shown below [41].

Exchange coupling: Exchange interactions are electrostatic interactions that decide the preference in a magnetic material for neighboring spins to align parallel or antiparallel to each other. This is also called direct exchange and it results from the overlap of orbitals responsible for magnetic moments. The interaction between neighboring atoms can be expressed in terms of an exchange energy expressed as:

$$E_{ex} = -2 \sum_{i>j} J_{ij} S_i \cdot S_j \quad (2.7)$$

Here, the spins are denoted as S_i , S_j , being 1 for spin up and -1 for spin down orientations; J_{ij} represents the exchange interaction strength. $J_{ij} > 0$ in ferromagnetic materials and the total energy is minimized if spins S_i , S_j are oriented in the same direction hence the exchange

interaction favors the parallel alignment of neighboring spins. In antiferromagnetic materials, the exchange interaction ($J_{ij} < 0$) favors antiparallel alignment of neighboring spins. The interplay between electron-electron Coulomb interactions and the constraints of the Pauli exclusion principle determine the sign of the exchange interaction and can be predicted by the Bethe Slater curve (Fig. 2.22) in 3d transition metals. It should be noted that the Pauli exclusion principle allows parallel spins at long interatomic distances but requires antiparallel spins at short separations. In 3d transition metal solids, the ratio of the interatomic separation (near-neighbor distance) to the diameter of the 3d orbit describes the amount of orbital overlap (or exchange). The negative exchange for Manganese, Mn solids can be explained in terms of smaller interatomic spacings relative to the d-orbital diameter. However, if the inter-atomic spacing of non-magnetic materials such as Mn changes because of an order-disorder transition, the sign of the exchange interaction could change from negative to positive making it ferromagnetic. This behaviour is observed in Heusler alloys [40]. Because Mn atoms are farther apart in the ordered alloys than in pure Mn, r_a/r_{3d} becomes large enough to make the exchange interaction positive. The exchange energy is minimum if all the neighboring spins lie in one direction. However, it increases (more positive) if the angle between the directions of neighboring spins increases, for example inside a domain wall [40].

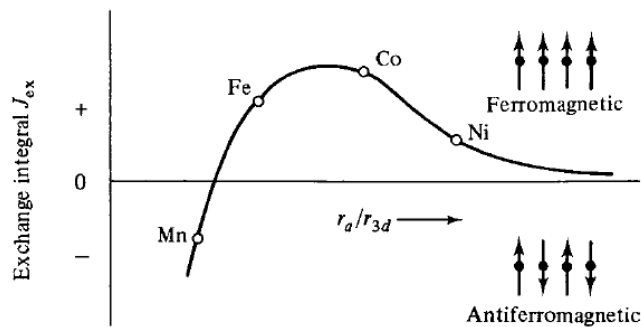


Figure 2.22: Schematic Bethe Slater curve [40].

Domain wall width: As described previously, the formation of magnetic domains is unavoidable in a ferromagnetic material. The ferromagnetic material is divided into a number of domains in its demagnetized state. The domain walls can be termed as magnetic defects since the magnetic properties are different inside a domain wall as compared to the bulk. The domain wall is usually associated with an energy that decides the type and size/width of a domain wall. The magnetization can change abruptly from one domain to the other domain as shown in Fig. 2.23 (a). This will lead to a very high exchange energy across the domain wall: $E_{ex} = -2JS^2$ or $+2JS^2$. This energy can be minimized if the transition from one domain to the other domain occurs smoothly as shown in Fig. 2.23(b). However, in this case all the spins in the wall are not aligned along the easy direction. This means there will be associated MAE. In other words, the exchange energy favors wide walls where adjacent magnetic moments can be as close to parallel as possible, whereas the magnetocrystalline anisotropy energy favors sharp changes in the magnetic moments between the favored directions in the crystal so that as few magnetic moments as possible point along “non-easy” directions. The actual domain wall width is determined by the minimization of the total domain wall energy, which is a sum of:

1. Exchange Energy
2. Magnetocrystalline Anisotropy Energy

The domain wall-width varies from about 1 nm in extremely hard materials to several 100 nm in very soft materials. The magnetic domain wall energy and the domain wall width can be expressed as a function of the exchange stiffness constant (A) and the magnetocrystalline anisotropy constant (K_1) as shown in Table 2.3.

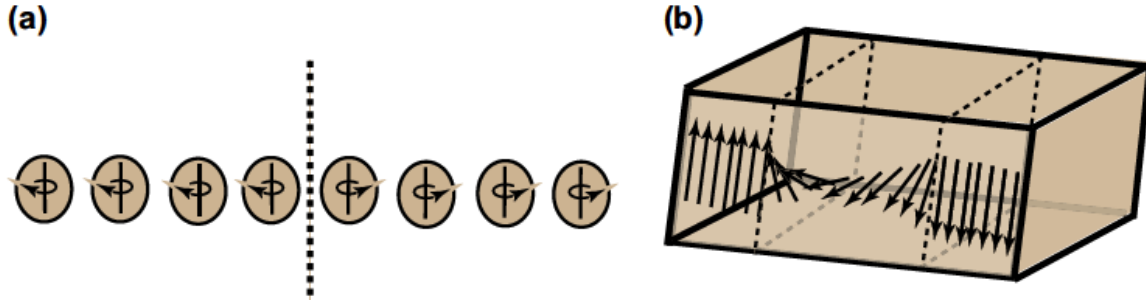


Figure 2.23: Magnetic domains separated (a) by an infinitely narrow domain wall, (b) by a domain wall with finite width [42].

Table 2-3: Magnetic quantities [9], [42], [53], [54].

Magnetic domain wall width (δ)	$\pi \sqrt{\frac{A}{K_1}}$
Magnetic domain wall energy (γ)	$4\sqrt{AK_1}$
Single domain particle size (R_{SD})	$\frac{36\sqrt{AK_1}}{\mu_0 M_s^2}$

Two types of domain wall are commonly observed in many magnetic materials; one is the Bloch wall and the other is the Néel wall. Fig. 2.24 (a) shows a 180° Bloch wall, where the magnetization rotates 180° from one easy direction to another in the plane of the wall [40], [41]. On the contrary, in the Néel wall (Fig. 2.24 (b)), the magnetization rotates within the plane of the domain magnetization and does not remain parallel to the wall plane. Bloch walls are usually observed in thick/bulk materials since the magnetostatic energy due to the surface charge above and below the wall is negligible, resulting in comparatively lower energy than Néel walls. As the film thickness becomes comparable to the thickness of the domain wall, surface charges would

appear inside the sample resulting in a smaller contribution to the magnetostatic energy at the interface of the wall than at the top surface [41]. So, Néel walls are preferred in thin magnetic films [40], [41].

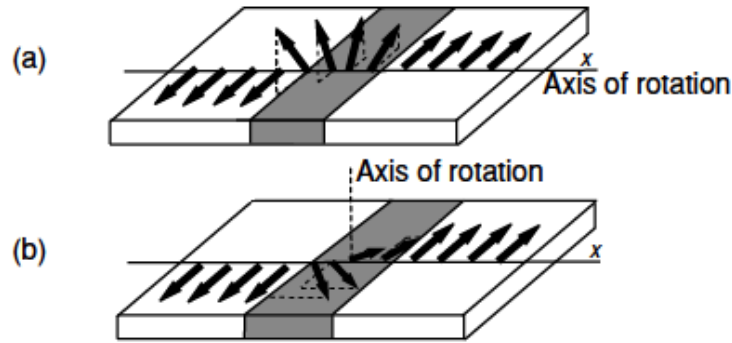


Figure 2.24: Schematic figure: (a) a 180° Bloch wall, (b) a Néel wall [39].

Single domain particle size: The contributions from exchange energy (domain wall energy) and magnetostatic energy help determine whether it is energetically favorable for a particle to exist as a single domain or a multi domain particle. Magnetostatic energy can be minimized in a particle/sample by including a large number of domain walls, separating small magnetic domains. On the contrary, making domains larger minimize the exchange energy, thereby allowing only a few domains walls in a given sample. Hence, a critical single-domain radius of spherical particles, above which a multi-domain state is more favorable than the single-domain state is given by R_{SD} and its value as a function of K_1 , A , and M_s is given in Table 2.3. Very small magnetic particles must be single-domain; they do not benefit energetically from wall formation if they are below a certain critical size [54]. Single magnetic domain nano particles have been observed in an equiatomic Co-Pt alloy with a large uniaxial magnetocrystalline anisotropy constant of 4.1×10^7 ergs/cm³ and a low saturation magnetization [55].

2.3.3 Exchange coupling in two phase nano-composites

Nano-composite materials consisting of two suitably dispersed ferromagnetic and mutually exchange coupled phases, one of which is a hard magnetic phase while the other is a soft magnetic phase, could provide optimum magnetic properties desirable for permanent magnets and high density magnetic storage media. The hard magnetic phase (high magnetocrystalline anisotropy, K_u) provides a high coercivity (H_c) while the soft magnetic phase provides a high saturation magnetization (M_s). The soft and hard phases will magnetize independently in the absence of inter-phase exchange coupling, for instance, if the size of the soft phase is sufficiently large. However, when the two phases are exchange coupled, the material can behave as a single magnetic phase yielding a high-energy product BH_{max} and a high remanence ratio, $M_r/M_s \geq 0.5$. A reversible demagnetization curve (exchange spring behavior) is also expected from such nano-composite systems [10], [56]. The factors that govern the exchange coupling include magnetic properties, volume fractions, size and distribution and the nature of the interface between the constituent phases [10].

Kneller and Hawig theoretically described exchange coupling in two-phase nano-composite structure [56]. They derived critical length scales of the corresponding phases necessary for the phenomenon of exchange coupling to occur. The exchange coupling between the two phases necessitates that the phases must emerge from a common metastable matrix phase in order to be crystallographically coherent and consequently magnetically exchange coupled. Coherent inter-phase boundaries/interfaces help improve the coupling. The optimum microstructure should be a homogeneous distribution of the hard phase in a magnetically soft matrix, with the lateral dimensions of both phases being about equal and equal to the critical diameter of the hard phase,

$b_k = b_m = b_{ck} = b_{cm}$ (Fig. 2.25). Here b_k is the diameter of the hard phase, b_m is the diameter of the soft phase; b_{ck} and b_{cm} are the critical diameter of the hard and the soft phases respectively, as predicted by Kneller and Hawig. The critical diameter b_{cm} is given by:

$$b_{cm} \approx \pi \left(\frac{A_m}{2K_k} \right)^{1/2} \quad (2.8)$$

Here, A_m is the exchange constant of the soft phase and K_k is the magnetocrystalline anisotropy constant of the hard phase. The magnetization of the soft phase is exchange coupled with the magnetization of the hard phase along their mutual phase boundaries. If the size of the soft phase is sufficiently large, the soft and the hard phases would reverse independently upon applying a demagnetizing reverse field. However, when the size of the soft phase is reduced below a critical value b_{cm} , the soft phase particles become too small to support a domain wall and the magnetization of both phases would switch coherently by rotation as if a single magnetic phase is present. Fig. 2.26 shows the schematic hysteresis loops for the hard magnetic phase, soft magnetic phase, and the exchange coupled composite comprising the hard and the soft phases.

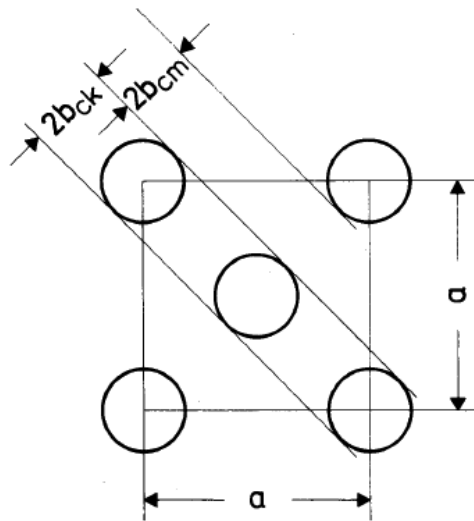


Figure 2.25: Schematic model of optimum microstructure suitable for exchange coupling [56].

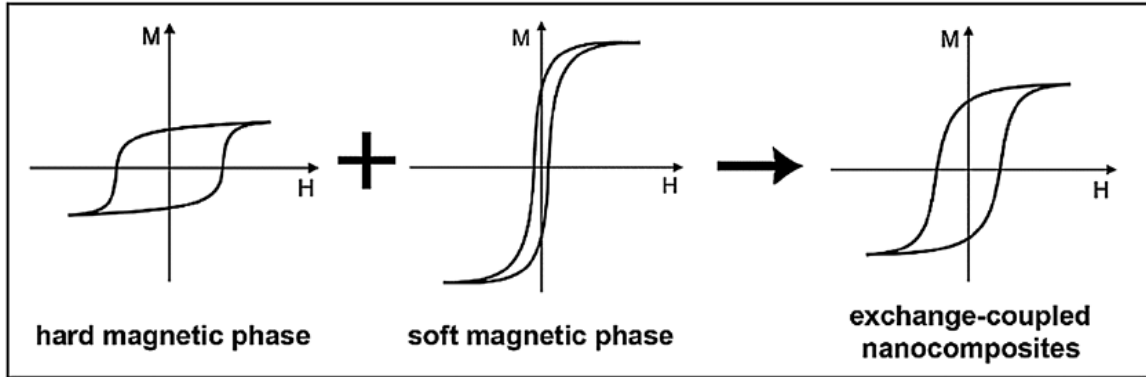


Figure 2.26: Schematic Hysteresis loops of hard magnetic phase, soft magnetic phase, and exchange coupled composite of the hard and the soft phases [10].

The Co-Pt eutectoid system is a good candidate for the exchange coupled nanocomposite since the hard $L1_0$ and the soft $L1_2$ phases emerge from a common matrix phase and are distributed on a fine scale and have coherent interfaces. The exchange coupling between the hard ferromagnetic $L1_0$ and soft ferromagnetic $L1_2$ phases should ideally result in improved magnetic properties. The $L1_2$ phase enhances the remanence, owing to its high saturation magnetization, while the $L1_0$ phase results in a larger coercivity. Ghatwai et al. studied the effect of composition and the effect of length scale of the soft and the hard phases on exchange coupling behavior in near eutectoid Co-Pt alloys using TEM microstructural studies and magnetic hysteresis curves [12], [57]. Vetter et al. studied the exchange coupling behavior of nano-chessboards in $Co_{40}Pt_{60}$ alloys using First Order Reversal Curves (FORCs) and micro-magnetic simulations [14], [58].

2.3.4 Magnetic microstructure in $L1_0$ alloys

Zhang & Soffa studied the magnetic microstructure of equiatomic Fe-Pd alloy [33]. Fig. 2.27 shows a Lorentz Fresnel under-focus image of a $L1_0$ Fe-Pd alloy. Four macro domain walls can be observed in the figure; two are “frozen” on the macro-twin boundaries and two kinked walls

are seen cutting across the assembly of micro-twin plates inside macro-twins. The thin bright and dark lines of contrast are coincident with the traces of (101) and (011) micro-twin boundaries and can be called micro magnetic domain walls. The thick bright and dark lines of contrast are the magnetic domain walls associated with the crystallographically imposed spin transition from one macro-twin plate to another. The serrated or kinked walls, shown by black arrows, are the 180° macro-domain walls cutting across the array of micro-twin plates. These walls are expected to be mobile and play a primary role in magnetic domain wall motion [33].

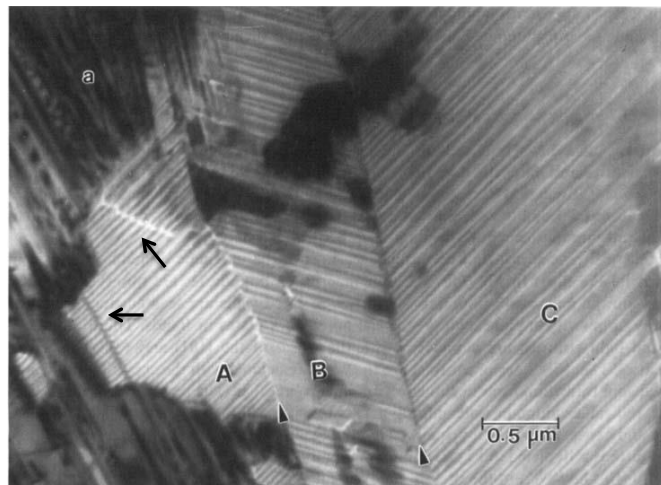


Figure 2.27: Fresnel under-focus image showing macro-domain and micro-domain structures in the aged Fe-Pd alloy [33].

Wang et al. [15] studied the magnetic domain structure of a non-equiatomic Fe-Pd alloy at different stages of atomic ordering using Lorentz Fresnel imaging mode and coercivity measurements obtained through a vibrating sample magnetometer (VSM). Fig. 2.28 (a) and (b) show the under-focus (UF) and over-focus (OF) images of the magnetic domain walls in the tweed microstructure. Magnetic domain walls can be seen as alternate bright and dark lines that can be seen to reverse contrast in the UF and OF images. Both the magnetic micro-domains and

magnetic macro-domains can be seen. The magnetic micro-domain walls are coincident with the micro-twin boundary (110) or the boundary between finely arranged plate shape c-variants. Only two directions of the boundaries are present in these two micrographs. The magnetic macro-domain walls pass through the boundaries of these c variants or $L1_0$ variants and each magnetic macro-domain wall intersects with a large number of magnetic micro-domain walls. It is found that in the tweed microstructure, all three $L1_0$ variants are present. These $L1_0$ variants align themselves along (110) twin plane traces [34]. VSM measurements showed a high coercivity for this sample with a tweed structure and the authors attributed it to the higher density of the intersection between the magnetic macro-domain walls and the c-variants [15].

Fig. 2.28 (c) shows the magnetic micro-domain walls and macro-domain walls in the poly-twinned structure. The magnetic micro-domain walls coincide with the twin boundaries, and cannot move during the magnetization process. The magnetic macro-domain walls, however, have a zigzag shape; and they can be moved during the magnetization. The zigzag domain walls pass through the micro-twin and macro-twin variants. Fig. 2.28 (d) shows the magnetic domain walls in the coarsened $L1_0$ grains. Two types of magnetic microstructure are observed depending on the orientation of the c-axis in the $L1_0$ grains. Stripe domains seen in the center grain are observed when the magnetization direction (c-axis) is perpendicular to the sample plane. The alternate 180° domain walls are observed when the easy axis of magnetization is in the plane of the sample or the c-axis of the grain lies in the plane.

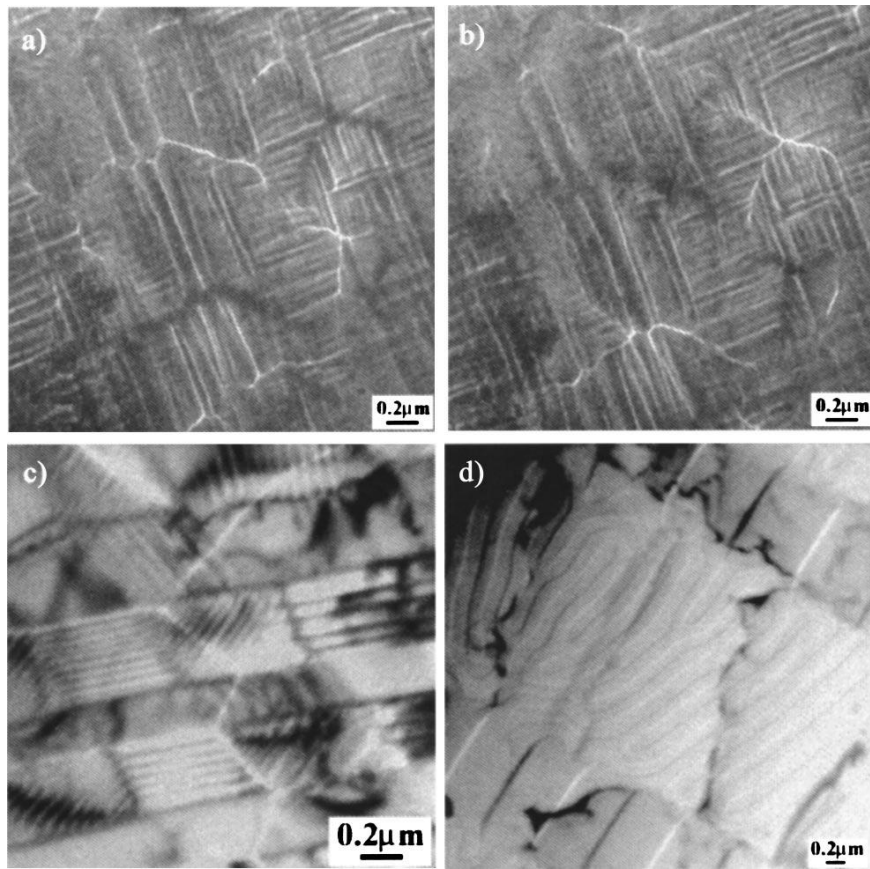


Figure 2.28: The magnetic domain structure of Fe-55%Pd after annealing: (a) & (b) Lorentz under-focus and over-focus Fresnel image of tweed microstructure, (c) Lorentz under-focus Fresnel image of poly-twinned microstructure, (d) Lorentz under-focus Fresnel image of coarsened $L1_0$ grains [15].

In the next Chapter, we describe experimental transmission electron microscopy techniques, simulation techniques, and quantitative data extraction procedures that have been employed in this work to study the magnetic and crystallographic structures of Co-Pt alloys.

3 Experimental and Simulation Techniques

3.1 Introduction

Transmission Electron Microscopy (TEM), first developed in the 1930s [59], is a highly versatile characterization technique, used for high-resolution microscopy and as an analytical tool. It exploits the small wavelengths of high-energy electrons to probe materials at the nano-meter scale. Information about local structure (by imaging of defects such as dislocations, stacking faults), average structure (using diffraction pattern to identify crystal structure and lattice parameter) and chemical composition may be collected almost simultaneously. TEM can be used to study a wide variety of materials including metals, ceramics, polymers, biomaterials and semiconductors. We are now able to obtain resolution down to atomic length scales owing to improvements in magnetic lenses, stability of high voltage sources, and a thorough understanding of various lens aberrations and corrections [60], [61].

When used in the so-called Lorentz mode, TEM can be used to study magnetic features [62]. While other characterization techniques such as Bitter technique [63], Kerr microscopy [64], Magnetic Force Microscopy (MFM) [65] are also used for studying magnetic materials, Lorentz microscopy has emerged as the most promising method primarily due to the relatively high resolution it provides [66]. Using existing image formation theory, Lorentz microscopy has made quantitative magnetic imaging possible.

This chapter summarizes characterization and simulation techniques applied to this work. The basic imaging modes of TEM and Lorentz TEM are explained in brief. The theory behind image formation in Lorentz mode is discussed using a classical approach followed by a quantum mechanical approach. The approach to the simulation of Lorentz images is described next, followed by phase reconstruction theory, based on the transport of intensity equation. At the end, spherical aberration corrected microscopy is discussed.

3.2 Transmission Electron Microscopy

Transmission Electron Microscopy is an imaging technique based on analyzing an electron beam that is transmitted through a specimen of interest. When high-energy electrons pass through a region of specimen, the electrons interact with the atoms of the material. The electrons exiting the specimen contain information about the structure of the material. These electrons are directed towards a viewing screen or detector to form images of the specimen microstructure. The contrast in the image depends on the electron-matter interactions occurring within the specimen. In the case of crystalline materials, diffraction pattern formation is dictated by Bragg's law [67], given by $2d\sin(\theta) = n\lambda$, where d is the spacing between crystal atomic planes, θ is the angle of diffraction, and λ is the relativistic wavelength of electron.

The electron beam originating at the source (electron gun) travels down an evacuated TEM column and is focused using a series of magnetic "lenses" (pole pieces) on to the specimen. A typical TEM column can be divided into three major parts:

1. "Gun and Condenser lens" or illumination system
2. "Objective lens and Goniometer stage" or image forming system

3. “Projector lens and Detectors” or image magnification and acquisition system

In addition, a TEM operation requires a high voltage of around 200-400 kV and a high vacuum of 10^{-7} to 10^{-10} Pa [2]. Part of the electron beam focused by the condenser lenses on to the specimen, interacts with the sample and is scattered or diffracted in different directions. The objective lens focuses the diffracted beams and forms a diffraction pattern at its back focal plane and an image at the image plane. The Projector lens and other magnifying lenses further magnify the image or diffraction pattern before they are captured on the fluorescent viewing screen. Since electron transmission is critical, sample preparation is an important aspect of TEM. In general, the specimen needs to be <100 nm thick. A variety of sample preparation techniques have been developed over the years, and the user needs to select the appropriate technique based on the material and the features of interest in the specimen. Some sample preparation techniques, for example, may be better suited to imaging defects but unsuitable for compositional analysis [68].

Bright Field and Dark Field imaging: The electron interacts with the specimen and produces bright or dark contrast depending on the thickness, composition and crystallographic properties of the material being studied. Some areas of the sample scatter or absorb electrons and therefore appear dark while other areas transmit electrons and appear bright. The image obtained in this way has a very poor contrast since both the scattered and the transmitted beams are used to form the image. To get a better contrast, an aperture called objective aperture can be introduced in the back focal plane of the objective lens; this allows us to select a particular beam to form the image. The easiest way of generating an image using TEM is the Bright Field imaging mode (Fig. 3.1(a)). In this mode, the objective aperture is used to select the transmitted beam and block

all the diffracted beams and form an image that is called a true bright field image. When one of the diffracted beams is selected to form the image, we obtain a so-called dark field image as shown in Fig. 3.1(b). In a TEM, unlike light microscopy, dark field images are not typically contrast-reversals of bright field images. Features of bright contrast in dark field images depend upon the specific diffracted beam selected using the objective aperture.

Diffraction mode: The diffracted beams originating from the specimen form a diffraction pattern on the viewing screen or detector. The specific arrangement of diffraction spots in the pattern depends on the crystal structure and crystal orientation with respect to the incident electron beam. This mode of the TEM can be used to study crystal structure and crystallographic defects in the specimen. A typical diffraction pattern is obtained by selecting a small area of a sample by introducing an aperture at the image plane of the objective lens. This is called a selected area diffraction pattern (SADP). Using the double-tilt stage of the TEM, a sample can be tilted to obtain diffraction patterns at different crystal orientations. When crystal is oriented along a high symmetry axis or zone axis, a uniform diffraction pattern is obtained. The diffraction of electrons is sensitive to the local orientation of lattice planes. In the case of defects, strain fields around a defect disturb the orientation of lattice planes in its vicinity, and this gives rise to defect contrast in the TEM images.

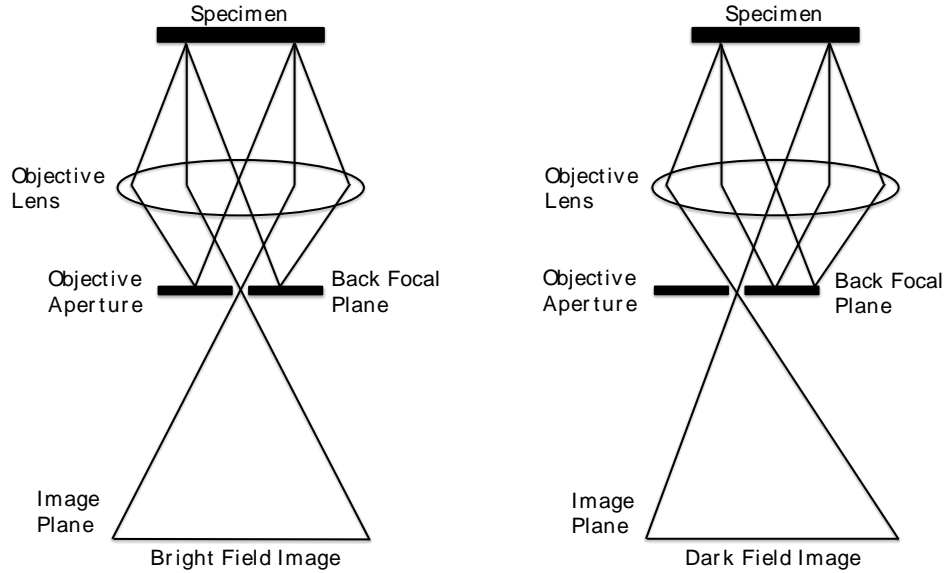


Figure 3.1: Schematic illustration of (a) Bright field mode, (b) Dark field mode.

TEM specimen preparation: TEM thin film specimens are prepared following the procedure summarized here. The 3 mm punched out discs have an initial thickness of approximately 250-400 μm . First the discs are mechanically ground on one side to a thickness of $\sim 120 \mu\text{m}$ using silicon carbide (SiC) abrasive grinding paper of grit size P1200 followed by P2400. This side is polished further using fine diamond-polishing paper of grit size 1 μm till the disc is reduced to a thickness of $\sim 100 \mu\text{m}$. Next, the non-polished side of the sample is dimpled using a dimple grinder. This step is required to selectively thin the center of the disc specimen to $\sim 15\text{-}25 \mu\text{m}$. During dimple grinding the bulk of the material is removed using 6 μm diamond polishing paste followed by 3 μm diamond polishing paste. Grinding wheel is rotated at medium speed with a load of 40g. The platform (of the grinding wheel) on which the specimen rests is also rotated to ensure uniform thinning. For the final stage of dimpling, a load of 20 g is employed to achieve smooth surface finish using 1 μm diamond paste. The specimen is then cleaned with acetone and methanol to prepare it for ion milling. A Precision Ion Polishing System (PIPS) is employed for

ion-milling the dimpled samples to electron transparency. A cold finger is utilized to perform the ion milling at a temperature of -50°C to -150°C . This ensures that any material removed by the milling process is preferentially collected on the cold finger and is not redeposited back on to the sample. During the initial stages of ion milling, both the top and bottom guns are set at an angle of 8° - 9° with incident ion energy of 4.5 KeV. The sample is rotated at a rate of 3 RPM and dual beam modulation is kept on during the entire milling process. After 30 minutes of milling, the angles are decreased to 7° and the sample is milled with these settings until perforation is achieved. Once a hole is visible at the center of the sample, the gun angles are changed to 5° for gentle milling/cleaning of the sample with an incident ion energy of 2.5 KeV for 10 minutes.

3.3 Lorentz Transmission Electron Microscopy

Lorentz Transmission Electron Microscopy (LTEM) is a technique used to image and characterize magnetic domains and magnetic domain walls. The lenses in a TEM generate magnetic fields and the specimen sits right inside the objective lens (which has a magnetic field of ~ 1 - 2 Tesla). Hence, the objective lens is turned off in Lorentz mode to keep the magnetic specimen in a field-free/low-field condition. A separate lens called Lorentz lens (Lorentz pole-piece) located below the objective lens is used to image the specimen, albeit with a reduction in attainable magnification and resolution [69].

3.3.1 Classical approach to Lorentz microscopy

When an electron with charge e and velocity \mathbf{v} passes through a region of magnetic material with an electrostatic field \mathbf{E} and a magnetic field \mathbf{B} , it experiences a force known as Lorentz force (\mathbf{F}_L), given by equation below [70]:

$$\mathbf{F}_L = -e[\mathbf{E} + \mathbf{v} \times \mathbf{B}]. \quad (3.1)$$

There will be a deflection of the electron's trajectory since the magnetic component of the Lorentz force acts normal to the electron beam as shown in Fig. 3.2. The magnetic field \mathbf{B} can be divided into two components, a) the component normal to \mathbf{v} , and b) the component parallel to \mathbf{v} :

$$\mathbf{B} = \mathbf{B}_\perp + B_z \mathbf{n}. \quad (3.2)$$

Here, \mathbf{n} is the unit vector parallel to the electron beam direction. Only the in-plane magnetic induction (\mathbf{B}_\perp) will contribute to the deflection and the Lorentz deflection angle is expressed as:

$$\theta_L = \frac{e}{h} \lambda \mathbf{B}_\perp t = C_L(V) \mathbf{B}_\perp t, \quad (3.3)$$

where e is the charge of electron, h is Plank's constant, λ is the relativistic wavelength of the electron, and t is the thickness of the magnetic thin film. It is assumed that the sample has a constant thickness throughout and hence a constant electrostatic lattice potential. The constant $C_L(V)$ is determined by the acceleration voltage V of the microscope and is given by:

$$C_L(V) = \frac{9.37783}{\sqrt{V+0.97485 \times 10^{-3} V^2}} \mu\text{rad/T/nm}. \quad (3.4)$$

For a microscope voltage of 300 kV, $C_L(300) = 0.476050 \mu\text{rad T}^{-1} \text{ nm}^{-1}$. Assuming a 100 nm thick magnetic foil with an in-plane magnetic induction \mathbf{B}_\perp of 1 Tesla, we obtain a deflection angle of 47.6 μrad . Since the magnetic deflections are pretty small, the deflected electrons travel very close to the optic axis. It is important to note that the Lorentz deflection angle is 2-3 times smaller than the Bragg angle for electron diffraction, which is in the range of a few milliradians, hence we can easily differentiate between the magnetic deflection and crystal diffraction. Also

note that the deflection angle decreases with decreasing electron wavelength. In other words, higher microscope voltages give rise to smaller magnetic deflection angles.

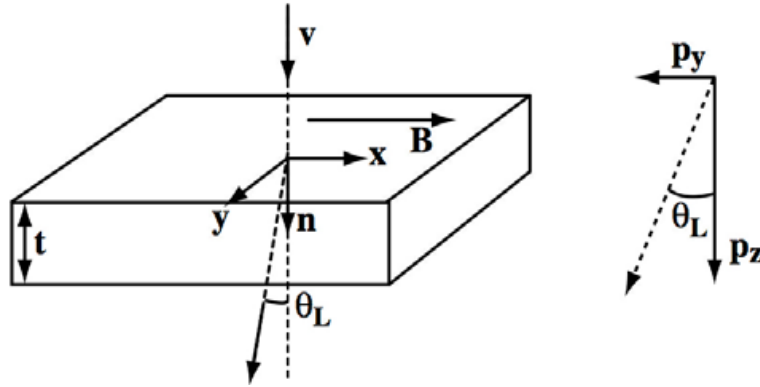


Figure 3.2: Schematic of a magnetic thin foil and the resulting deflection of an incident electron beam [70].

Since the deflection angle is directly dependent on the product $\mathbf{B}_{\perp}t$, Lorentz imaging will provide information about the magnetic induction of the sample. However, the information will at best be qualitative since it results from the combined effect of sample thickness and sample magnetization. Localized variation in thickness and magnetic induction produces identical changes in the Lorentz deflection angle. An independent thickness measurement is required for Lorentz methods to be used to create a direct map of the in-plane induction.

3.3.2 Lorentz Fresnel imaging

The Lorentz Fresnel Imaging mode is a defocus or out-of-focus mode of imaging magnetic domain walls - the boundaries between two differently oriented magnetic domains. This is the easiest imaging mode of all the Lorentz TEM based observation modes since only a change in lens current is required to image domain walls. In this mode, three images are taken namely

focus, under-focus, and over-focus images. Fig. 3.3 schematically shows the Fresnel imaging mode. Consider a sample with three magnetic domains whose magnetization directions are in and out of the plane of the drawing. The domains are separated from each other by 180° magnetic domain walls. A typical bright field image acquired using the transmitted beam does not show any magnetic contrast for an in-focus condition. In other words, when the imaging lens is focused at the sample, only crystal diffraction (and/or absorption) contrast is observed. A change in imaging lens current changes the focus of the sample. In order to capture Fresnel contrast, the Lorentz lens is operated in the defocused mode, the object plane is located at a distance Δf below (under-focus) or above (over-focus) the sample and the resulting image will show a bright feature (excess of electrons) or a dark feature (deficiency of electrons) at the position of domain walls. In the under-focus image, the bright wall is called the convergent wall since the electrons are deflected towards the wall while the dark wall is called the divergent wall because electrons are deflected away from this wall. Since the deflection angle of electrons is pretty small, a very high defocus value is required to observe the contrast, which degrades the resolution of the images. In addition, a slight change in magnification can be observed in the over-focus and under-focus images due to the change in lens current. When the lens goes from under-focus to over-focus mode, the contrast of walls is reversed. Fig. 3.4 shows a set of experimental Fresnel through-focus series images of a permalloy film. It can be seen that the in-focus image doesn't show any magnetic contrast. The bright and the dark contrast in the defocused images correspond to magnetic domain walls. The small bright and dark spots correspond to vortices (circular magnetization configuration) in the sample. The under-focus and over-focus images can be seen reversing the contrast at the domain walls.

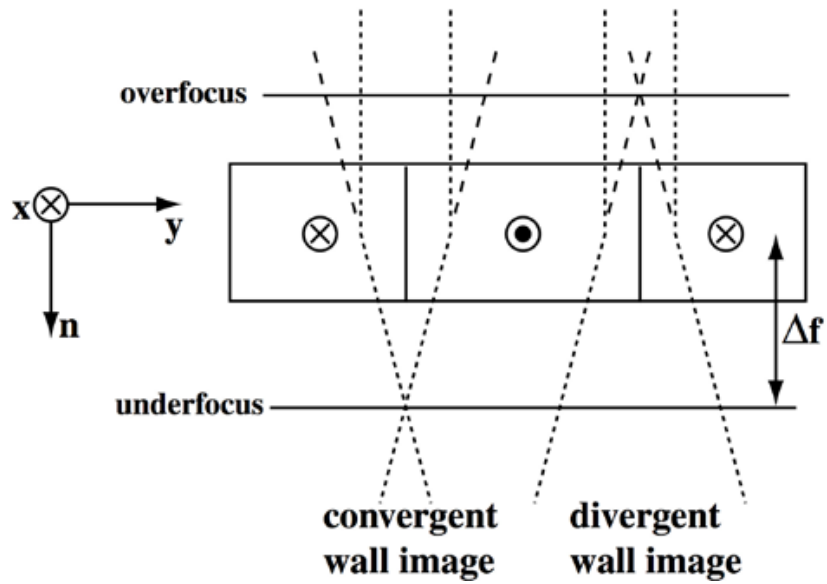


Figure 3.3: Schematic illustration of the Fresnel imaging mode [70].

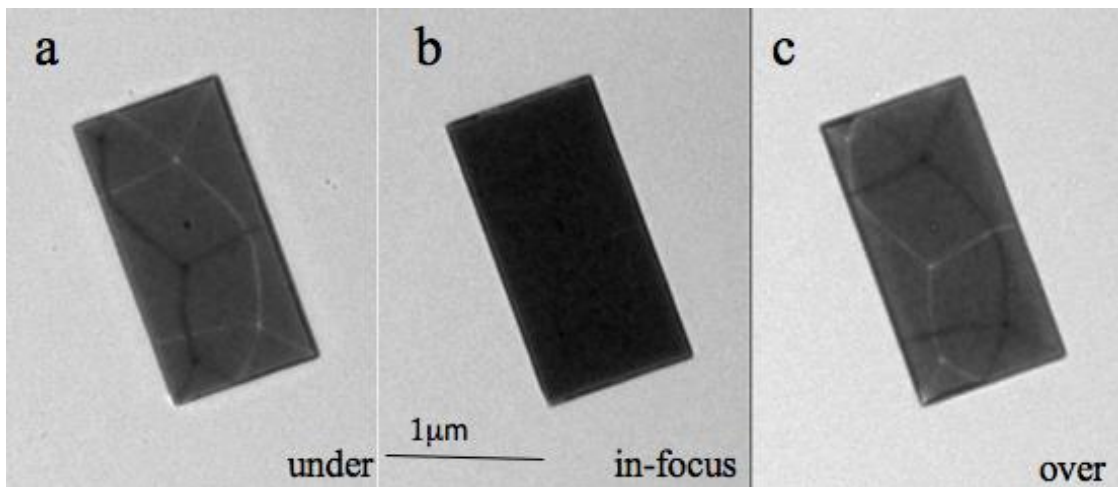


Figure 3.4: Lorentz Fresnel through-focus images of a thin permalloy island [71].

One of the drawbacks of Fresnel imaging is that it is operated in the defocused mode. This makes it difficult to obtain any quantitative information such as domain wall width, from Fresnel images. It can at best provide the position of domain walls. However, it is possible to extract quantitative information about the magnetic induction by reconstructing the phase of the electron

waves. This approach is described in Section 3.5.

3.3.3 Quantum mechanical approach to Lorentz microscopy

The quantum mechanical approach utilizes the wave nature of the electrons to understand the magnetic image theory in Lorentz TEM. The electron wave changes its phase as it interacts with a magnetic sample. In 1959, Aharonov and Bohm [72] gave a fundamental equation for the phase shift imparted to such an electron wave in the presence of an electromagnetic field. This phase shift, also called the A-B phase shift is given as a function of the electrostatic lattice potential V and the magnetic vector potential \mathbf{A} and is given by:

$$\phi(\mathbf{r}) = \frac{\pi}{\lambda E_t} \int_L V(\mathbf{r}, z) dz - \frac{e}{\hbar} \int_L \mathbf{A}(\mathbf{r}, z) \cdot d\mathbf{r}, \quad (3.5)$$

where E_t is the total energy of the electron beam and the integrals are carried out along a straight line L parallel to the incident electron beam direction. The first term in the phase shift is the electrostatic phase shift while the second term is the magnetic phase shift. An example of a magnetic phase shift for the domain arrangement in Fig. 3.3 is described below. The magnetic thin foil has a constant thickness t and a uniform in-plane magnetic induction \mathbf{B}_\perp . The magnetization direction is normal to the plane of the drawing. The center of the thin foil is taken to be the origin (0,0,0) of the right-handed Cartesian reference frame, with its z -axis coinciding with the optic axis. The electron travels along the positive z -direction. The magnetization in the three domains points along the x -direction, hence the resulting Lorentz deflection will be along the y -direction. Using Stokes' theorem [73], the magnetic phase shift for this thin foil can be expressed as:

$$\phi(y) = \frac{e}{\hbar} \int_{-t/2}^{+t/2} \int_0^y \mathbf{B}_\perp dy dz = \frac{e}{\hbar} \mathbf{B}_\perp ty. \quad (3.6)$$

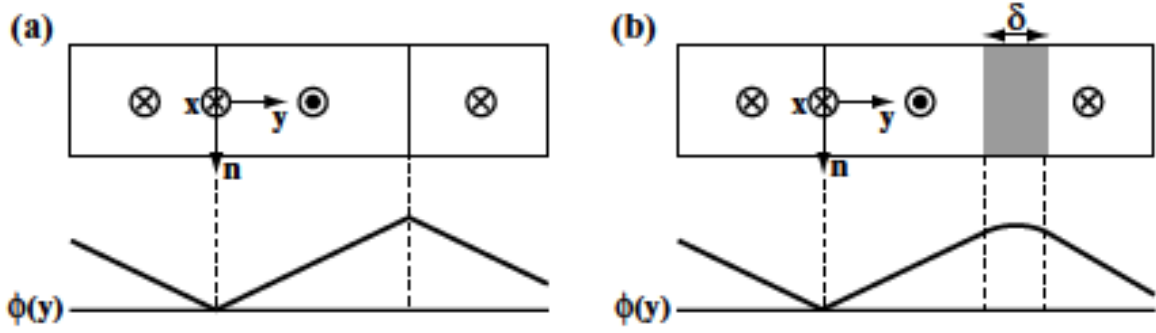


Figure 3.5: Schematic illustration of phase computation: a) Infinitely narrow domain wall, b) Finite domain wall width [2].

Using the above equation, the phase shift profile can be computed as shown in Fig. 3.5. Fig. 3.5(a) shows the phase shift for an infinitely narrow domain wall. In this case, the phase shift changes linearly inside the magnetic domains and the slope of the phase changes discontinuously across the domain walls. However, real domain walls usually have a finite domain wall width as shown in Fig. 3.5(b) and the resulting slope change is continuous across the walls and the range over which the slope changes (or the curvature) corresponds to the domain wall width δ . The phase shift is linear only if the sample has a constant thickness and a uniform magnetization. Local thickness variations and non-uniform magnetization will contribute non-linearity to the phase profile. The Lorentz deflection angle, equation (3.3), can be written in the form of the phase gradient as:

$$\nabla\phi = \frac{2\pi}{\lambda} \theta_L \mathbf{e} = \frac{e}{\hbar} \mathbf{B}_\perp t \mathbf{e} = -\frac{e}{\hbar} (\mathbf{B} \times \mathbf{n}) t. \quad (3.7)$$

It should be noted that the magnetic phase shift is independent of the electron energy. However, the electrostatic component of the phase shift decreases with increasing electron energy or the microscope voltage V . So, it would seem that it is better to use higher-voltage microscopes for magnetic imaging. But the electron deflection angle decreases with increasing electron energy. Hence it is advisable to use intermediate voltages in the range of 200-400 kV to achieve the best compromise between a strong relative magnetic contribution and reasonably large Lorentz deflection angles.

3.4 Lorentz Image Simulation

In this section, the approach to Lorentz image simulations is discussed. Two methods to compute the phase of an electron wave are presented, followed by simulation of Lorentz Fresnel images.

3.4.1 Computation of magnetic phase shift

In thin magnetic films, the magnetic phase shift imparted to the electron beam in the Lorentz TEM can be calculated by assuming that the magnetization has in-plane periodicity, i.e. periodicity in 2-D space. We can construct a lattice with a distribution of magnetization that satisfies periodic boundary conditions as well as smooth transition of magnetization at the boundaries. Once we have created a two-dimensional (2D) magnetization unit cell, we assign a three-dimensional (3D) magnetization vector $\mathbf{M}(i,j)$ or $\mathbf{M}(\mathbf{r})$ to each pixel (i,j) in the cell. $\mathbf{M}(i,j)$ has three components namely $M_x(i,j)$, $M_y(i,j)$ and $M_z(i,j)$. The magnetization is assumed to be constant along the thickness of the magnetic thin film and we also ignore the demagnetization field outside the film. As an example, one such magnetization configuration can be constructed by using the domain wall energetics solution described by Hubert and Schafer [49]. Consider an

infinite planar 180° Bloch wall, separating two opposite domains as shown in Fig. 3.6. The wall is perpendicular with respect to the x -axis and the magnetization angle (φ) is the angle between the magnetization vector and the x -axis. φ' is the derivative of φ with respect to x . A is the exchange energy constant. We can neglect the second anisotropy constant and denote by K the first constant then the specific wall energy γ_w - the total energy per unit area of the wall - is an integral over the expressions,

$$\gamma_w = \int_{-\infty}^{\infty} [A\varphi'^2 + K\cos^2\varphi]dx, \varphi(-\infty) = \frac{\pi}{2}, \varphi(\infty) = -\frac{\pi}{2}. \quad (3.8)$$

The domain wall width is given by the slope of the magnetization angle φ and its value is $\delta = \pi\sqrt{A/K}$. By solving this equation for minimization of energy, a relationship between φ and x is established,

$$\sin\varphi = \tanh\xi; \xi = x/\sqrt{A/K}. \quad (3.9)$$

The wall with the opposite rotation sense is described by $-\sin\varphi = \tanh\xi$. Alternate forms of this relation are $\cos\varphi = 1/\cosh\xi$ and $\tan\varphi = \sinh\xi$.

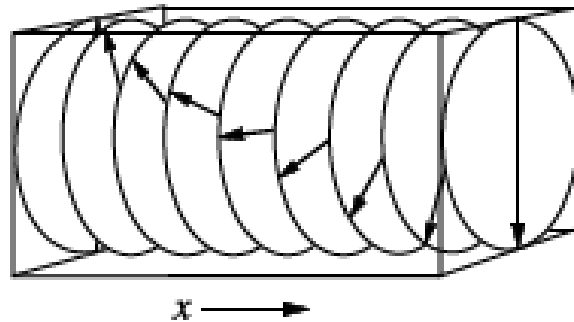


Figure 3.6: Schematic figure showing rotation of magnetization vector from one domain through a 180° Bloch wall, to the other domain in an infinite uniaxial material [49].

Assuming a saturation magnetization (M_s) of 1 A/m and a domain wall width $\delta_{180^\circ} = 50.24$ nm, \mathbf{M} as a function of x can be written as,

$$\mathbf{M}(x) = M_s \sin \varphi = M_s \tanh \zeta. \quad (3.10)$$

Two domain walls of opposite sense can be created as shown in Fig. 3.7 (a). This magnetization configuration is periodic in x -direction. The magnetization cell is defined for an array of $P \times Q = 256 \times 256$ pixels, and the pixel size is equal to $D = 2$ nm. This configuration commonly occurs in materials, which have their easy axes along in-plane directions, i.e., magnetization vectors prefer to lie along these directions because it reduces the total magnetic energy. The incident electron beam is normal to the plane of the drawing along the [00-1] direction. The table below gives the numerical values of various parameters used in this calculation. From here onwards, we'll be using the same numerical values for all the simulations unless otherwise specified.

Table 3-1: Microscope and material parameters used for simulation.

Microscope voltage	200 kV
Relativistic wavelength of electron (200 kV)	0.002508 nm
Saturation magnetic induction (B_s)	1 Tesla
Thickness of sample (t)	100 nm
Electron charge (e)	1.602e-19 Coulombs

For a sample with magnetization $\mathbf{M}(\mathbf{r})$, the magnetic vector potential is given by:

$$\mathbf{A}(\mathbf{r}) = \frac{\mu_0}{4\pi} \int \mathbf{M}(\mathbf{r}') \times \frac{\mathbf{r}-\mathbf{r}'}{|\mathbf{r}-\mathbf{r}'|^3} d^3\mathbf{r}'. \quad (3.11)$$

The magnetic phase shift can be computed using the A-B equation as,

$$\phi_m(\mathbf{r}) = \frac{e}{\hbar} \int_L \mathbf{A}(\mathbf{r}, z) \cdot d\mathbf{r}. \quad (3.12)$$

For such magnetic configurations, two approaches can be used to calculate the phase shift using the A-B equation. One approach is to calculate the phase shift numerically as shown by Mansuripur [74], and the second approach [75] is to calculate the phase shift analytically. Both approaches are described below.

It has been shown by Mansuripur and further explained by De Graef [2] that the magnetic A-B phase shift can be calculated using Fast Fourier Transforms for such a periodic magnetization configuration in thin magnetic films. A full explanation can be found in the Mansuripur paper [74]. In the equation below, \mathbf{M}_{mn} represents the discrete Fourier components of the magnetization over a unit cell of $P \times Q$ pixels with a pixel spacing D , with $m = 1, \dots, P$ and $n = 1, \dots, Q$,

$$\mathbf{M}_{mn} = \sum_i^P \sum_j^Q \mathbf{M}(i, j) \exp \left[-2\pi i \left(\frac{mi}{P} + \frac{nj}{Q} \right) \right]. \quad (3.13)$$

The A–B phase shift is then given by the discrete 2D Fourier transform:

$$\phi(\mathbf{r}) = \frac{2e}{\hbar} \sum_{m=0}^P \sum_{n=0}^Q i \frac{t}{|\mathbf{q}|} G_{\mathbf{p}}(t|\mathbf{q}|) (\hat{\mathbf{q}} \times \mathbf{e}_z) \cdot [\mathbf{p} \times (\mathbf{p} \times \mathbf{M}_{mn})] e^{2\pi i \mathbf{r} \cdot \mathbf{q}}. \quad (3.14)$$

Note that the term $(m, n) = (0, 0)$ does not contribute to the summation; $\mathbf{q} = \frac{m}{P} \mathbf{e}_x^* + \frac{n}{Q} \mathbf{e}_y^*$ is the two dimensional frequency vector; $\mathbf{e}_x, \mathbf{e}_y, \mathbf{e}_z$ are lattice unit vectors in real space; $\mathbf{e}_x^*, \mathbf{e}_y^*$ are the reciprocal unit vectors, unit vector \mathbf{p} denotes the electron beam direction expressed in the orthonormal reference frame, p_z is given by $\mathbf{p} \cdot \mathbf{e}_z$ and the function $G_{\mathbf{p}}(t|\mathbf{q}|)$ is given by:

$$G_{\mathbf{p}}(t|\mathbf{q}|) = \frac{1}{(\mathbf{p}\cdot\hat{\mathbf{q}})^2 + p_z^2} \text{sinc}\left(\pi t|\mathbf{q}|\frac{\mathbf{p}\cdot\hat{\mathbf{q}}}{p_z}\right), \quad (3.15)$$

where $\text{sinc}(x) = \sin(x)/x$. Note that the above phase shift equation makes it clear that the projection of $\mathbf{M}(i,j)$ along the electron beam direction \mathbf{p} makes no contribution to the phase shift. In other words, no magnetic contrast is observed in the Lorentz TEM if the electron beam is parallel to the magnetization direction or only in-plane component of magnetization with respect to the electron beam gives rise to magnetic contrast. For normal beam incidence ($\mathbf{p} \parallel \mathbf{e}_z$), the function $G_{\mathbf{p}}(t|\mathbf{q}|)$ takes on the value 1. Accommodating $G_{\mathbf{p}}$ into the phase shift equation enables the computation of the phase shift at different relative beam-sample orientations. Usually, in a TEM, the sample is tilted to orient the sample in a desired direction since tilting the beam inside the TEM disrupts the electron optical properties. Additionally, there is limit on beam tilting inside TEM. However, a clockwise sample tilt is equivalent to an anti-clockwise beam tilt, hence the phase shift can be simulated at different beam tilts for comparison with experimental images. Fig. 3.7(b) shows the phase map ($B_{st} = 100$) obtained for the magnetic configuration in Fig. 3.7(a). A sharp bright and dark contrast can be seen at the position of domain walls. The intensity is increasing/decreasing away from the walls. The intensity varies from -55.75 rad to +55.75 rad in the phase map. Fig. 3(c) shows a shaded surface representation of phase shift. It clearly shows that the magnetic phase shift inside a domain is a linear (planar) function of position, whereas the slope of the phase changes upon crossing a magnetic domain wall. The phase shift can be as large as several radians hence a magnetic thin foil is a strong phase object.

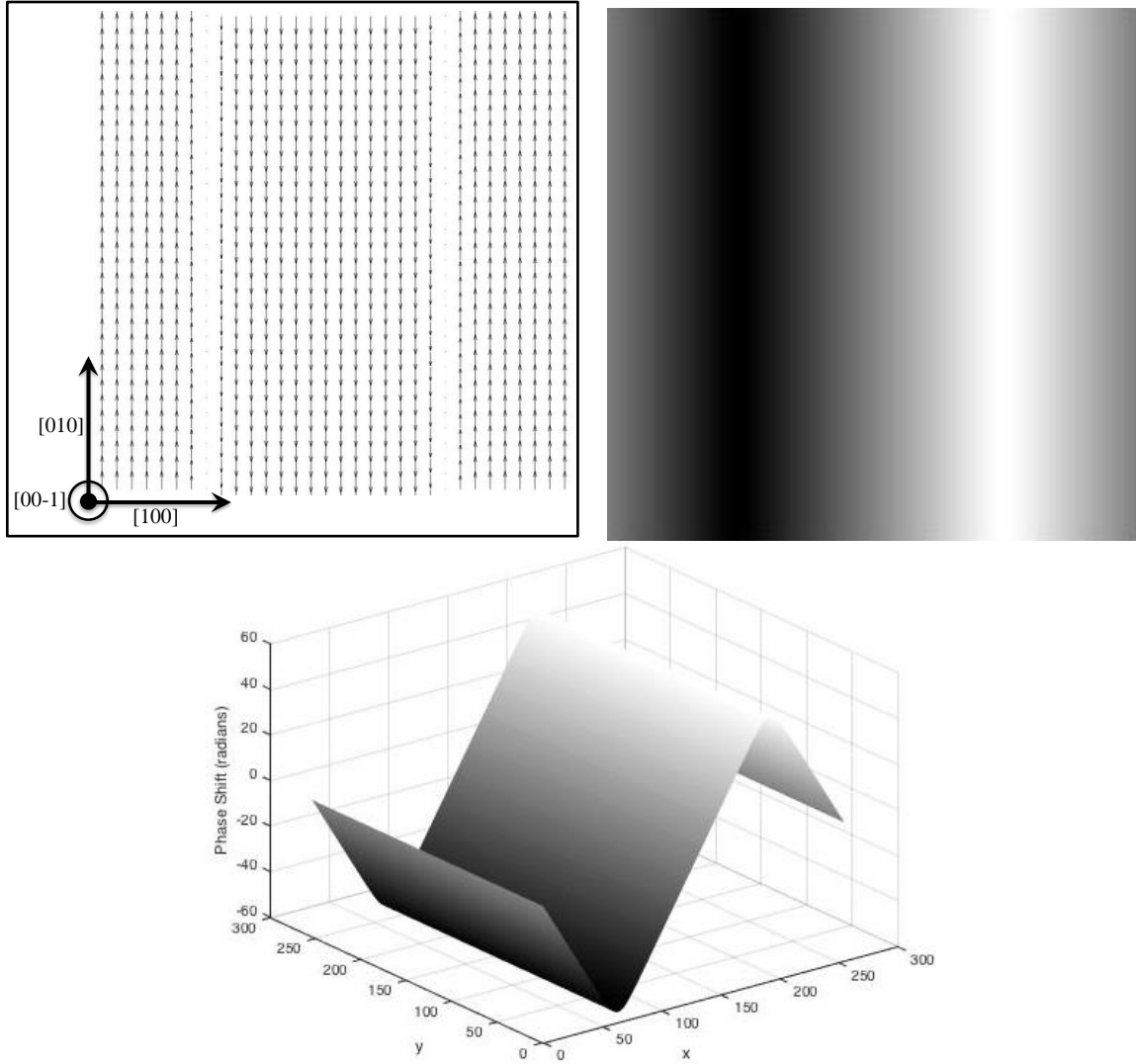


Figure 3.7: (a) Periodic 2D magnetization configuration with two different domain orientations; magnetization vectors are along [010] and [0-10] directions; domain walls have a width of 50.24 nm, (b) The calculated A-B phase shift for the configuration in (a), (c) Shaded surface representation of the phase shift.

The analytical approach to solving the phase shift equation is described below [75]. Consider an array of uniformly magnetized nanoparticles with the magnetization vector as $M_s \hat{\mathbf{m}}$; $\hat{\mathbf{m}}$ is the unit vector for the direction of magnetization. A dimensionless shape function $D(\mathbf{r})$ is introduced to represent region bounded by the particle surface. $D(\mathbf{r})$ is 1 inside the particle and 0 outside the particle.

$$\mathbf{M}(\mathbf{r}) = M_s \hat{\mathbf{m}} D(\mathbf{r}). \quad (3.16)$$

$\mathbf{M}(\mathbf{k})$ in the reciprocal space can be obtained by taking the Fourier transform of the above equation and using this, the magnetic vector potential in 3D Fourier space is given as:

$$\mathbf{A}(\mathbf{k}) = -\frac{iB_s}{k^2} D(\mathbf{k}) (\hat{\mathbf{m}} \times \mathbf{k}). \quad (3.17)$$

B_s is the magnetic induction corresponding to the saturation magnetization M_s . This equation takes into account the demagnetizing field extending in the vacuum surrounding the particle. This field depends on the geometry of the uniformly magnetized particles. Using the A-B phase shift equation, the magnetic phase shift can be computed as:

$$\phi_m(\mathbf{k}) = \frac{i\pi B_s}{\phi_0} \frac{D(k_x, k_y, 0)}{k_\perp^2} (\hat{\mathbf{m}} \times \mathbf{k})|_z, \quad (3.18)$$

where $k_\perp = (k_x^2 + k_y^2)^{1/2}$.

The phase shift in real space is then simply given as the inverse Fourier transform of Equation 3.18.

3.4.2 Simulation of magnetic induction maps

The phase shift can be related to the in-plane integrated magnetic induction using the equation below [76]:

$$(B_x, B_y) = \frac{\phi_0}{\pi t} \left(-\frac{\partial \phi}{\partial y}, \frac{\partial \phi}{\partial x} \right). \quad (3.19)$$

Once the phase shift profile for a given magnetization configuration is known, the in-plane magnetic induction maps (B_x and B_y) can be created. These induction maps can then be used to

generate color induction maps that give the direction of the integrated magnetic induction inside differently oriented magnetic domains.

3.4.3 Lorentz image simulations

In Section 3.3.3, it is shown that the phase shift caused by a magnetic specimen can amount to several radians. Hence, a magnetic thin foil can be considered as a strong phase object since it changes the phase of the electron wave without altering its amplitude. Following this, Lorentz Fresnel images can be simulated using a method similar to image simulations of phase contrast microscopy, as described in [2]. Fig. 3.8 shows the progression of the electron wave as it travels down the microscope column.

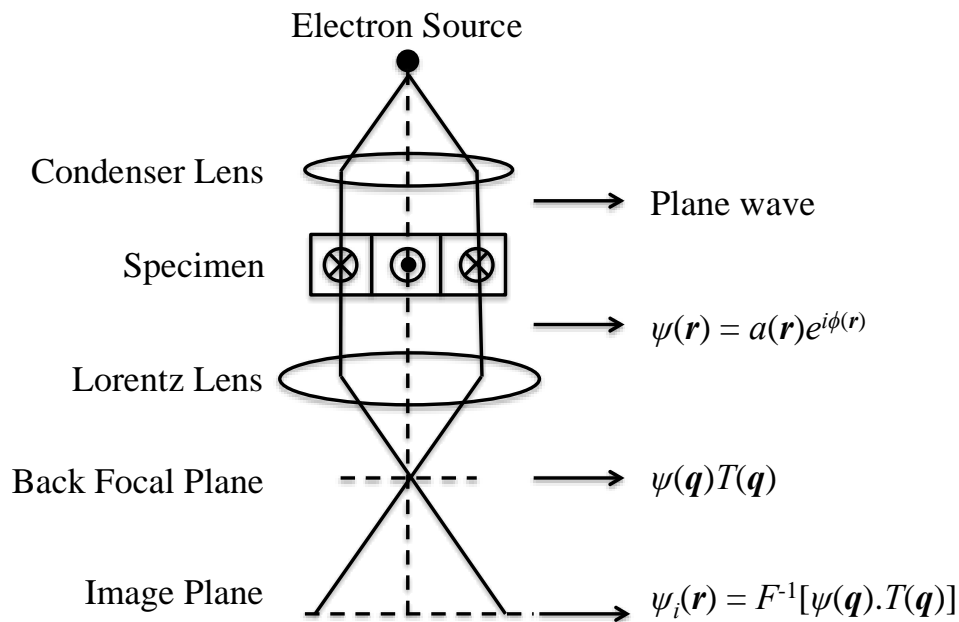


Figure 3.8: Schematic illustration of image formation in Lorentz TEM.

In the TEM, when a coherent electron beam passes through a magnetic specimen, the exit wave

function can be written as,

$$\psi(\mathbf{r}) = a(\mathbf{r})e^{i\phi(\mathbf{r})}, \quad (3.20)$$

here, $a(\mathbf{r})$ is the amplitude of the electron wave, $\phi(\mathbf{r})$ is the phase shift imparted to the electron wave. When the beam passes through the imaging lens (Lorentz lens), this wave function is modified and this modification can be accommodated by using the point spread function $T(\mathbf{r})$ of the imaging lens. Thus, assuming linear image formation, the image plane wave function can be computed by taking the convolution product of the exit wave function with the point spread function $T(\mathbf{r})$. The paraxial wave function $\psi(\mathbf{q})$ in the back focal plane can be computed by taking the Fourier transform of exit wave function, where \mathbf{q} is a vector in the lens back focal plane. And the image plane wave function can also be obtained by taking the inverse Fourier transform of the product $\psi(\mathbf{q})$ and $T(\mathbf{q})$; $T(\mathbf{q})$ is the microscope phase transfer function,

$$\psi_i(\mathbf{r}) = \psi(\mathbf{r}) \otimes T(\mathbf{r}) = \mathcal{F}^{-1}[\psi(\mathbf{q}) \cdot T(\mathbf{q})]. \quad (3.21)$$

The Lorentz deflection angle is of the order of few μrad , giving rise to short spatial frequency vectors \mathbf{q} hence we can safely ignore higher order terms in the phase transfer function. And, the microscope contrast transfer function for Lorentz imaging can be approximately written as,

$$T_L(\mathbf{q}) = A(\mathbf{q} - \mathbf{q}_0)e^{z_2q^2} e^{z_4q^4}, \quad (3.22)$$

$$z_2 = -(\pi\theta_c\Delta f)^2 + i\pi\lambda[\Delta f + C_a\cos 2(\phi - \phi_a)], \quad (3.23)$$

$$z_4 = -\frac{(\pi\lambda\Delta)^2}{2} + 2(\pi\theta_c\lambda)^2\Delta f C_s - i\frac{\pi}{2}C_s\lambda^3. \quad (3.24)$$

$A(\mathbf{q}-\mathbf{q}_0)$ is the aperture function, θ_c is the beam divergence angle, Δ is the defocus spread, C_s and

C_a are constants of the spherical aberration and astigmatism, respectively. In addition, if the aperture radius is small enough to exclude Bragg reflections, we can ignore the diffraction aperture function $A(\mathbf{q}-\mathbf{q}_0)$ in the contrast transfer function $T_L(\mathbf{q})$ for Lorentz image simulations. Even though the spherical aberration constant (C_s) of a dedicated Lorentz pole piece is as high as several meters, the phase shift caused by spherical aberration can be ignored since the short spatial frequency vectors result in a small contribution to the phase shift. Hence, the final two parameters in z_4 become zero, which effectively makes it a real number. The first term of z_4 becomes the damping envelope for an in-focus image ($\Delta f = 0$) hence it cannot be ignored. The defocus spread is very large for Lorentz imaging when a dedicated Lorentz pole piece is used. Similarly, the chromatic aberration constant is in the range of meters. So, these must be taken into account for all the Lorentz image simulations. Once the exit wave function and contrast transfer function are obtained, we can calculate the image intensity by taking the square modulus of the image plane wave function,

$$I(\mathbf{r}) = |\psi_i(\mathbf{r})|^2 = |\mathcal{F}^{-1}[\psi(\mathbf{q}) \cdot T(\mathbf{q})]|^2. \quad (3.25)$$

Solving this equation, we obtain,

$$I = a^2 - \frac{\lambda \Delta f}{2\pi} \nabla \cdot (a^2 \nabla \phi) + \frac{(\theta_c \Delta f)^2}{2} [a \nabla^2 a - a^2 (\nabla \phi)^2]. \quad (3.26)$$

For a uniform background intensity $a^2 = 1$, therefore,

$$I = 1 - \frac{\lambda \Delta f}{2\pi} \nabla^2 \phi - \frac{(\theta_c \Delta f)^2}{2} (\nabla \phi)^2. \quad (3.27)$$

This equation can be further simplified if we ignore the last term in the intensity equation by assuming that the beam divergence angle θ_c is very small (negligible) for a coherent beam,

$$I(\mathbf{r}, \Delta f) = 1 - \frac{\lambda \Delta f}{2\pi} \nabla^2 \phi. \quad (3.28)$$

For a $\Delta f = 0$, which is an in-focus image, the expression for intensity gives a value of 1. The contrast in a Fresnel image appears only when the value of defocus and Laplacian of the phase shift have non-zero values. And the Laplacian of phase shift is nonzero at the position of domain walls. This means that the in-focus image will not have any magnetic contrast. The above equation explains the origin of magnetic contrast in Lorentz Fresnel images.

3.5 Phase Reconstruction Theory

As described previously, Fresnel images only provide information about the position of domain walls. The information is qualitative in nature in that we can say that the magnetization direction is opposite on either sides of a domain wall. However, the exact magnetization orientation of the magnetic domains cannot be deduced from Fresnel images. In order to extract quantitative information about the domains, we must reconstruct the magnetic phase shift from the intensities in the Fresnel images to derive the induction configuration inside the sample. The transport-of-intensity equation (TIE) is used to reconstruct the phase from the intensities in the images. Paganin and Nugent showed that the longitudinal derivative of the intensity can be related to the in-plane spatial variations of the magnetic induction [77]. This relation is mathematically expressed using TIE as follows:

$$\nabla \cdot (I(\mathbf{r}, 0) \nabla \phi) = -\frac{2\pi}{\lambda} \frac{\partial I(\mathbf{r}, 0)}{\partial z} \approx -\frac{2\pi}{\lambda} \frac{I(\mathbf{r}, \Delta f) - I(\mathbf{r}, -\Delta f)}{2\Delta f}, \quad (3.29)$$

where $I(\mathbf{r}, \Delta f)$ is the image intensity at microscope defocus Δf , and ∇ is the 2-D Nabla differential operator in the plane normal to the beam direction z . The phase shift suffered by an

electron as it travels through the specimen can be inferred from a through-focus series of Fresnel images. The reconstructed phase can be used to obtain quantitative information about the sample, such as the magnetization configuration and the width of a magnetic domain wall. The Fourier transform method is used to derive a solution for the TIE equations. The gradient of the phase can be expressed in terms of the in-plane components of the magnetic induction as follows:

$$\nabla\phi = \frac{e}{\hbar} \mathbf{B}_{\perp} t \mathbf{e}. \quad (3.30)$$

The color map obtained from the phase reconstruction provides information about the direction of the integrated magnetic induction inside the sample.

The phase reconstruction of Lorentz Fresnel images is performed using the Interactive Data Language (IDL) routines written by De Graef and Tandon [71] in the following steps. Firstly, a series of in-focus, under-focus and over-focus Fresnel images, with the same defocus $|\Delta f|$, are obtained in the Lorentz TEM as shown in Fig. 3.4. The input to the IDL routines are Fresnel series of images, defocus value and electron voltage. The routine aligns the through-focus images and computes the intensity difference at each pixel in the image by subtracting under-focus image from the over-focus image. Thereafter, Equation 3.29 is solved using FFT to obtain the final phase map shown in Fig. 3.9(a). The magnetic induction can then be computed by using Equation 3.30 assuming very small fringing fields and a uniform thickness. While this method is easy to use and requires no additional equipment, the reconstructed phase results in a magnetic induction integrated over the thickness of the foil.

Fig. 3.9 shows an example of a phase reconstruction for Fresnel images in Fig. 3. 4. In the phase map, domain walls correspond to regions where the phase map has curvature, i.e., ridges and valleys. Fig. 3.9(b) and Fig. 3.9(c) shows the integrated magnetic induction components (B_{xt} and B_{yt}). White corresponds to a large induction component along the positive x -direction (from left to right), or the positive y -direction (from bottom to top); dark regions correspond to induction components in the negative x and y -directions. The two inductions maps can be used to generate the color map as shown in Fig. 3.9(d). The color map of the integrated induction shows that the domain walls enclose magnetic domain regions whose magnetization points towards the top (blue color on the color wheel) and towards the bottom (yellow color on the color wheel) respectively. The horizontal magnetization directions are represented by red and green color. Intermediate colors correspond to induction directions containing both horizontal and vertical components.

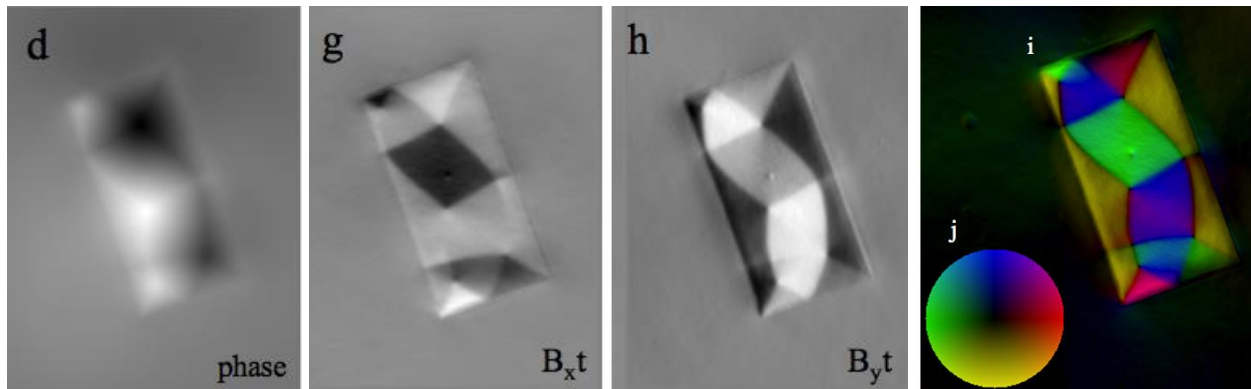


Figure 3.9: Reconstructed phase map, Induction maps: B_{xt} and B_{yt} , Color map [71].

It should be noted that the uncertainties in the microscope parameters needs to be taken into account for further quantitative analysis from the reconstructed phase map. A very large defocus Δf can cause a change of image magnification, image shift and rotation and the background

intensities of under-focus and over-focus images are not the same, and hence TIE is not valid under such conditions.

3.6 Spherical Aberration Corrected Lorentz Microscopy

The resolution of a TEM depends on a number of factors including the accelerating voltage, the properties of the electron source and the presence of lens aberrations. With the development of better electron sources because of advances in Field Emission Gun technology, the major factor limiting resolution is lens aberrations hence the actual resolution of a TEM is much lower than the theoretical resolution limit. Lens aberrations exist because it is not possible to create perfect magnetic lenses. Among all the lens aberrations, spherical aberration is the dominant factor in determining the resolution of the microscope. The effect of spherical aberration on image formation can be explained using Fig. 3.10 [2]. The electrons leaving an axial point object are affected by the spherical aberration of the magnetic lens. The electron beams passing through the outer zone of the lens (i.e., through a circle with a large radius r_a) are focused more strongly as compared to the electrons that are travelling close to the optic axis. As a result, a point object is imaged as a disk at the Gaussian image plane. The radius of the disk is given by:

$$r_i = MC_s\alpha^3, \quad (3.31)$$

where M is magnification factor, C_s is the coefficient of spherical aberration. The spherical aberration coefficient C_s is expressed in millimeters. It is important to note that C_s is very sensitive to variations in the magnetic field. In addition, spherical aberration cannot be completely removed because it is an inherent property of round magnetic lenses. However, spherical aberration can be corrected using a set of magnetic multipoles (deflectors) that produce

a negative spherical aberration, to compensate for the positive spherical aberration created by round lenses [78], [79]. Two types of correctors can be used to correct spherical aberration - Quadrupole-Octupole Corrector, Hexapole Corrector.

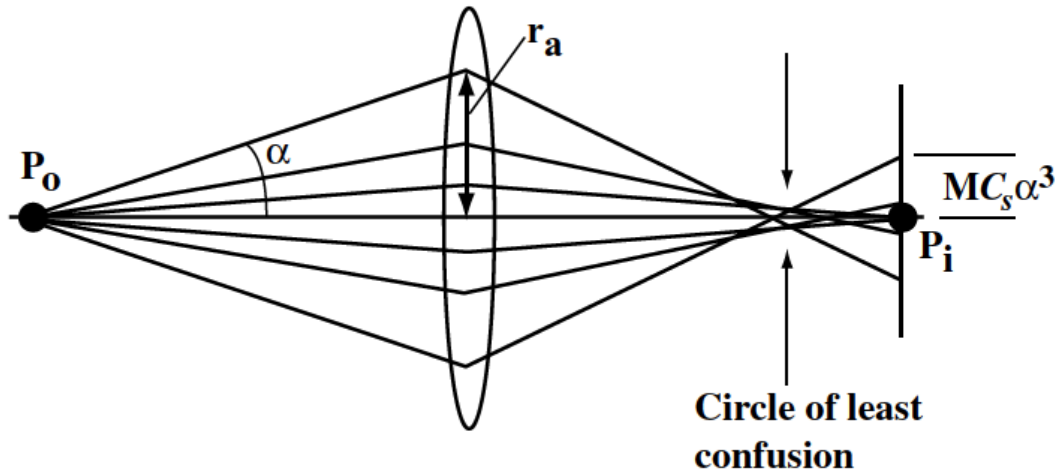


Figure 3.10: Schematic showing spherical aberration of electron beams [2].

Spherical aberration correction in Lorentz mode is essential for studying complex and nano-scale magnetic features. The field-free requirement in the Lorentz mode severely reduces the attainable magnification and resolution for magnetic imaging. In addition, the spherical aberration for a Lorentz pole piece is relatively high because of the low strength of the Lorentz lens. This makes it challenging to study nano-scale magnetic structures. The conventional Lorentz TEM offers a spatial resolution of $\sim 10\text{-}15$ nm and requires a very high defocus value (of the order of several microns) to make magnetic domain walls visible, which further degrades the resolution of the final images. In addition, inelastic scattering in the sample contributes noise to the images, which further limits the attainable resolution in the Lorentz mode. As described in previous sections, the reconstruction of the integrated magnetic induction relies on the recovered magnetic phase shift from Lorentz images. The electron phase shift is modified by the lens

aberrations; hence, it should be clear that lens aberrations need to be minimized to minimize the error in the recovered phase shift. In addition, aberration correction also reduces the defocus value required to image the domain walls and makes Fresnel images useful for quantitative analysis. Thus, a quantitative study of the magnetization necessitates the use of a C_s corrector in Lorentz mode. In this study, an FEI Titan 80-300 microscope with a dedicated Lorentz pole piece is used to study nano-scale magnetic structures. This microscope offers C_s -corrected field free imaging (<2 Oe) with <1 nm resolution. A comparison of the two microscopes used in this study is shown below:

Table 3-2: Microscope parameters [80].

TEM	Voltage (kV)	C_s (mm)	Resolution limit (nm)
FEI Tecnai F20	200	7430	10-12
FEI Titan 80-300	300	10	1-2

4 Magnetic Domain Structure of Co₄₀Pt₆₀ Alloy

4.1 Introduction

In this chapter, the magnetic domain structure investigations of near-eutectoid Co₄₀Pt₆₀ ordered alloys are presented. Lorentz Fresnel mode imaging in combination with phase reconstruction is utilized to quantitatively characterize the magnetic domain structure of two Co₄₀Pt₆₀ alloys subjected to different annealing conditions. Conventional bright field/dark field imaging and electron diffraction pattern analysis is also performed to relate the magnetic domain structure with the underlying crystallographic microstructure, including crystal/sample surface orientation and crystal defects.

The characteristics of the magnetic domain structure and crystallographic microstructure are correlated with the heat treatments and the observed bulk magnetic properties (for example magnetic coercivity). Magnetic domain walls in nano-chessboard regions are studied both experimentally and theoretically, and the comparative results are reported. Several other crystallographic defects such as tweed, coarse L1₀ plates, and anti-phase boundaries (APBs) are also characterized in the conventional TEM mode. The thickness/width of magnetic domain walls is measured using the reconstructed phase shift from experimentally obtained Lorentz images. The thickness results for domain walls in various magnetic domain structures are presented and compared with the theory.

4.2 Conventional TEM Imaging

Material fabrication and sample processing were carried out as follows by Priya Ghatwai [12] and Eric Vetter [14] at the University of Virginia. Binary Co-Pt alloys were synthesized by electric arc melting high purity Co (99.9%) and Pt (99.99%) in an argon atmosphere. The composition of bulk sample was determined to be $\text{Co}_{40.2}\text{Pt}_{59.8}$ with a grain size of approximately 20-40 μm [14]. The bulk samples were homogenized/recrystallized at 925°C for 8 hours in a tube furnace and then water quenched to retain the chemically disordered FCC A1 phase. The chemically disordered FCC phase is referred to as the base material. Thereafter, the eutectoid transformation $\text{A1} \rightarrow \text{L1}_0 + \text{L1}_2$ was facilitated as follows. Samples prepared from the base material were firstly heated to 750°C and then slow cooled from 750°C to 600°C at two different cooling rates. Finally, the samples were isothermally annealed at 600°C for either 1 week or 4 days. Thereafter, TEM thin specimens were prepared by mechanical grinding and dimpling followed by ion milling the samples to electron transparency [12], [14], [58]. Processing conditions for the alloys used in this study are summarized in the table below.

Table 4-1: Summary of specimens used for this work.

Composition	Specimen ID	Cooling rate	Annealing duration at 600°C
$\text{Co}_{40.2}\text{Pt}_{59.8}$	S-40	40°C/day	1 week
$\text{Co}_{40.2}\text{Pt}_{59.8}$	S-80	80°C/day	4 days

A detailed TEM microstructural study of alloys of similar composition has been performed by many researchers [11], [12], [14]. Hence, the microstructural characteristics of this alloy are well understood. A more recent study focused on evaluating macro magnetic properties such as

coercivity, remanence, and saturation magnetization using Vibrating Sample Magnetometer (VSM) [58]. There has been no attempt to-date, however, to explore the magnetic domain structure of near-eutectoid Co-Pt alloys. The characterization of magnetic domain structure is necessary in order to understand the underlying magnetic properties. In addition, the width of magnetic defects or magnetic domain walls is a critical parameter in controlling the magnetic properties, hence a reliable method is needed to measure the domain wall widths experimentally. Here, we have employed Lorentz TEM, conventional TEM, and image simulations based on micro-magnetic models to quantitatively characterize the magnetic domain walls associated with various types of crystallographic microstructures observed in this alloy.

The TEM microstructural study shows that both Specimen S-40 and Specimen S-80 primarily consist of colonies of nano-chessboard microstructures of varying length-scales, with a typical colony size of ~100-500nm. Specimen S-80 is found to exhibit finer-scale nano-chessboards as compared to Specimen S-40. It should be mentioned at this point that the nano chessboard structure is not a true equilibrium structure but is metastable and as a result, slight variations or non-uniformities in either the composition or temperature across the sample can result in differences in microstructure across the sample. This in turn will result in different magnetic domain structures as well. Depending on the ageing/annealing condition or the degree of atomic ordering, one or more than one type of the following microstructures are expected in a specimen:

1. Nano-chessboard microstructure ($L1_0+L1_2$)
2. Untransformed region (FCC disordered phase)
3. Partially transformed region or tweed structure ($L1_0$ variants in a disordered matrix)
4. Poly-twinned/macro-twinned plates of $L1_0$ variants

5. Coarsened $L1_0$ plates

6. Anti-phase boundaries (Disordered boundaries separating ordered domains)

The nano-chessboard structure, coarsened $L1_0$ plates, tweed structure, and anti-phase boundaries can be characterized by employing dark field imaging mode in TEM. However, it is typically not possible to detect the untransformed parent FCC phase. In this chapter, we will show the magnetic domain structures corresponding to the above-mentioned crystallographic microstructures and their inter-relationships. We will also compare them with the observed bulk magnetic properties.

In practice, Lorentz imaging is usually carried out first before doing conventional TEM imaging to ensure that the sample does not get exposed to the high magnetic field of objective lens, thereby avoiding the saturation of sample and the potential risk of modifying the magnetic domain structure of the sample. However, in this document, firstly we show conventional TEM images in order to understand the basic crystallography of the microstructures observed in Co-Pt alloy. This section forms the basis for a reliable interpretation of the magnetic domain structures shown in the subsequent sections.

The images in this section were acquired in the conventional TEM mode (with objective lens switched on) using an FEI Tecnai F20 microscope, operated at an electron accelerating voltage of 200 kV. Fig. 4.1 shows conventional TEM images of the nano-chessboard structure from a location in Specimen S-80. As described earlier in Chapter 2, the nano-chessboard structure consists of chessboard colonies that are formed along all the three crystallographic axes of the parent cubic grain. When a grain is aligned along one of the crystallographic axes inside TEM

and imaged under the proper diffraction/beam conditions, a perfect nano-chessboard structure is observed. The chessboard colonies along the other two crystallographic axes are seen as parallel rods under this imaging condition. Fig. 4.1(b) shows one such (110) Dark Field (DF) TEM image with a perfect nano-chessboard structure containing L_{12} phase and two orientation variants of L_{10} phase. The Bright Field (BF) image (Fig. 4.1(a)) of this region also hints towards the presence of nano-chessboard structure. More specifically, the inter-phase boundaries between the L_{10} and L_{12} phases can be seen as grey-colored contrast in the BF image. All the directions and planes in TEM images (real space) and diffraction patterns (reciprocal space) in this document are indexed with respect to the parent cubic lattice. The crystal is oriented along the [001] zone axis; Fig. 4.1(c) shows the [001] Zone Axis Diffraction Pattern (ZADP) acquired in this region. In this ZADP, the blue circle indicates a fundamental reflection, the yellow circle indicates (110) superlattice reflection, the red circle indicates (010) superlattice reflection, and the green circle indicates (100) superlattice reflection. The white 'X' indicates the transmitted beam or (000) which has been blocked by the beam blocker. A DF TEM image acquired with a (110) type superlattice reflection renders X- and Y-variants of L_{10} phase dark while the L_{12} phase lights up hence it looks like a typical nano-chessboard pattern. As can be seen in the DF image, two orientation variants of L_{10} phase are alternating in [110] and [1-10] directions. The L_{10} tiles are typically observed to be diamond or parallelogram shaped, while L_{12} tiles are primarily square-shaped. This is consistent with the earlier reported results [11], [81]. The long axes of diamond-shaped L_{10} orientation variants lie along either [100] or [010] axis in agreement with their respective tetragonal directions. In Fig. 4.1(a) and (b), the solid white arrows are pointing to parallel rods corresponding to nano-chessboard colony along the [010] crystallographic axis. Since the sample is oriented along [001] zone axis, the rods along [010] direction get projected

as dark/bright contrast in both the BF and DF images. These parallel rods contain two orientation variants of $L1_0$ phase (Y+Z) and $L1_2$ phase.

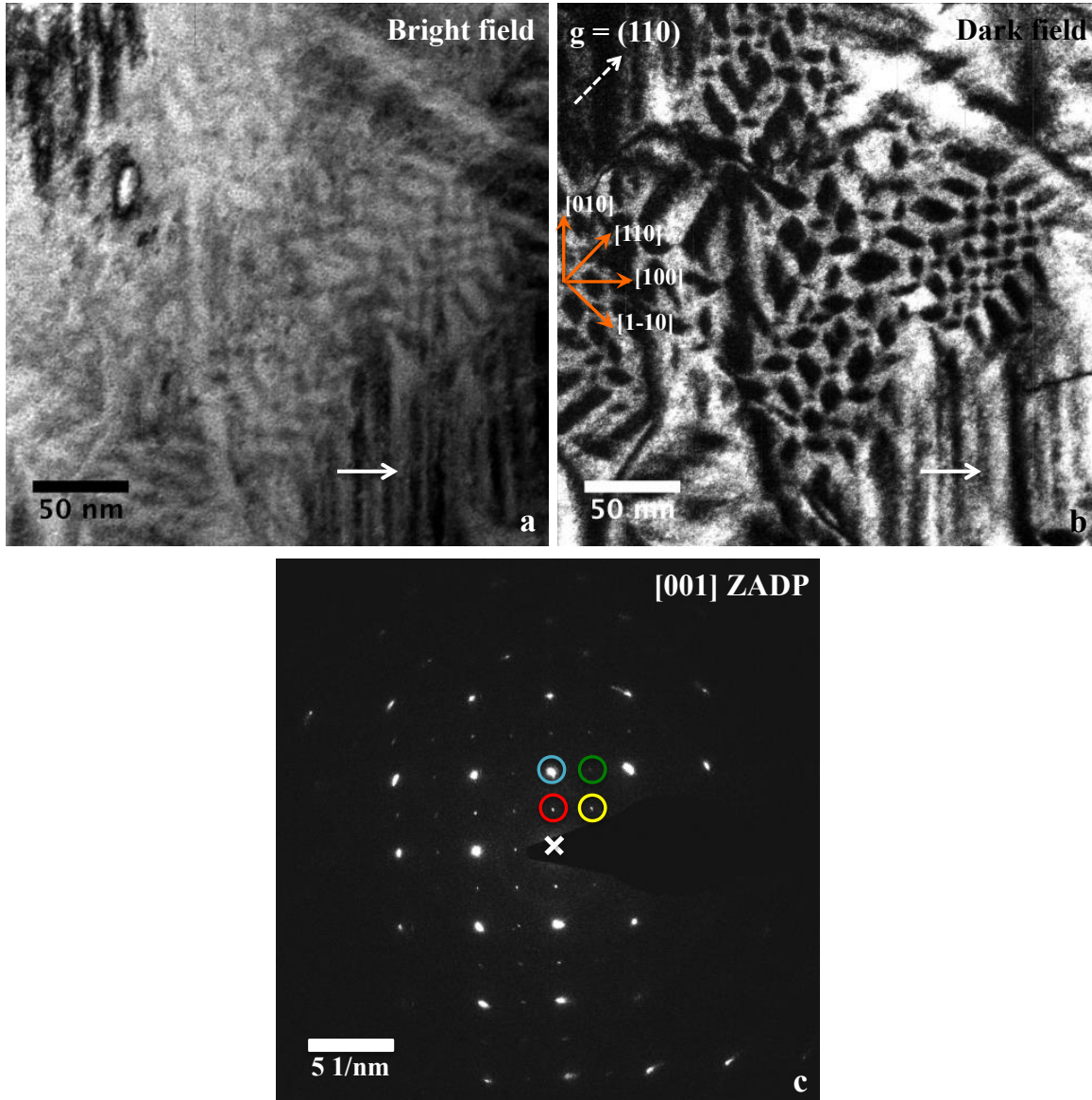


Figure 4.1: Conventional TEM images from Specimen S-80 of $Co_{40}Pt_{60}$ alloy. (a) Bright field TEM image, (b) (110) dark field TEM image showing nano-chessboard structure; solid white arrows in (a) and (b) are pointing to rods corresponding to nano-chessboard colony along the [010] crystallographic axis, (c) [001] zone axis diffraction pattern of region imaged in (a) and (b); the blue circle indicates fundamental reflection, the yellow circle indicates (110) superlattice reflection, the red circle indicates (010) superlattice reflection, and the green circle indicates (100) superlattice reflection, the white 'X' indicates the transmitted beam or (000) which has been blocked by the beam blocker in TEM. The relevant directions are marked in (b).

Fig. 4.2 shows another (110) DF TEM image from Specimen S-80 of $\text{Co}_{40}\text{Pt}_{60}$ alloy hosting several nano-chessboard colonies. Although this image displays nano-chessboard microstructures with uniform tile size and shape in most instances, several elongated or coarsened L1_0 plates can also be observed and are indicated by red arrows in the image. This type of L1_0 plates was also reported by Leroux et al. in [11]. They studied $\text{Co}_{38.5}\text{Pt}_{61.5}$ alloy aged at 700°C and allowed the sample to go through $\text{L1}_2 \rightarrow \text{L1}_0 + \text{L1}_2$ transformation instead of $\text{A1} \rightarrow \text{L1}_0 + \text{L1}_2$ transformation. This transformation first led to the formation of thin platelets of L1_0 in the L1_2 matrix (Fig. 4.3(a)), very similar to L1_0 plates shown by red arrows in Fig. 4.2. However, the further evolution of this structure resulted in the formation of thick L1_0 plates in the L1_2 matrix (Fig. 4.3(b)) with very similar distribution of L1_0 and L1_2 as in nano-chessboards. One such structure can also be spotted in Fig. 4.2, shown by marked circular area. Hence, it can be said that the regions that do not show perfect nano-chessboard structures have gone through slightly different transformations and ordering mechanisms, which can be attributed to the inhomogeneity in composition and temperature across the sample.

Another interesting microstructural feature observed in this alloy is Anti-phase Boundaries (APBs), shown by blue arrows in the image. This alloy consists of both the L1_0 and L1_2 ordered phases hence, APBs can be expected from the ordering of both the phases. From L1_2 phase ordering, APBs with displacement vectors $\mathbf{R} = [\frac{1}{2} 0 \frac{1}{2}]$ or $\mathbf{R} = [0 \frac{1}{2} \frac{1}{2}]$ or $\mathbf{R} = [\frac{1}{2} \frac{1}{2} 0]$ are to be expected [11]. In case of L1_0 phase ordering, for each orientation variant there are two translation variants therefore only one type of APB is possible. For example, the translation variants for orientation variant 'Z' are related with the displacement vector $\mathbf{R} = [\frac{1}{2} 0 \frac{1}{2}]$ or equivalently $[0 \frac{1}{2} \frac{1}{2}]$. The displacement vector 'R' can be determined by utilizing invisibility

criterion for defects and obtaining dark field images with suitable superlattice reflections [2]. Here, we haven't characterized the displacement vectors of APBs since a detailed analysis of different types of APBs found in this alloy has been previously reported [11], [82]. Since all the dark field images in this section were acquired using (110) superlattice reflection with sample oriented along [001] zone axis, the APBs that are visible in these images should correspond to $R = [\frac{1}{2} 0 \frac{1}{2}]$ or $R = [0 \frac{1}{2} \frac{1}{2}]$ for both the L1₀ and L1₂ ordering.

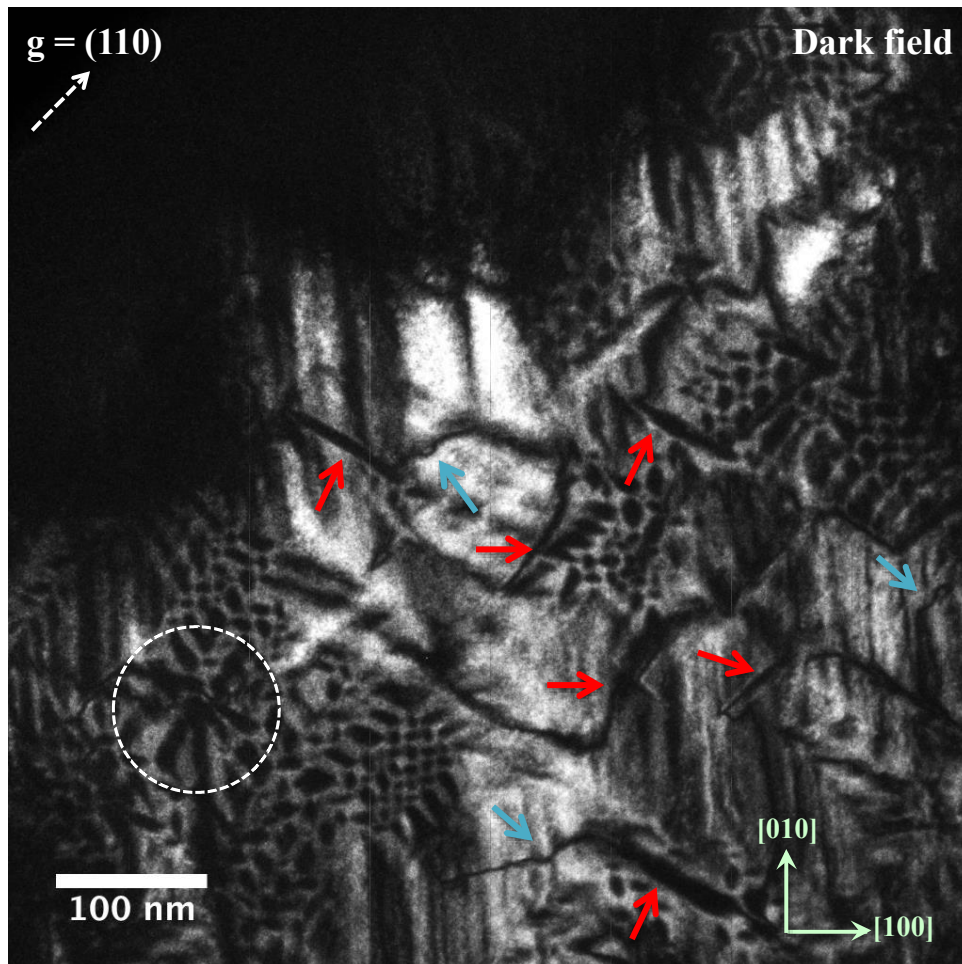


Figure 4.2: (110) Dark field TEM image from Specimen S-80 of Co₄₀Pt₆₀ alloy showing nano-chessboard colonies, red arrows point to coarsened L1₀ plates while blue arrows point to APBs, marked circular area is showing a different distribution of L1₀ plates; sample is oriented along [001] zone axis.

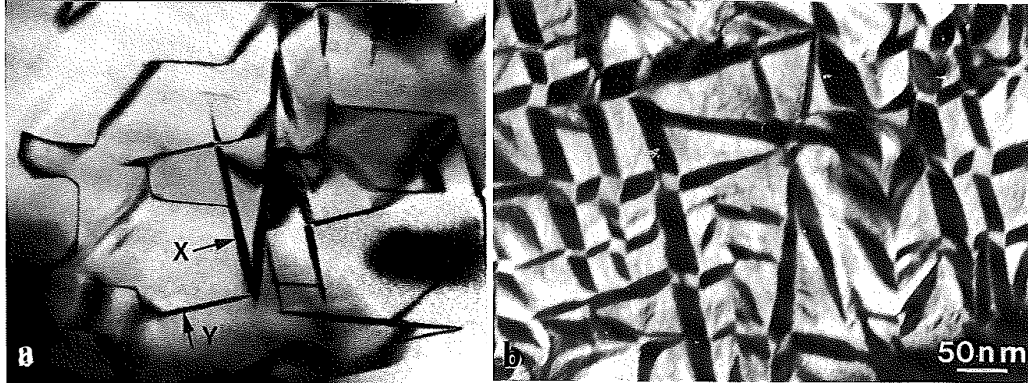


Figure 4.3: (110) Dark field TEM images of Co_{38.5}Pt_{61.5} alloy: (a) Fine L₁₀ platelets along <110> directions in the L₁₂ matrix, (b) Thick L₁₀ platelets in the L₁₂ matrix [11].

The DF TEM image shown in Fig. 4.4 perfectly sums up all the possible crystallographic microstructural features observed in this alloy. This image shows nano-chessboard colonies along all the three crystallographic axes. In addition, coarsened L₁₀ plates as well as anti-phase boundaries can also be spotted. The region enclosed by rectangular box shows a “band-shaped” structure in which L₁₀ bands are separated by a thin slice of L₁₂ phase as opposed to a square L₁₂ phase in the nano-chessboard structure. In the next two sections, we show additional relevant conventional TEM images for comparison with the magnetic domain structures observed in this alloy.

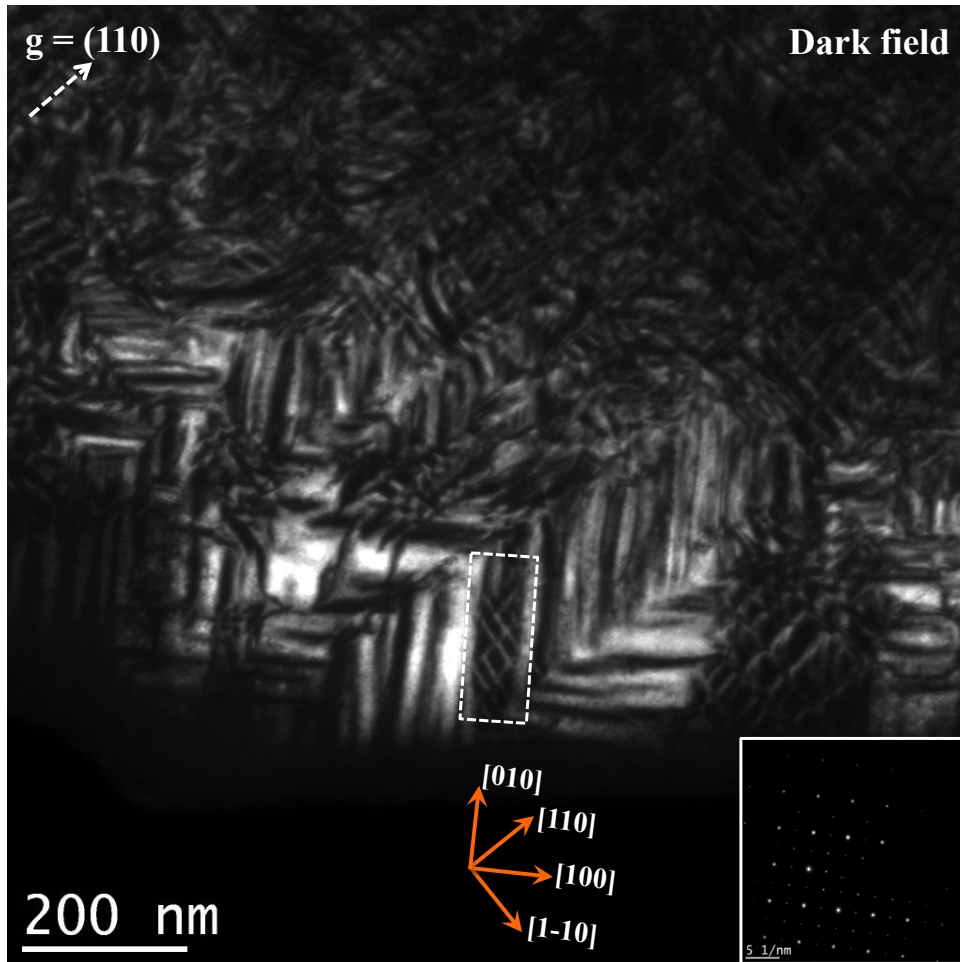


Figure 4.4: (110) Dark field TEM image from Specimen S-80 of $\text{Co}_{40}\text{Pt}_{60}$ alloy displaying all the possible crystallographic features possible in this alloy including nano-chessboards along all the three crystallographic axes, coarsened $L1_0$ bands/plates, and anti-phase boundaries; sample is oriented along [001] zone axis, diffraction pattern is shown in inset and relevant directions are marked in the figure.

4.3 Magnetic Domain Structure

The images in this section were acquired using an FEI Tecnai F20 microscope with a dedicated Lorentz pole piece, operated at an electron accelerating voltage of 200 kV. Fig. 4.5 shows a Lorentz Fresnel through-focus series of images from a region of Specimen S-40. A through-focus series of Fresnel images includes an in-focus image with no magnetic contrast, and over-focus and under-focus images with the same absolute defocus value. The magnitude of defocus,

$|\Delta f|$ should be as small as possible in order to perform the phase reconstruction from the through-focus series, and large enough to observe the domain wall contrast in the defocussed images. A higher defocus value will lead to a significant change of magnification and image rotation which will result in poor phase reconstruction. The Fresnel images in Fig. 4.5 are taken from a single grain. Note that this sample is polycrystalline and various crystal grains can be expected in a TEM thin foil. The exact orientation of the sample could not be identified because of the limitation of operating the Lorentz TEM in the diffraction mode as there is no suitable lens placed at the back-focal plane of the Lorentz lens. An effort was made to acquire diffraction pattern in Lorentz mode using a convergent beam and free lens control system in TEM. However, the diffraction patterns obtained were distorted mainly because the standard conditions for projecting and capturing diffraction patterns were not met. Nevertheless, a relative orientation between different magnetic features can be determined by comparing Lorentz TEM images with the conventional TEM images and electron diffraction patterns of similar regions as will be shown in this chapter.

The in-focus image shows diffraction contrast (dark features), and no magnetic contrast is visible. The over-focus image (Fig. 4.5(b)) shows a series of white and dark lines apart from the diffraction contrast. These lines correspond to regions of change in magnetization direction and are called magnetic domain walls. The magnetic domains in these regions are oriented in such a way that they give rise to a deflection of the electron beam and hence magnetic contrast. The under-focus image in Fig. 4.5(c) can be seen reversing the contrast of the lines, which is a characteristic of magnetic domain contrast. One such domain wall is pointed out by black arrow in the two images.

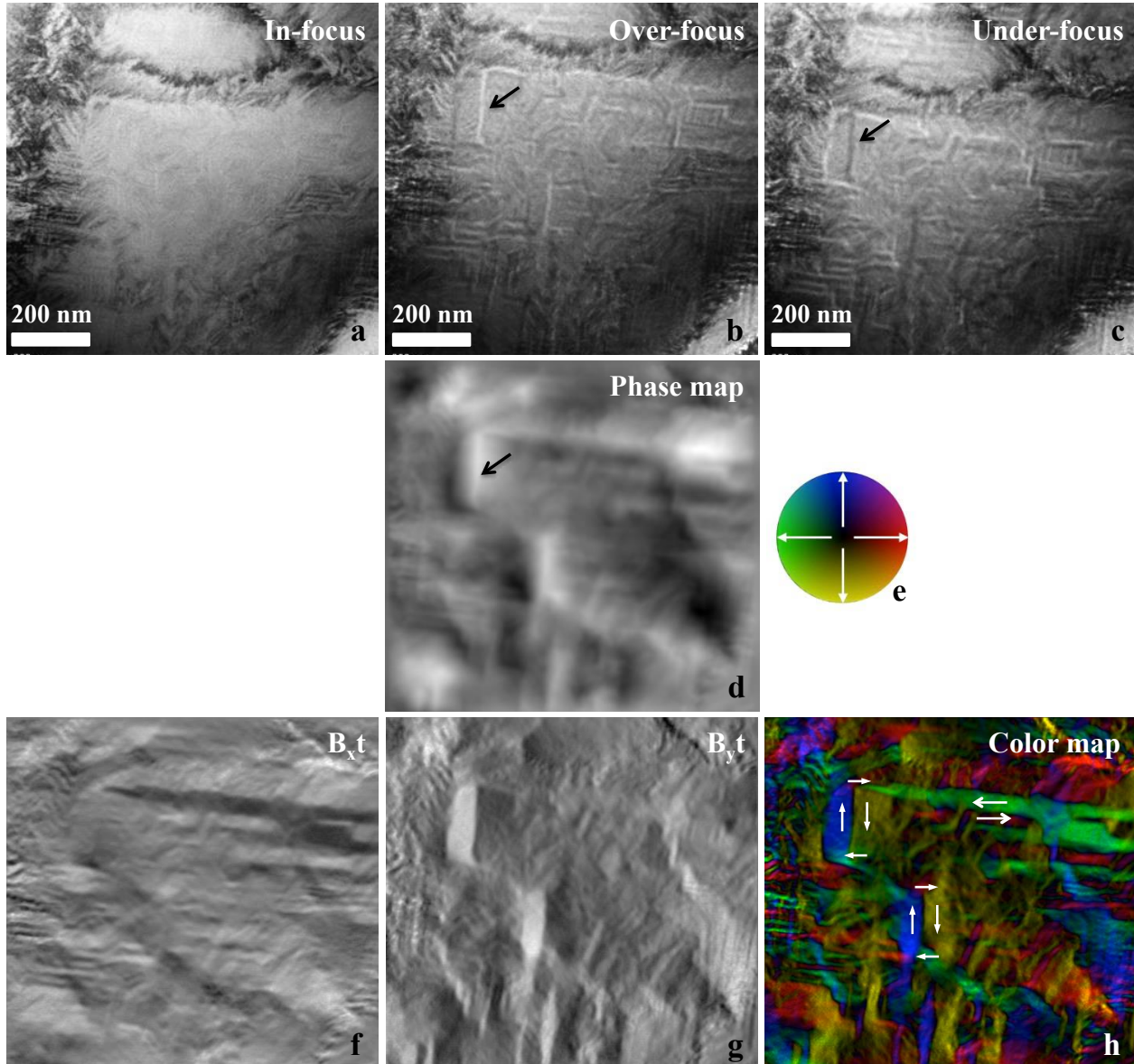


Figure 4.5: (a)-(c) Lorentz Fresnel through-focus series of images of $\text{Co}_{40}\text{Pt}_{60}$ alloy, the dark and white lines as shown by black arrows in (b) and (c) correspond to magnetic domain walls, (d) Reconstructed phase map, (e) Color legend, (f)-(g) Integrated B_{xt} and B_{yt} induction maps, (h) Color map with the arrows showing the magnetic configuration across 180° walls and 90° walls.

The over-focus and under-focus images have a slightly different magnification due to the very high lens defocus used to observe the domain walls. The two images are also shifted with respect to each other. The type of magnetic domain arrangement is dependent on the relative orientation of the easy axis of magnetization with respect to the thin foil normal. Straight domain walls are

indicative of an in-plane magnetization direction. The direction of in-plane integrated magnetic induction in a particular region of the thin foil can be obtained by reconstructing the phase of the electron waves from the Fresnel images as described in Section 3.5. Fig. 4.5(d) shows the reconstructed phase map. Although the defocus value of the Fresnel images was not calibrated, the topology of the phase map can be correctly extracted from the Fresnel images. Domain walls correspond to regions where phase map has curvature, i.e., ridges and valleys. The position of the domain wall pointed out in Fig. 4.5(b) and (c) is shown by black arrow in the phase map. Fig. 4.5(f) and (g) show the integrated in-plane magnetic induction components (integrated along the electron beam trajectory), B_{xt} & B_{yt} . The white contrast corresponds to a large induction component along the positive x -direction (from left to right), or the positive y -direction (from bottom to top); regions of dark contrast correspond to induction components in the negative x - and y -directions. A color map is generated from the induction maps as shown in Fig. 4.5(h); the color legend is shown in Fig. 4.5(e). The different colors in the color map show magnetic domains oriented along different directions with the in-plane directions represented by various colors in the color legend. Several white-colored vectors are overlaid in the color map to show the in-plane direction of magnetization of various domains.

Based on the reconstructed phase maps and color maps it can be inferred that the domain walls seen in the Fresnel images are 180° and 90° domain walls, since a 180° or a 90° change in orientation of magnetic induction across the domain walls is observed in the color map. The magnetic domain walls are visible as black boundaries separating the colored regions. Magnetic domain regions of varying shapes and sizes ranging from 70 nm to 700 nm are observed. The nature of the domain walls is either Bloch or Néel, but could not be determined from these

images. In addition, two closure-type magnetic configurations can be spotted in the color map with a clockwise rotation of magnetization, as shown by white arrows. Closure-type magnetic domain structure is considered to be the most stable domain configuration since it usually reduces the magnetostatic energy by minimizing the stray field. However, this structure is mostly observed in materials with more than one easy axis or soft magnetic materials since a closure-type configuration requires a change of magnetization direction.

The morphology of magnetic domains suggests three possible explanations for the observed magnetic domain structure. Firstly, the directionality of magnetic domains, such as the large green and red color rods/plates, strongly indicates that this magnetic region corresponds to the region of coarsened $L1_0$ tetragonal variants that seem to have grown randomly from the underlying precursor tweed structure. Since nano-chessboard formation is strongly dependent upon composition and temperature, a slight deviation in some part of the sample may have resulted in $L1_0$ growth instead of nano-chessboard. Hence, we observe different sizes & shapes of domains in the color map. These rod/plate like magnetic domains resemble the $L1_0$ plates in DF TEM images shown in Fig. 4.6. Similar features were observed in DF TEM image of an aged $Co_{40}Pt_{60}$ alloy shown in Fig. 2.14 [11]. It can be argued that the $L1_0$ plates in the Lorentz images are not visible in the in-focus image because it is a bright field image and only a dark field image acquired with a suitable diffraction spot will reveal the $L1_0$ plates. However, the over-focus and under-focus images reveal the presence of these variants/plates by revealing the location of magnetic domain walls inside/at the boundaries of these variants. The magnetization lies along the c-axis or the easy axis of the $L1_0$ variant. In this case, the green and red domains should correspond to the X-variants while the blue and yellow domains should correspond to the Y-

variants.

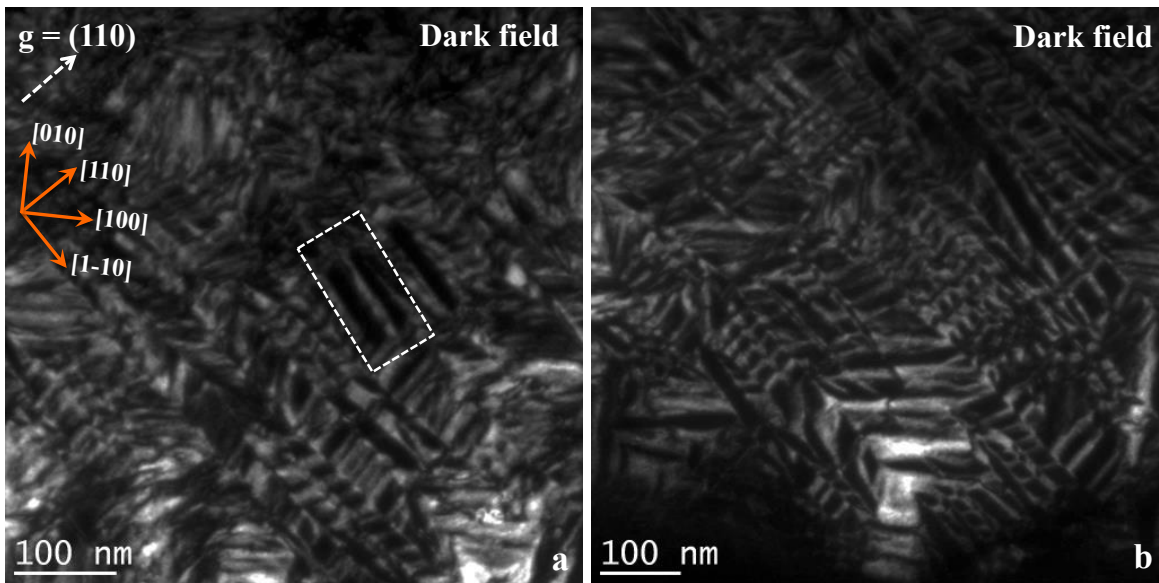


Figure 4.6: (a)-(b) Dark field TEM images of $\text{Co}_{40}\text{Pt}_{60}$ alloy from a region of coarsened L_{10} plates, marked rectangular area in (a) is highlighting two coarse L_{10} plates separated by a thin slice of L_{12} phase.

The second possible explanation lies in the assumption that this region of the sample could be over-annealed/over-aged leading to the coarsening of the nano-chessboard microstructure itself. The findings by [81] show that the coarsening of nano-chessboard usually leads to the growth of L_{10} tiles into L_{10} plates/rods consuming the neighboring L_{12} tiles. Hence, in DF TEM images, large L_{10} plates can be spotted separated by thin regions of L_{12} phase; one such instance is indicated by enclosed rectangular area in Fig. 4.6(a). This is in agreement with the closure-type magnetic configuration seen in the color induction map in Fig. 4.5(h). For example, assuming the blue and yellow color domains correspond to L_{10} phase, there isn't any evidence for the presence of a "large" L_{12} phase between the two plates. In this case, the magnetization direction of the thin slice of soft L_{12} phase is completely controlled by the neighboring hard L_{10} plates ensuring

a smooth transition of magnetization between neighboring $L1_0$ plates. This magnetic characteristic will be discussed in more detail in Section 4.4 where the magnetic domain structure of nano-chessboards has been explained.

On the other hand, if we assume that this part of the sample is in the initial stages of $L1_2 \rightarrow L1_0 + L1_2$ transformation as discussed in Section 4.2 and as also observed by [82], this will create large $L1_0$ plates in the $L1_2$ matrix. In this case, the explanation for the red/green magnetic domains remains the same. However, the regions with closure-type magnetic configuration should correspond to $L1_2$ regions. This is because the easy axes of magnetization of $L1_2$ phase lie along $\langle 100 \rangle$ directions and a closure-type magnetic structure would not only reduce magnetostatic energy but also reduce the magnetocrystalline anisotropy energy since the magnetization in all the four magnetic domains lies along the easy directions. However, this observation is contradictory to the domain wall width measurements shown in Section 4.7. The domain wall widths obtained for both the red/green rods as well as the closure configurations fairly match with the theoretical domain wall width for the hard $L1_0$ phase, which suggests that both the regions correspond to $L1_0$ phases. It should be kept in mind that the Lorentz Fresnel images are acquired at unknown sample orientations meaning it is possible that the sample may not be oriented along a zone axis hence only the in-plane component of overall magnetic induction gets projected in the color induction map instead of the total magnetic induction potentially giving rise to non-uniform shapes and sizes of magnetic domain contrast. Hence, the shape and size of magnetic domain contrast seen in Lorentz image may not exactly match with the shape and size of $L1_0$ plates observed in the dark field TEM images.

Fig. 4.7 shows Lorentz Fresnel images from another location in Specimen S-40. In the in-focus image (Fig. 4.7(a)), few bands of macro-twins can be observed; white-dashed lines show twin boundaries. Furthermore, macro-twins can be seen comprising fine twins/micro-twins with adjacent bands having orthogonal twins. In the under-focus image (Fig. 4.7(b)), magnetic domain walls inside the macro-twins are not clearly visible because of the strong diffraction contrast as well as the fact that the domain walls coincide with the twin boundaries. Another interesting feature in the under-focus image is shown by white arrow. These magnetic features resemble the magnetic contrast due to the nano-chessboard structure as will be shown in next section. However, the poor resolution of Tecnai microscope could not reveal the magnetic contrast of individual nano-chessboard tiles. The color induction map in Fig. 4.7(c) shows the in-plane magnetization direction orientation of each of the micro-twins. A magnified view of marked rectangular area in Fig. 4.7(c) is shown in Fig. 4.7(d). It is likely that the sample is not oriented along a zone axis hence a non-uniform distribution of colors is seen instead of perfectly alternating colors inside the micro-twins. In addition, the color induction map is integrated along the thickness of the sample, which means that all the magnetic domains (randomly oriented) along the sample thickness will contribute to the magnetic induction map. The color induction map of an idealized macro-twinned structure oriented along a zone axis should look like the figure shown in Fig. 4.7(e).

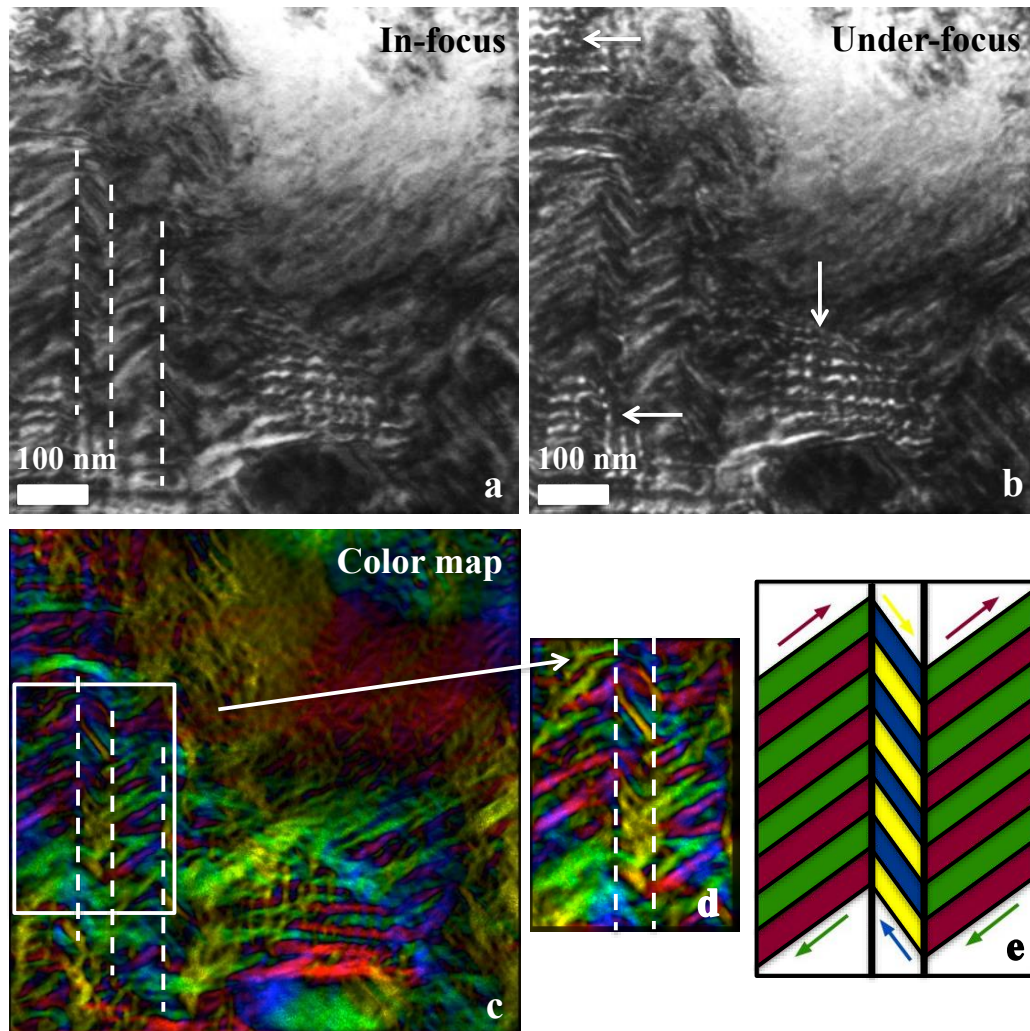


Figure 4.7: (a) Lorentz Fresnel in-focus image, white dashed lines show twin boundaries, (b) Under-focus image, white arrows point to nano-scale fine magnetic features, (c) Color induction map, (d) Magnified color induction map of twinned region, (e) Schematic idealized representation of magnetization orientation of macro-twinning plates.

Fig. 4.8 (a) and (b) show BF and DF TEM images, respectively from a location containing tweed microstructure in Specimen S-80. The ZADP of this region is shown in Fig. 4.8(d). The DF image was acquired using (100) superlattice reflection in a systematic row beam condition as shown in the inset in Fig. 4.8(b). The BF-DF image pair clearly shows the tweed contrast along $\langle 110 \rangle$ directions. This contrast is very similar to the tweed microstructure observed by many others in different Fe-Pt [36], Fe-Pd [15], [36] alloys. Apart from the tweed contrast, these

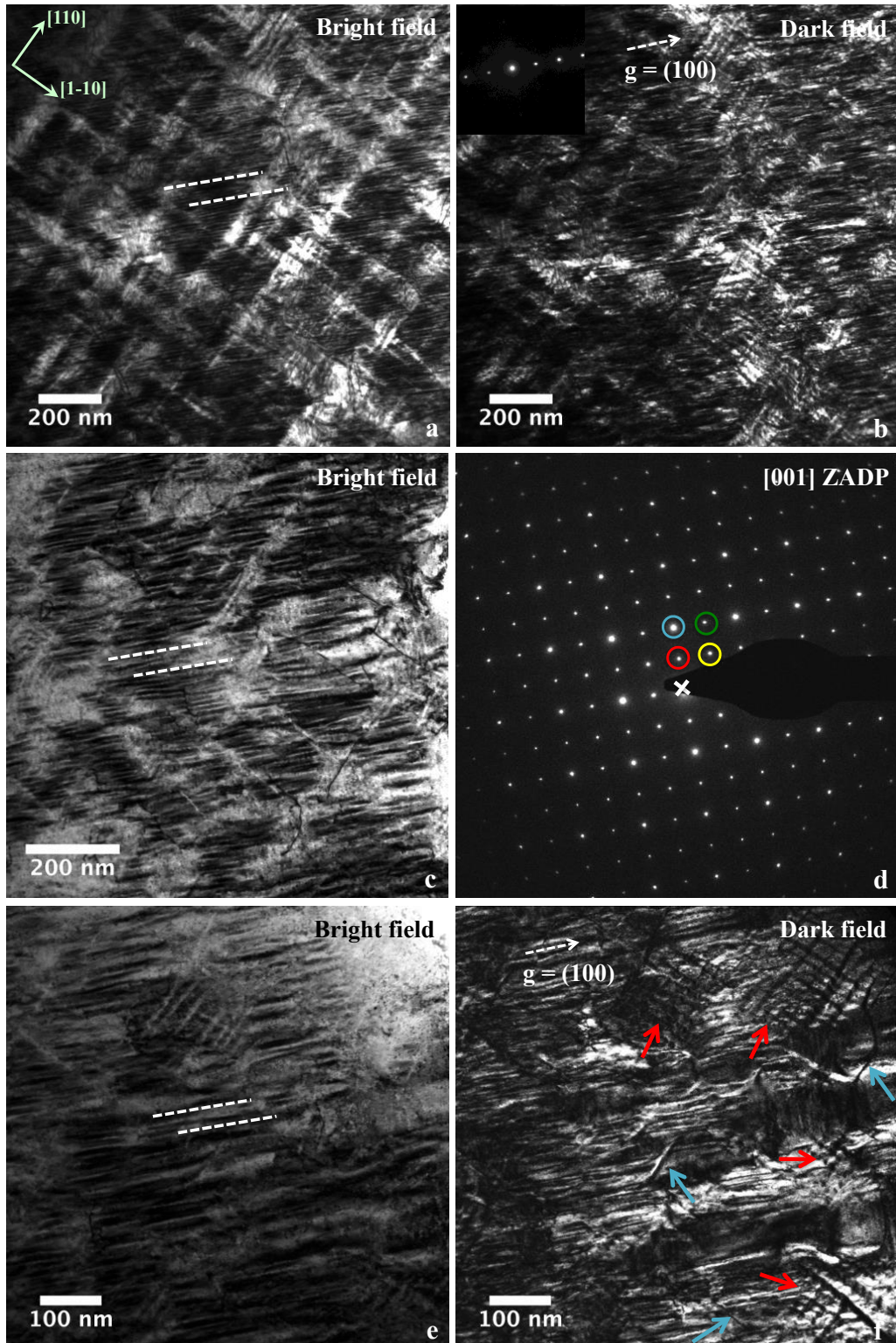


Figure 4.8: (a) Bright field image showing tweed microstructure, white dashed lines indicate striated features, (b) Dark field image corresponding to (a); inset shows diffraction condition used for imaging, (c) Magnified image of striated features, (d) [001] ZADP, (e)-(f) Bright field-dark field image pairs showing other microstructural features.

images show a striated contrast or fine plate shaped features along [100] direction. On observing high magnification images of similar regions (Fig. 4.8(c) & Fig. 4.8(e)), it is concluded that these features correspond to the rods of nano-chessboards oriented along [100] direction. Furthermore, the red arrows in Fig. 4.8(f) point to the nano-chessboard colonies oriented along [001] crystallographic axis. However, a perfect nano-chessboard contrast is not seen here because the superlattice reflection and beam/sample conditions employed here for DF imaging do not satisfy the conditions that lead to a perfect nano-chessboard contrast. The blue arrows point to several APBs.

Fig. 4.9 (a)-(c) show a Fresnel through-focus series of images from a tweed region of Specimen S-80 acquired in the Lorentz TEM mode. It should be noted that this is a similar region but may not be the same region as BF-DF image pairs shown in Fig. 4.8. The micrographs can be divided into two regions: the upper right part (region 1) and the lower left part (region 2). In the in-focus image, a tweed contrast can be clearly seen in region 1 while region 2 shows dark striated features very similar to that observed in Fig. 4.8. The in-focus image does not show any contrast other than diffraction contrast. However, the over-focus and under-focus images show long black and white features in region 1 that resemble 180° and 90° magnetic domain walls. These are magnetic domain walls associated with the tweed microstructure. Similar results were observed by Wang et al. in $L1_0$ Fe-Pt alloys [15]. Note the reversal of magnetic contrast and a slight change in magnification in the over-focus and under-focus images. The comparison of these images with the BF-DF image pairs shown in Fig. 4.8 easily confirms the tweed directions in the Fresnel images; the relevant directions are marked in Fig. 4.9(a).

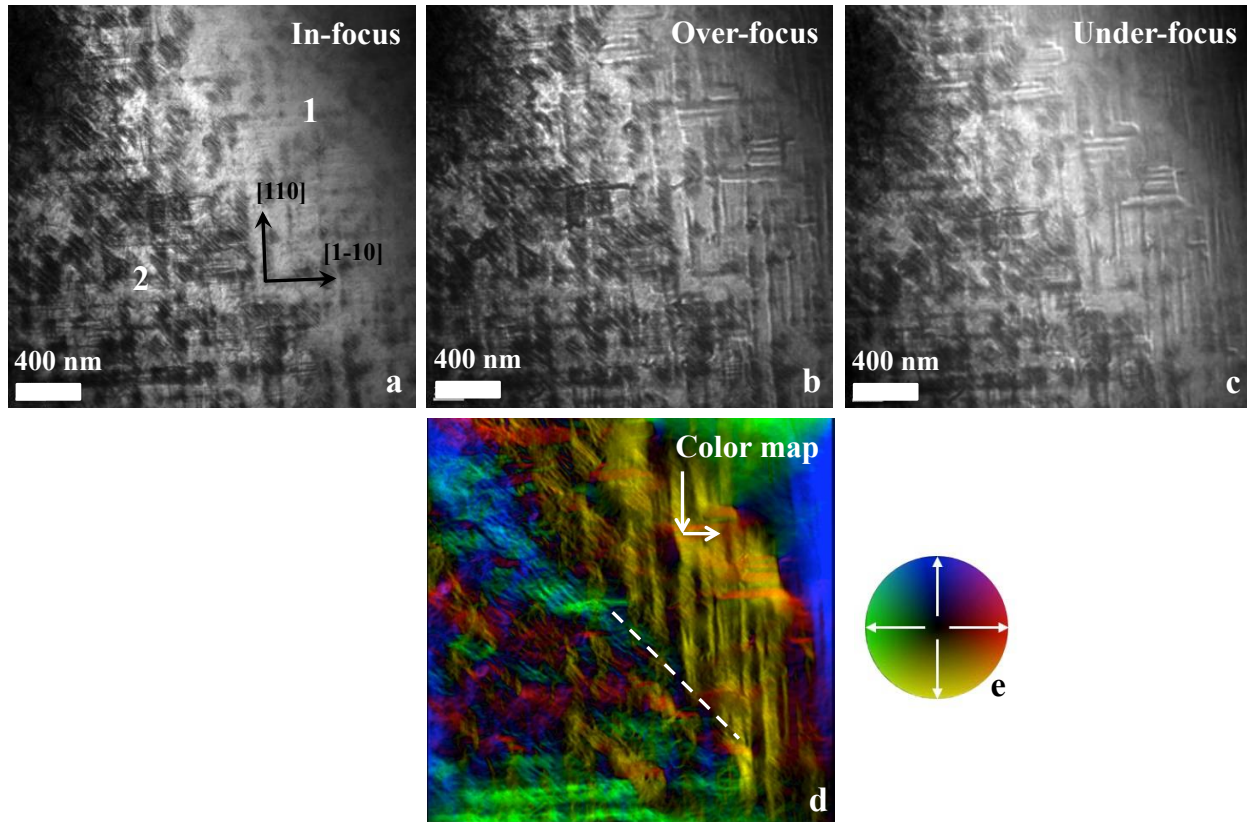


Figure 4.9: (a)-(c) Fresnel through focus series of images; black and white straight lines are domain walls, (d) Phase reconstructed color map, showing various magnetic domains, (e) Color legend.

Fig. 4.9(d) shows the phase reconstructed color map and the color legend is shown in Fig. 4.9(e). The tweed microstructure/contrast is a result of the relative arrangement of ordered $L1_0$ variants along different directions within the disordered matrix in order to accommodate the lattice mismatch strain produced during ordering. In our case, we will refer the tweed microstructure as a state of incomplete transformation of the parent FCC phase into the $L1_0$ - $L1_2$ nano-chessboard structure. The tweed microstructure contains all three variants of $L1_0$ nuclei oriented along $\langle 110 \rangle$ directions, however, only two variants of $L1_0$ persist as a result of continued annealing [15]. The easy axes of magnetization of the three $L1_0$ variants are along their c-axes ($M // \langle 001 \rangle$). An ideal sample, oriented along the $[001]$ zone axis inside the TEM, with all three $L1_0$ variants

(<001>) will have six magnetic domains, two of which will have out-of-plane magnetization direction ([001] & [00-1]) and the remaining four will have in-plane magnetization direction ([100], [-100], [010], [-010]). These in-plane magnetic domains will be seen as different colors in the color induction map: red for [100], green for [-100], blue for [010], and yellow for [0-10]. However, if the sample is tilted away from the zone axis only the in-plane magnetic components of the six magnetic domains will contribute to contrast in the Lorentz images. In this case, it is possible that the sample is not perfectly oriented along a zone axis and only the in-plane contribution of the various $L1_0$ magnetic domains is seen, as shown by different colors in the color map. In these structures, the magnetic domain walls coincide with the structural $L1_0$ boundaries. Hence, these magnetic domain walls are frozen or pinned at the structural boundaries and cannot move during the magnetization process. This results in an increased coercivity, as observed by others in similar types of alloys [15], [35]. As mentioned earlier, the tweed contrast observed in this part of sample may be a result of a lack of uniformity in composition or annealing conditions. The annealing time for this specimen (S-80) was less than that of Specimen S-40 and it is justifiable to say that the tweed structure in this region did not get sufficient time to grow and transform into $L1_0$ coarsened plates or macro-twinned plates as observed in case of Specimen S-40. The color induction map of region 2 also shows strong magnetic contrast corresponding to nano-rods that consists of two variants of $L1_0$ (X+Y or Y+Z or Z+X) and $L1_2$ phase. The magnetic contrast between adjacent nano-rods is clearly shown in Fig. 4.11. Another sample of same composition and annealing conditions as Specimen S-80 also shows similar type of magnetic domain walls associated with the tweed structure as shown in Fig. 4.10. The observation of this type of domain wall contrast in multiple regions across various samples lends credibility to our magnetic domain structure results.

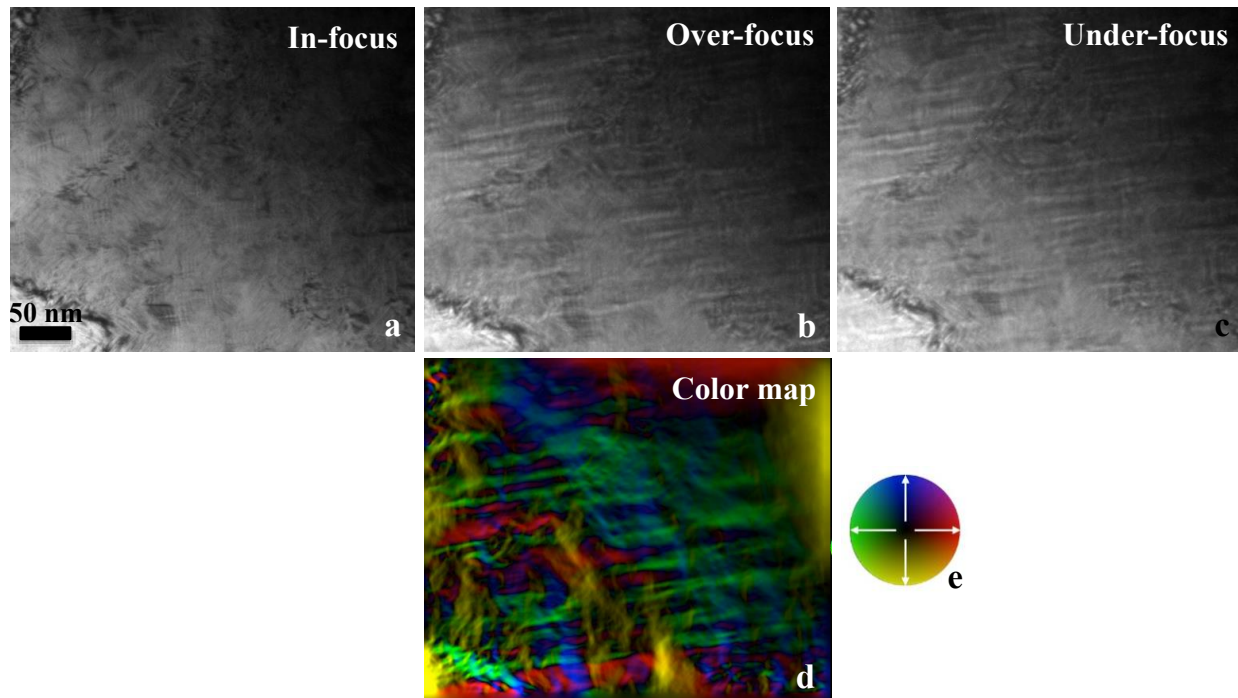


Figure 4.10: (a)-(c) Fresnel through-focus images; black and white straight lines are domain walls, (d) Phase reconstructed color map, showing various magnetic domains, (e) Color legend.

Fig. 4.11 shows Lorentz images from another location of Specimen S-80. A grain boundary can be seen across the middle of the micrograph, shown by a black arrow in Fig. 4.11(a). The right side of the grain boundary shows magnetic domain walls corresponding to the tweed microstructure. The left side of the grain boundary shows domain walls associated with nano-rods lying along $[100]$ and $[010]$ axis if it is assumed that the sample is oriented along $[001]$ zone axis. The curved dark features in the images are bend contours that arise due to the bending of the TEM thin foil. The color induction map (Fig. 4.11(c)) of the right side of the grain boundary does not reveal the magnetic domains clearly since the strong diffraction contrast interferes with the phase reconstruction and results in an unreliable color induction map. The induction map of the left side of the grain boundary clearly reveals all the fine $L1_0$ magnetic domains as shown in the magnified image in Fig. 4.11(d). Note that $L1_0$ variants have their c-axes/magnetic easy axes

perpendicular to each other hence we see a 90° (blue to green or red to yellow) change in magnetization in the adjacent $L1_0$ nano-rods. In addition, the phase shift profile (Fig. 4.11(e)) of the region marked by a white line in Fig. 4.11(d) shows the existence of two curved macro domain walls cutting across nano-rods. Thus, a change in contrast from blue/green to red/yellow and then again to blue/green is observed. The macro-domain walls are mobile; however, the coercivity will still be high since these domain walls will encounter multiple hindrances during their movement, in the form of $L1_0$ variant boundaries.

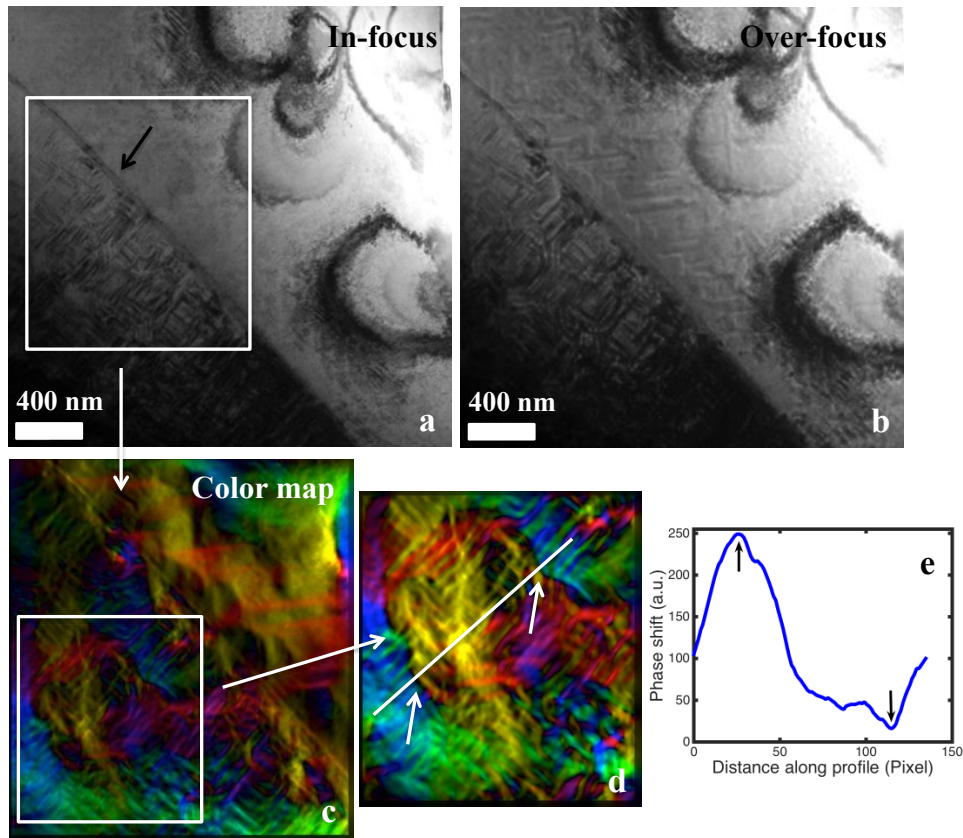


Figure 4.11: (a) In-focus image, (b) Over-focus image, (c) Color induction map of marked rectangular area in (a), (d) Magnified view of marked rectangular area in (c), (e) Phase shift profile of line/region marked in (d).

To compare the magnetic domain structure observations in this section with the bulk magnetic

properties, refer to Table 4.2. This table summarizes the observed magnetic properties for the samples studied in this work. It is to be noted that Specimen S-80 shows a higher remanence, coercivity and magnetic energy product as compared to Specimen S-40. All these properties are a measure of the resistance of ferromagnetic materials to the applied field. This resistance comes from the obstructions/defects that are encountered during the motion of a domain wall in response to the applied external field. Some of the defects include grain boundaries, twin boundaries, structural boundaries and anti-phase boundaries. Hence, magnetic properties can be directly related to the magnetic domain structure. While both the Specimen S-40 and S-80 are found to be composed of nano-chessboard structures and coarsened $L1_0$ plates, macro-twinned structure is only observed in S-40 while the tweed structure is only observed in S-80. A tweed microstructure will increasingly impede the motion of domain walls as compared to the macro-twinned structure due to the higher frequency of encountering $L1_0$ variant boundaries in the tweed structure. Hence, the relatively higher coercivity for Specimen S-80 can be attributed to the tweed structure. Since the bulk magnetic properties are a result of the contribution of the coercivity from all types of microstructures involved, the differences in magnetic properties between the two samples are justified.

Table 4-2: Bulk magnetic properties of $Co_{40}Pt_{60}$ alloys [1, 3].

Magnetic Property	S-40	S-80
Saturation Magnetization, M_s (A/m)	4.85×10^5	4.82×10^5
Remanence, M_r (A/m)	3.16×10^5	3.50×10^5
Coercivity, H_c (mT)	217.1	292.2
Maximum Energy Product, BH_{max} (J/m ³)	1.2×10^4	2.6×10^4

4.4 Magnetic Domain Walls in the Nano-chessboard Structure

The Lorentz Fresnel images shown in this section are acquired using spherical aberration correction in an FEI Titan 80-300 microscope with a dedicated Lorentz pole piece and operated at an electron voltage of 300 kV. Aberration correction in Lorentz mode has two advantages; firstly, it increases the maximum attainable resolution by reducing the spherical aberration of the Lorentz lens. Secondly, it also brings down the defocus value required to image the domain walls and makes Fresnel images more useful for quantitative analysis [83].

Fig. 4.12 shows Lorentz images from a region in Specimen S-40. Only in-focus and under-focus images are shown here (Fig. 4.12(a)-(b)). In the under-focus image, a zigzag repetitive pattern or ‘S’ shaped magnetic domain walls can be seen as white bright contrast. The corresponding phase map in Fig. 4.12(c) shows the positions of the domain walls. In addition, the white arrows in the phase map point to two separate sets of walls that are aligned at approximately 90° with respect to each other. The in-plane induction components shown in Fig. 4.12(d)-(e) also specify the location of various magnetic domains having horizontal and vertical magnetization components. The color induction map in Fig. 4.12(f) shows the in-plane magnetization integrated along the thickness of the specimen. A repetitive circular magnetization configuration consisting of yellow-red-blue-green colors can be seen in the color map. This configuration resembles the vortex-type magnetization arrangement observed in many magnetic materials [66], [84], [85]. Fig. 4.12(h) shows an experimental (-110) dark field TEM image showing a nano-chessboard structure from the same sample aligned along [001] zone axis [12]. The black tiles are the $L1_0$ phase and white tiles are the $L1_2$ phase. The red arrows in this image point to nano-rods aligned along other two orientations ([100] & [010]). By comparing the conventional nano-chessboard

image with the Lorentz color map, it is concluded that the repetitive vortex-type configuration (marked rectangular area in Fig. 4.12(f)) corresponds to different $L1_0$ tiles in the nano-chessboard structure.

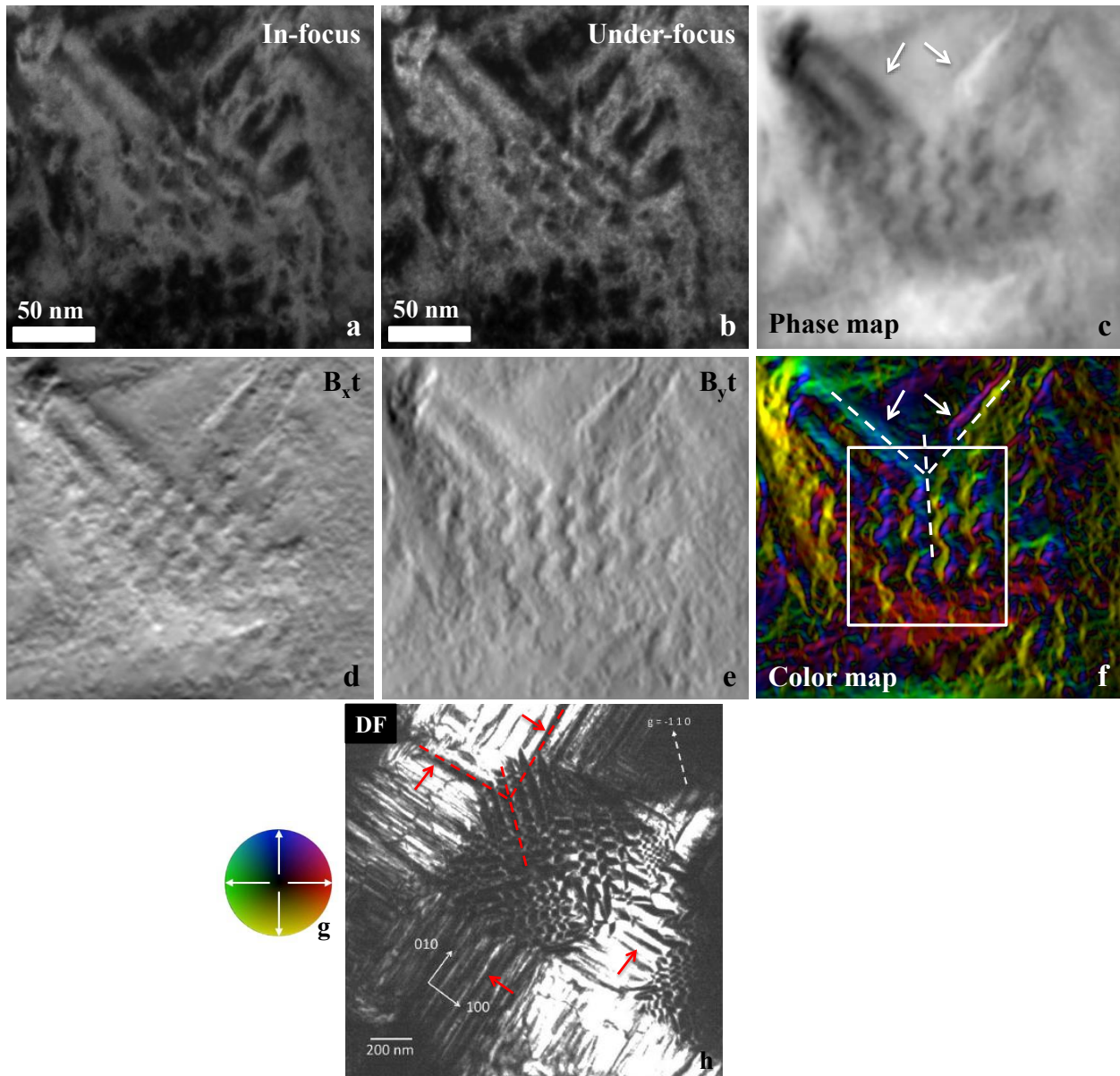


Figure 4.12: (a) In-focus image, (b) Under-focus image showing zig-zag domain walls, (c) Phase map, arrows point to nano-rods aligned along $[100]$ and $[010]$, (d)-(e) $B_{x,t}$ and $B_{y,t}$ maps, (f) Color induction map, (g) Color legend, (h) (-110) Dark field TEM image of nano-chessboard [12].

The white arrows in Fig. 4.12(c) and (f) are pointing to magnetic domain walls that are associated with the nano-rods oriented in [100] and [010] directions, as shown by red arrows in Fig. 4.12(h). Furthermore, the red dashed lines in Fig. 4.12(h) show the relative angles between the nano-chessboards aligned along the three axes, viewed along [001] direction. These angles match very well with the angles between white colored dashed lines in the color map. This further confirms our observation that the circular magnetization configuration corresponds to the nano-chessboard structure in which $L1_0$ and $L1_2$ tiles run along $\langle 110 \rangle$ directions.

Magnified images of the area marked by a rectangle in Fig. 4.12(f) are shown in Fig. 4.13. The overlaid magnetization vectors (white arrows) in the color map show the direction of magnetic induction in each of the $L1_0$ tiles. Each of the $L1_0$ tiles is a single magnetic domain whose magnetization points along the easy axes/c-axes of the tetragonal $L1_0$ phase. For example, a yellow color corresponds to $L1_0$ tile whose magnetization lies along [0-10] direction. The other neighboring $L1_0$ tiles contribute red [100], green [-100], or blue [010] color to the magnetic induction map. The alternate in-plane easy axis in adjacent $L1_0$ tiles leads to a vortex-type magnetic configuration so as to minimize the system energy by minimizing both the magneto-crystalline anisotropy energy and the magneto-static energy. In this case, an anti-clockwise sense of rotation of magnetization can be observed. The square region in the phase map, $B_x t$ map, and $B_y t$ map can be seen showing a point-like contrast. The corresponding color induction map shows a perfect vortex structure in the magnified view of the square region in the color map. This can be explained as follows. $L1_0$ tiles of varying length-scales are observed in the DF TEM image of nano-chessboard structure shown previously. When the length-scales of adjacent $L1_0$ tiles become smaller than a critical value they tend to form a perfect vortex magnetic structure. In this

case, the vortex center lies at the center of an L₁₂ tile which is surrounded by four L₁₀ tiles.

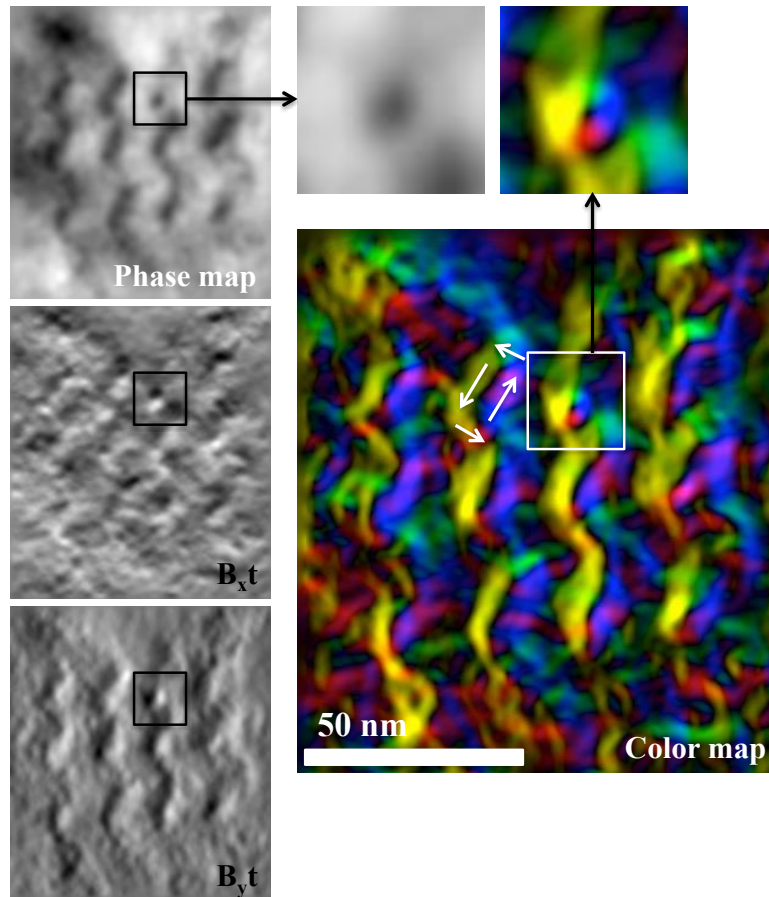


Figure 4.13: Magnified images of marked rectangular area in Fig. 4.12(f).

TEM and VSM studies by Ghatwai et al. [12] on samples with compositions bracketing the two-phase eutectoid region - $\text{Co}_{41.7}\text{Pt}_{58.3}$ and $\text{Co}_{37.6}\text{Pt}_{62.4}$ which predominantly contained L₁₀ phase and L₁₂ phase respectively, demonstrated a Curie temperature of 419°C for the L₁₀ phase and a Curie temperature of 354°C for the L₁₂ phase. They claimed that these Curie temperatures should also apply to the compositions within the two-phase existence region and therefore to the L₁₀ and L₁₂ phases of the nano-chessboard structure. Furthermore, the stoichiometric L₁₀ structured CoPt is known to have a Curie temperature of 567°C [21] whereas stoichiometric L₁₂

structured CoPt_3 has a Curie temperature of 15°C [86]. Thus, we see that the deviations from stoichiometry significantly affect the value of the Curie temperature and hence the magnetic behavior of the alloy. Hence, the Curie temperatures of the individual L1_0 and L1_2 phases of the nano-chessboard in our samples ($\text{Co}_{40.2}\text{Pt}_{59.8}$) cannot be predicted accurately. However, it is evident that the L1_0 phase is largely ferromagnetic at room temperature while the same cannot be said about the L1_2 phase. The L1_2 phase could be soft magnetic or paramagnetic at room temperature. In either case, we believe that the magnetization of L1_2 tiles is strongly modified/influenced by the neighboring hard L1_0 tiles due to their close proximity at a length-scale of a few nanometers in the nano-chessboard structure. The L1_2 region essentially acts as a magnetic domain wall connecting the two L1_0 tiles with opposite magnetization. This type of magnetic domain wall has never been reported before. The domain walls that have been reported in the past usually exist within one crystallographic phase [15], [16], [87]. We propose that this wall is what we call an Inter Phase Magnetic Domain Wall (IPMDW). An IPMDW is a domain wall that encompasses a region containing two different crystallographic phases, in this case the L1_0 and L1_2 phases. The formation of an IPMDW is critically dependent on the following factors:

1. The two phases should have a coherent interface. A coherent interface will make sure that the transition of magnetization happens smoothly across the interface.
2. It is also necessary for one of the phases to be able to influence the magnetization direction of the other, so one of the phases should be a strong hard magnetic phase while the other phase should be a relatively softer magnetic phase.
3. Finally, the length scales of the individual phases have to be smaller than the critical size for single magnetic domain particle otherwise a domain wall could be nucleated inside

the individual phases, negating the need for an IPMDW.

In the case of the samples analyzed here, all the conditions mentioned above are satisfied. The L1₀ and L1₂ tiles have coherent interfaces in the nano-chessboard structure and the L1₀ phase is a hard uniaxial magnet while the L1₂ phase is a soft magnet. In addition, the theoretical single domain particle sizes for L1₀ and L1₂ phases were determined to be ~995 nm and ~75 nm respectively using experimentally obtained exchange constant and anisotropy constants: $A(L1_0, L1_2) = 2.5 \times 10^{-11}$ J/m and $K(L1_0) = 1.5 \times 10^6$ J/m³, $K(L1_2) = 2 \times 10^4$ J/m³ for both phases [12]. The length-scale measurements show that the size of both the L1₀ and L1₂ tiles are well below the calculated limit of their respective single domain particle size. Hence no domain wall formation is expected inside the individual tiles. However, the opposite magnetization between two adjacent L1₀ tiles necessitates the formation of a domain wall between them to minimize the exchange energy, and this is only possible if a domain wall is formed across the L1₂ region between the two L1₀ tiles, as schematically shown in Fig. 4.14. In this figure, the red lines represent the phase boundary between the L1₀ and L1₂ phases while the wide yellow band represents the magnetic domain wall of wall thickness 'δ'. Black and white bands represent L1₀ and L1₂ phases, respectively. Three separate cases are considered. In the first case, the domain wall lies well within the L1₂ phase with the magnetization of remaining L1₂ phase conveniently aligned along the magnetization of L1₀ neighboring tiles. In case II, it is proposed that the domain wall encompasses the whole L1₂ phase and also extends into the neighboring L1₀ phases. In case III, the phase boundaries between the L1₀ and L1₂ phases coincide with the two ends of a domain wall hence the domain wall encompasses the L1₂ phase in its entirety. At such fine length-scales of a few nano-meters and given the limited resolution in Lorentz mode, it is

currently not possible to determine by direct observation, which of the three cases is most accurate. However, our results so far strongly suggest the existence of an IPMDW.

In summary, the formation of IPMDW and vortex-magnetic configuration in nano-chessboard structure is a direct result of the balance between the magneto-crystalline anisotropy energy, exchange energy, and magneto-static energy at a length scale of a few tens of nanometers.

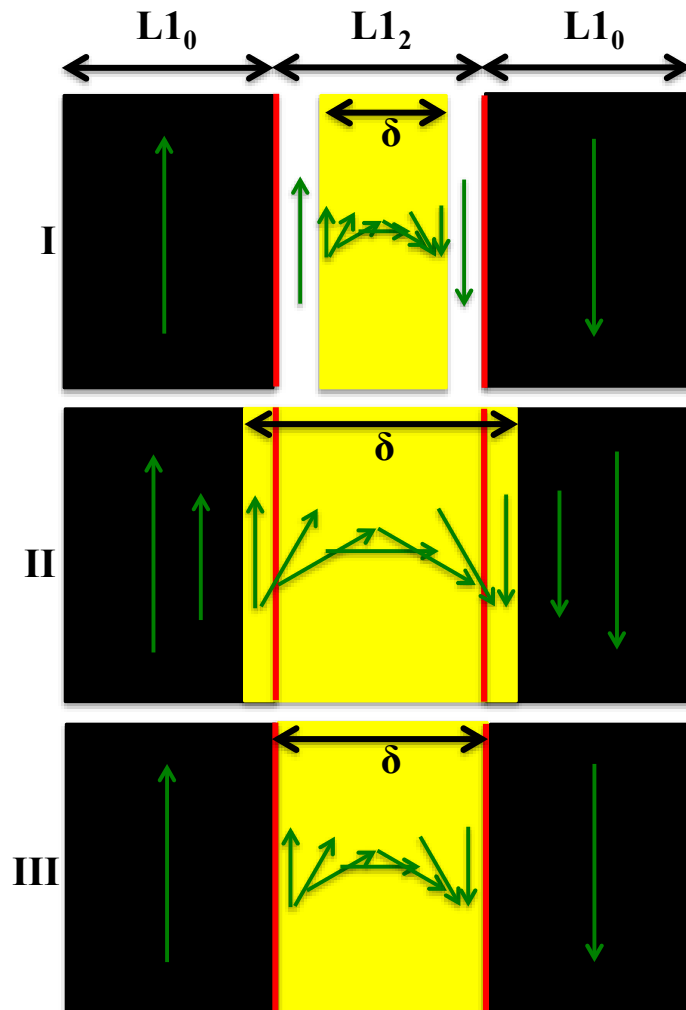


Figure 4.14: Idealized figure showing formation of inter phase magnetic domain wall (IPMDW) between $L1_0$ and $L1_2$ phases in the nano-chessboard structure.

Fig. 4.15 shows Lorentz images from a region in Specimen S-80. A zigzag/S-shaped domain wall can be clearly seen in the over-focus image and the phase map (Fig. 4.15(a)-(b)). B_{xt} and B_{yt} maps in Fig. 4.15(c)-(d) show the horizontal and vertical components of the magnetic induction. Fig. 4.15(e) shows the color induction map. A similar vortex-type magnetic configuration as observed in Specimen S-40 can be seen repeating here. Here, the length-scale of tiles/domains seems to be even smaller than in Specimen S-40. Since S-80 sample is cooled at a faster rate as compared to S-40, during thermal processing of the disordered A1 phase, nano-chessboards with reduced length-scale are observed for S-80 as compared to S-40. Thus, fine scale vortex magnetic configurations can be frequently spotted here.

Fig. 4.15(g) shows a magnified image of the three vortex configurations enclosed in a rectangular box in Fig. 4.15(e). In between two adjacent vortex configurations, an anti-vortex configuration can be seen. Interestingly, the three vortex configurations are spotted as bright spots in the phase map while the anti-vortex configurations can be seen exhibiting black domain wall-like contrast (Fig. 4.15(h)). These domain walls, shown by white dashed lines in the color map appear to be 90° domain walls since they are seen separating blue and red colored magnetic domains as well as green and yellow color domains. The phase profile drawn for the region shown by a white solid line in the phase map shows the intensities of vortices (shown by black arrows) and intensity of anti-vortex domain walls (shown by red arrows). A close look at Fig. 4.13 also reveals the anti-vortex pattern between the two vortex patterns; however they are not as apparent as here, due to highly distorted domains, possibly because of higher disorientation from zone axis.

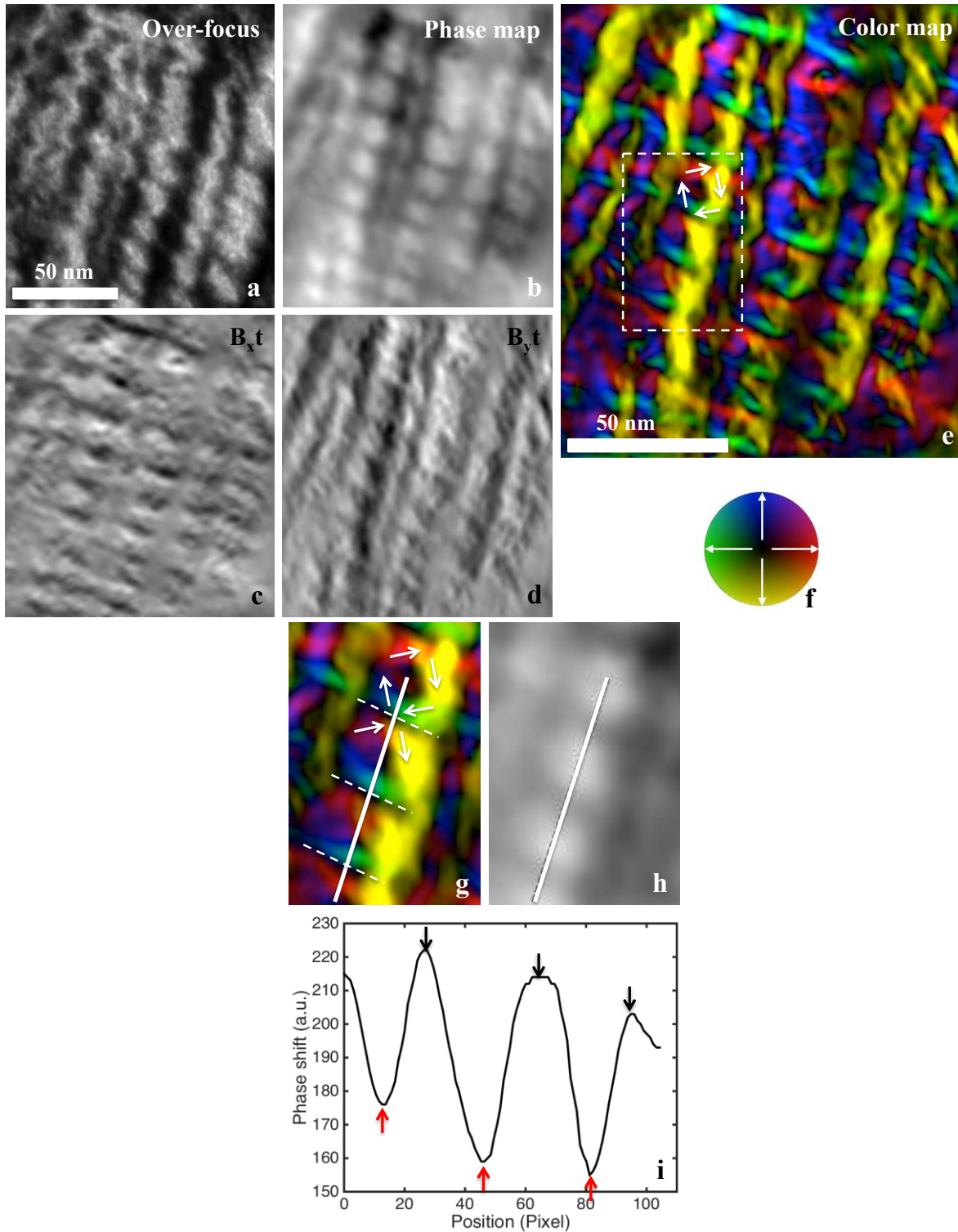


Figure 4.15: (a) Over-focus image, (b) Phase map, (c)-(d) B_{xt} and B_{yt} maps, (e) Color map, (f) Color legend, (g)-(h) Magnified color map and phase map of rectangular area marked in (e), color map shows anti-vortex pattern and vortex pattern, white dashed lines show position of anti-vortex domain wall, (i) Phase shift profile of region marked by white solid line in (h), pixel size is calibrated as 0.45 nm.

The length-scale of $L1_0$ tiles in the DF TEM images are compared with the size of magnetic domains in the color induction map. In Specimen S-80, the length-scale measured from the color map matches, to a reasonable degree, with that measured from the DF image with both the size of $L1_0$ tiles and magnetic domains varying between 4 nm to 18 nm. In Specimen S-40, a slight discrepancy in the length-scales measured from the color map and DF image was observed. The size of $L1_0$ tiles in the DF image varied from ~7-34 nm while the size of magnetic domains were ~2.5-19 nm. This can be understood from the fact that the sample in Lorentz TEM may not be perfectly oriented along a zone axis and/or the two images could be from different regions of the sample. In addition, a perfect diamond shaped magnetic domain is not observed in the color maps. Since only in-plane magnetization contributes to the color map/magnetic contrast, the out-of-plane magnetization component of a randomly oriented sample does not get accounted for in the color maps, which results in a not-so-perfect diamond shaped magnetic domains.

In summary, both the specimens S-40 and S-80 exhibit vortex-type magnetic configurations in the nano-chessboard structure. In addition, formation of an unusual magnetic domain wall – “IPMDW” is observed in both the specimens. The IPMDW is hypothesized to be pinned/frozen between the $L1_0$ and $L1_2$ phases, since it cannot move past the phase boundary during the magnetization process. One of the reasons for a relatively higher coercivity in S-80 as compared to S-40 could be the existence of a large number of IPMDWs per unit volume of the sample, due to the relatively fine-scale nano-chessboards in Specimen S-80.

4.5 Phase Shift Simulation of Nano-chessboards

4.5.1 Micro-magnetic simulations methodology

Micro-magnetic simulations of the two-phase Co-Pt nano-chessboard structure were performed by [14] as follows. The two-phase structure is characterized by a phase field variable $\theta(\mathbf{r})$ which assumes a value of 1 for the tetragonal $L1_0$ phase and 0 for the cubic $L1_2$ phase. In the $L1_0$ phase, the local orientation of tetragonal axis is further characterized by a vector field $\mathbf{t}(\mathbf{r})$, which alternates between $[100]$ and $[010]$ in neighboring $L1_0$ tiles. The magnetic domain structure is described by a directional magnetization vector field $\mathbf{M}(\mathbf{r})$ which depends on the two-phase microstructure as shown below:

$$\mathbf{M}(\mathbf{r}) = M_s(\mathbf{r})\mathbf{m}(\mathbf{r}) = [M_s^{L1_0}\theta(\mathbf{r}) + M_s^{L1_2}(1 - \theta(\mathbf{r}))]\mathbf{m}(\mathbf{r}), \quad (4.1)$$

Here, $M_s(\mathbf{r})$ is the magnitude of the spontaneous magnetization and $\mathbf{m}(\mathbf{r})$ is the unit vector field of magnetization. $M_s^{L1_0}$ and $M_s^{L1_2}$ are the saturation magnetizations of the $L1_0$ phase and $L1_2$ phase, respectively. The evolution of magnetic domain structure is described by the Landau-Lifshitz-Gilbert equation that depends on the system free energy. The free energy of the two-phase magnetic Co-Pt system is given by the sum of magnetocrystalline anisotropy energy, exchange energy, magnetostatic energy, and Zeeman energy. In this case, the magnetocrystalline anisotropy function depends on the underlying microstructure and is given by:

$$f^{an} = K_1^{L1_0}\{1 - [\mathbf{t}(\mathbf{r}) \cdot \mathbf{m}(\mathbf{r})]^2\}\theta(\mathbf{r}) + K_1^{L1_2}[m_1^2(\mathbf{r})m_2^2(\mathbf{r}) + m_2^2(\mathbf{r})m_3^2(\mathbf{r}) + m_3^2(\mathbf{r})m_1^2(\mathbf{r})](1 - \theta(\mathbf{r})), \quad (4.2)$$

where $K_1^{L1_0}$ and $K_1^{L1_2}$ are the magnetocrystalline anisotropy constants of the $L1_0$ phase and $L1_2$ phase, respectively. As the interfaces in the Co-Pt nano-chessboard structures are fully coherent, and the compositions are very similar, constant exchange stiffness (A) is assumed across $L1_0$ and

L1₂ phases. The material parameters used in the simulations are summarized in the table below.

Table 4-3: Material parameters of Co₄₀Pt₆₀ alloy [12], [14], [58].

Phase	M_s (A/m)	K (J/m ³)	A (J/m)
L1 ₀	4.2×10^5	1.5×10^6	2.5×10^{-11}
L1 ₂	5.2×10^5	2×10^4	2.5×10^{-11}

The magnetic domain structure is computed for a tile size (L1₂ square tile) of $d = 36$ nm. A 256×256 computational cell is used, with pixel size 1.5625 nm. The 2-D magnetization unit cell satisfies periodic boundary conditions in the nano-chessboard plane as well as smooth magnetization transitions at the phase boundaries. Additionally, it is assumed that the nano-chessboard colony is uniform along the third dimension or the z -axis. The micro-magnetic simulation result produces a three-dimensional (3-D) magnetization vector $M(i, j)$ for each pixel (i, j) in the 2-D unit cell. This magnetization vector field is used as an input for our phase-shift calculations. Phase shift maps for the nano-chessboard structure are simulated using both the Beleggia method and the Mansuripur method as described previously in Section 3.4.1. Since both methods yielded similar results, only the results obtained via Mansuripur method are discussed in this section. From the simulated phase shifts, Lorentz Fresnel images and integrated in-plane magnetic induction maps are simulated as explained in Sections 3.4.2 and 3.4.3. These results are then compared to the experimentally obtained Lorentz Fresnel images and magnetic induction maps in the next section.

4.5.2 Magnetic contrast at zero beam tilt

Fig. 4.16 shows a set of simulated images. Fig. 4.16 (a)-(c) are the output magnetization maps obtained from the micro-magnetic simulations. Note that the sample is assumed to be oriented

along the [001] zone axis in this simulation. The white contrast indicates magnetization along $+x$, $+y$ and $+z$ directions while the black contrast indicates magnetization along $-x$, $-y$, and $-z$ directions in M_x , M_y , and M_z maps, respectively. The square tiles correspond to the $L1_2$ phase whereas the diamond tiles correspond to the $L1_0$ phase. As can be seen, only $L1_0$ tiles have in plane magnetization while $L1_2$ tiles are magnetized in the out-of-plane direction for this magnetization state. Fig. 4.16(d) shows the calculated phase map from this magnetization data. The numerical value of magnetic phase shift ranges from -29.89 rad to 28.41 rad. Fig. 4.16 (e)-(f) are the integrated in-plane magnetic induction maps. Fig. 4.16(g) shows the color induction map. It is evident from the color map that the $L1_0$ tiles exist as single magnetic domains with their magnetization direction dictated by the magnetic easy axes, shown by different colors. Two circular vortex-type configurations with an anti-vortex pattern in between are highlighted by the white arrows in the color map. This type of repetitive vortex and anti-vortex configuration was also observed in the experimental color maps which were shown in the previous section. Fig. 4.16 (h)-(j) are the simulated Lorentz Fresnel through-focus series images. The domain walls can be clearly seen as white and dark contrast in the defocussed images.

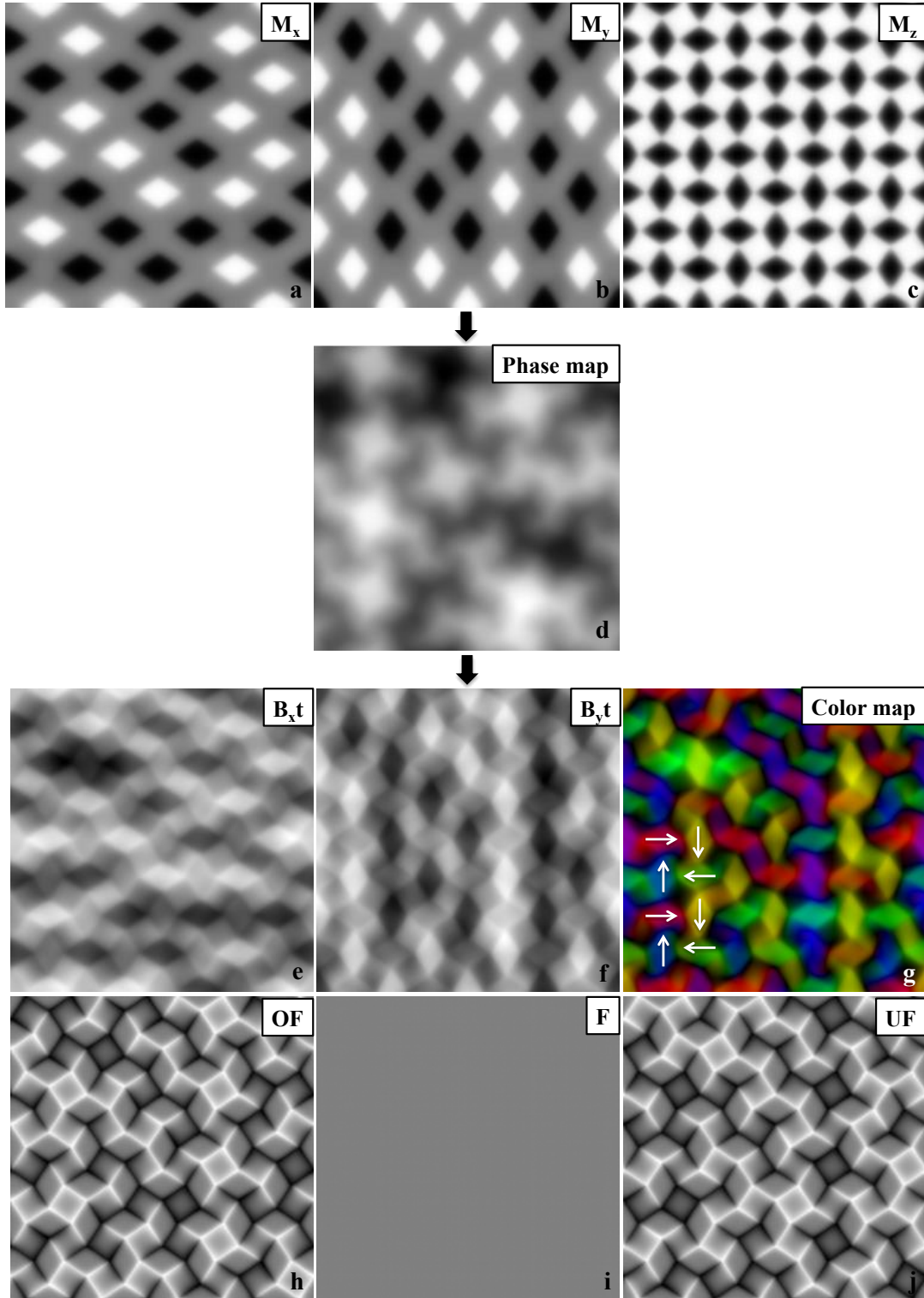


Figure 4.16: Simulated images: (a)-(c) M_x , M_y , M_z extracted from micro-magnetic simulation of nano-chessboard, (d) Simulated phase map, (e)-(f) $B_{x,t}$ and $B_{y,t}$ maps, (g) Color map, white and black arrows showing vortex and anti-vortex pattern, respectively, (h)-(j) Fresnel through focus images. All images are 256×256 pixel, 256 pixel = 400 nm.

4.5.3 Beam tilt effect on magnetic contrast

Since the long-focal length Lorentz lens used for magnetic imaging has its back-focal plane near the conventional selected area aperture plane, it is often difficult to obtain electron diffraction patterns with a low pattern distortion. Hence, the experimental Fresnel images are usually acquired at unknown sample orientations implying that it is important to analyze the tilts with respect to specific zone axes. A clockwise sample tilt inside the TEM is equivalent to an anti-clockwise tilt of the electron beam, hence the magnetic contrast in the experimentally obtained magnetic induction color maps can be analyzed by comparing it with simulated color maps generated for different beam tilts. Only the in-plane component of magnetization gives rise to magnetic contrast. As the beam is tilted, the angle between the electron beam and the sample normal changes the projected in-plane magnetization components and, thus, produces a different magnetic contrast. The Mansuripur algorithm properly projects a magnetic structure that is constant along z -axis, so, we expect the resulting phase maps and induction maps to be accurate for the tilting range typically used in TEM experiments. In case of nano-chessboard structure, as the sample is tilted away from the zone axis $[001]$, the in-plane magnetic component corresponding to each $L1_0$ tile changes and a non-symmetrical distribution of colors is seen in the color map. This asymmetry in the magnetic contrast can be seen in the simulated color maps obtained at various angles of beam tilt. As shown in Fig. 4.17, the red and green color contrast (horizontal in-plane components) becomes more pronounced as the beam is tilted around the x -axis. Similarly, the blue and yellow color (vertical in-plane components) contrast enhances as the beam is tilted around the y -axis (Fig. 4.18). This contrast change is obvious since tilting the sample/beam around the y -axis or x -axis will lead to a lower/negligible contribution from the magnetic domains magnetized along the x -axis or y -axis.

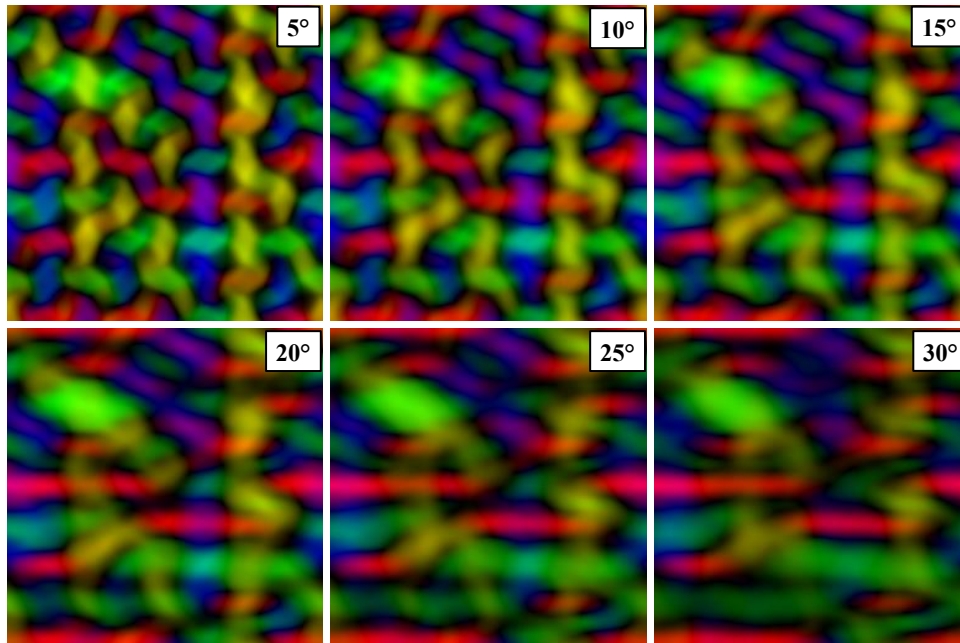


Figure 4.17: Color induction maps showing beam/sample tilt effect on magnetic contrast of the nano-chessboard structure as the beam is tilted around the x -axis, beam tilt angle marked in each figure.

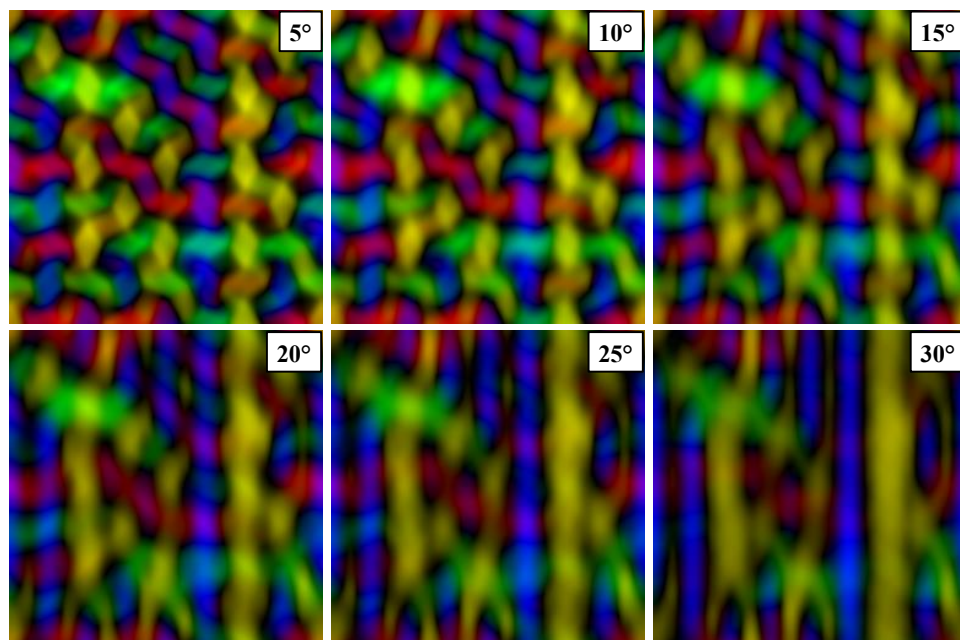


Figure 4.18: Color induction maps showing beam/sample tilt effect on magnetic contrast of the nano-chessboard structure as the beam is tilted around the y -axis, beam tilt angle marked in each figure.

4.6 Comparison of Experimental and Simulated Images

Fig. 4.19 compares a simulated Fresnel under-focus image with an experimental Fresnel under-focus image; both images show S-shaped domain walls. However, the simulated image shows domain walls at both the phase boundaries inside L_{10} - L_{12} - L_{10} three-particle system (green arrows inside rectangular box) while the experimental image shows only one domain wall for L_{10} - L_{12} - L_{10} system, as explained in Section 4.4. This can be understood since the simulation is done for a relatively large L_{12} tile size of 36 nm while the experimental images show L_{12} tiles of the order of 5-10 nm. In reality, two domain walls cannot be accommodated in such a small space as this will lead to an increased exchange energy as well as magneto-crystalline anisotropy energy, making the magnetic system unstable. Nevertheless, a reasonable agreement can be seen between the two images.

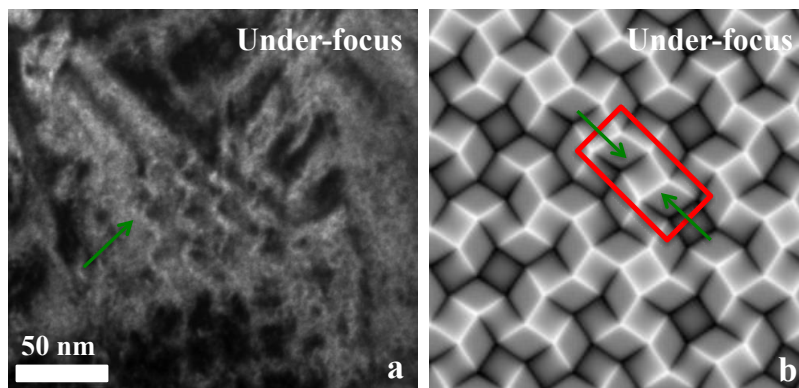


Figure 4.19: Comparison of Lorentz Fresnel images: (a) Experimental image, green arrow points to repetitive S-shaped domain walls, (b) Simulated image, red box encloses a L_{10} - L_{12} - L_{10} three particle system, green arrows point to two domain walls within this system.

Fig. 4.20 compares a phase reconstructed color map simulated at 15° beam tilt with an experimentally obtained color map of Specimen S-40. Both images show a vortex-type magnetic configuration. The simulated image also explains the non-uniform contribution of yellow-red-

blue-green colors seen in the experimental color map. It should be emphasized that a direct comparison between the two images should not be made since the simulation considers nano-chessboards of one crystallographic orientation perfectly oriented along [001] zone axis, with tiles of uniform sizes and shapes while the real chessboard is more complex owing to variability in tile sizes and shapes, presence of nano-chessboards along all the three crystallographic axes, and a random orientation of the sample.

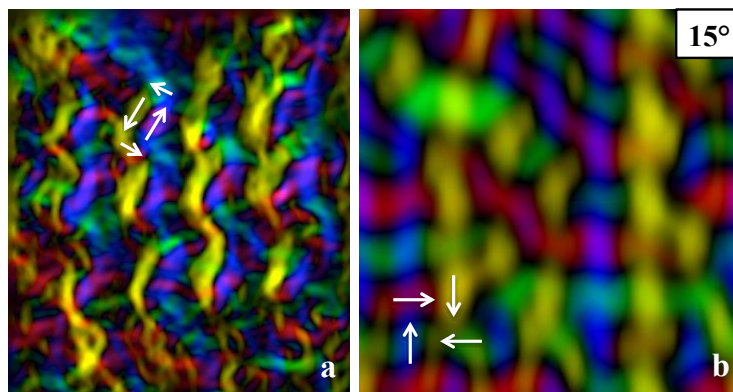


Figure 4.20: Comparison of Phase reconstructed color induction maps: (a) Experimental image, (b) Simulated image. White arrows in both images show vortex-type magnetic configuration.

Fig. 4.21 compares another simulated Lorentz image, simulated at 25° beam tilt, with the experimental Lorentz images of Specimen S-40. A similar type of contrast can be seen in the Fresnel images, phase maps and color maps. As can be seen here, a large relative sample/beam orientation can lead to a highly non-uniform in-plane projection of magnetic contrast which is clearly visible in both the experimental and simulated color maps.

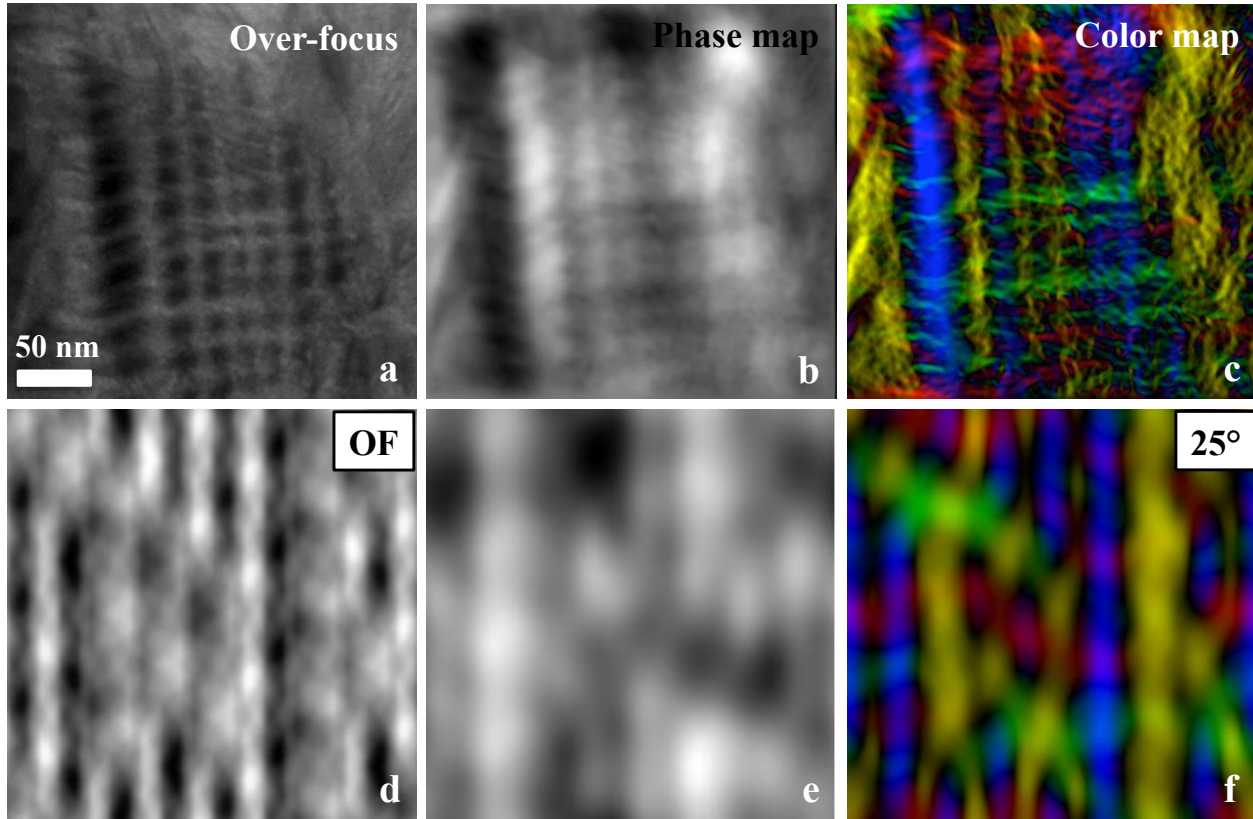


Figure 4.21: Comparison of experimental (above) and simulated images (below): (a) & (d) Over-focus Fresnel images, (b) & (e) Phase maps, (c) & (f) Color induction maps.

Fig. 4.22 shows experimental Lorentz images from another Specimen S-80. Both the image series can be seen showing zig-zag domain walls as well as vortex-type magnetic induction configurations. However, the color maps show elongated or non-uniform contrast along certain directions very similar to elongated contrast seen in Fig. 4.17 for beam tilt around x-axis. This provides further confirmation of our results from images simulated at different beam tilts. Hence, a solid correlation between the relative beam-sample orientation and the magnetic contrast in the experimental color induction maps is established.

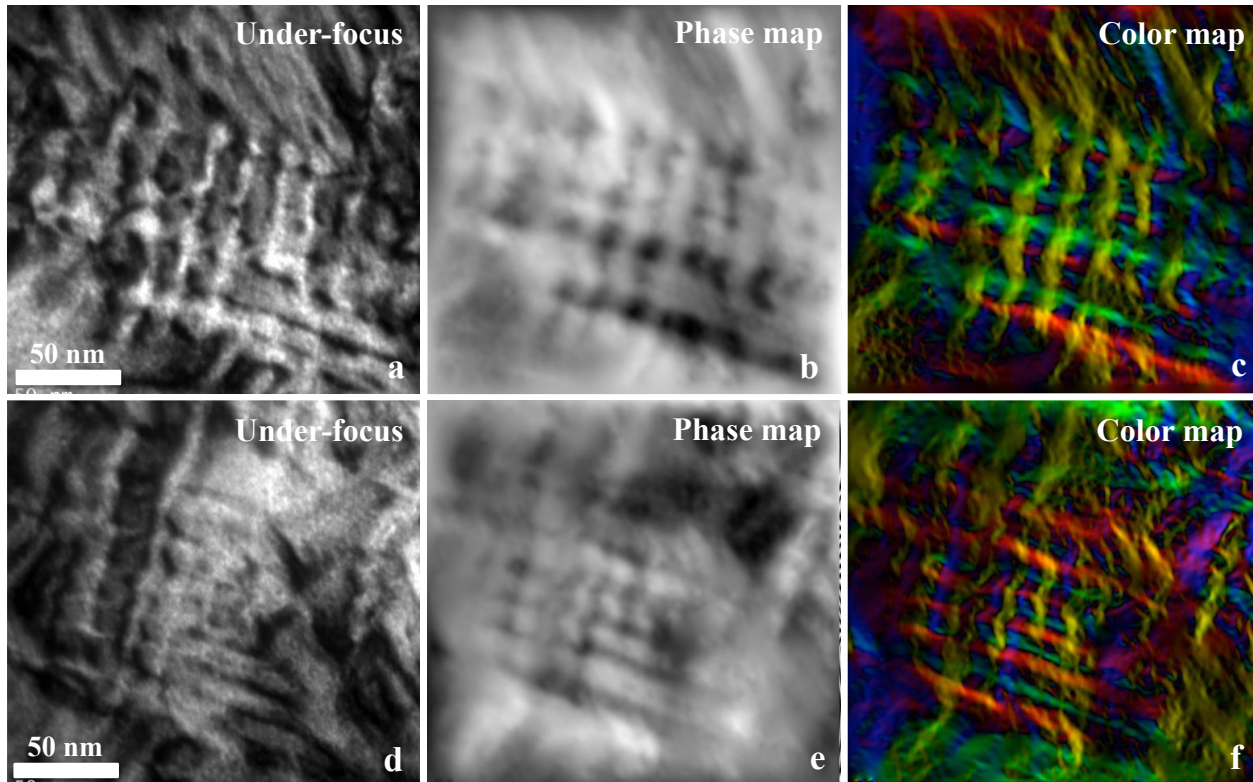


Figure 4.22: Experimental Lorentz images of Specimen S-80: (a) & (d) Under-focus Fresnel images, (b) & (e) Phase maps, (c) & (f) Color induction maps.

4.7 Domain Wall Width Measurement from Lorentz Fresnel Images

4.7.1 Methodology

As explained in Section 3.3.3, the phase shift experienced by an electron, on traveling inside a magnetic thin film of constant thickness t and uniform in-plane magnetic induction \mathbf{B}_{\perp} , changes linearly inside magnetic domains while the slope of the phase shift profile changes continuously across the magnetic domain walls. The range over which this slope changes between two adjacent magnetic domains corresponds to the magnetic domain wall width ' δ '. So, we can

utilize the phase shift profile to measure the domain wall width from the experimental Lorentz Fresnel images as explained below:

1. Set of Fresnel through-focus series images is acquired with the same absolute defocus value $(-\Delta f, 0, \Delta f)$.
2. The Fresnel images are used to retrieve the phase shift map of the electron wave using the transport-of-intensity equation (Equation 3.29).
3. The domain wall width is measured from the first-order derivative of the phase shift profile for the selected domain wall.

This method of determining domain wall width from a phase shift profile has previously been performed by [88] for Ni-Mn-Ga and Fe-Pd ferromagnetic shape memory alloys and a good agreement between theoretical domain wall width and calculated width was found. The domain wall width from Lorentz Fresnel images can also be obtained by the extrapolation method [89]. In this method, several sets of Fresnel images of increasing defocus value are recorded; then, the width of the domain wall contrast in the Fresnel image is plotted against the defocus value. The resulting plot is then extrapolated to zero defocus value and the corresponding width is taken as the domain wall width. At present, we will only apply first method to calculate the domain wall width.

Fig. 4.23(a) shows the phase shift map of a 2D magnetization configuration introduced in Section 3.4.1. The linear phase shift profile is superimposed on the phase shift map. It can be seen that the slope of the phase shift changes smoothly across the domain walls. Fig. 4.23(b) shows a plot of the first order derivative of this profile. The domain wall width can be obtained

using the following steps:

1. Firstly, a tangent at the wall center is drawn, shown by red color in the plot.
2. The tangent is extrapolated to the minimum and the maximum of the plot.
3. The distance between the two intercepts is measured as the domain wall width.

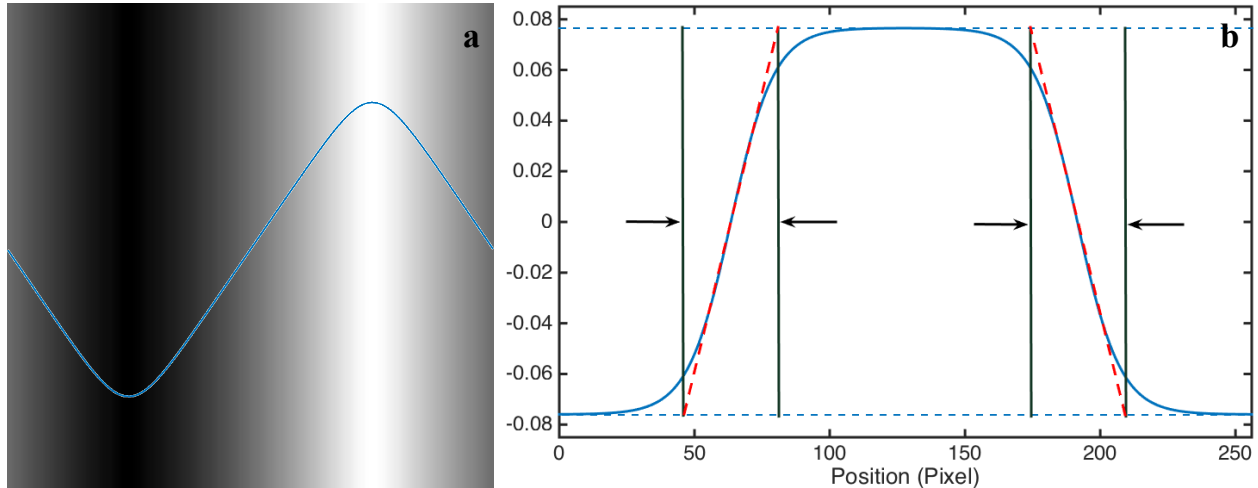


Figure 4.23: (a) Phase map and phase shift profile, (b) Schematic showing calculation of domain wall width from the first order derivative of phase shift profile.

Domain wall widths determined from through-focus series of Fresnel images are compared with the theoretical domain wall width calculated using the experimentally observed K and A .

4.7.2 Domain wall width results

Fig. 4.24 shows phase shift profiles obtained for the regions indicated by white lines (1&2) in the phase reconstructed color map of macro-domain walls in Specimen S-40. The region shown by white line 1 contains two 180° domain walls and the same is reflected in the phase shift profile. The region shown by white line 2 contains a 180° domain wall and a 90° domain wall. Note that the range over which slope of 90° domain wall changes seems to be smaller than the 180°

domain wall, hence the resulting width should also be smaller. The domain wall widths are determined from phase shift profiles as explained in Section 4.7.1. Such measurements are repeated for domain walls in different regions and the average of all the wall widths is taken as the final wall width. Errors due to variations in thickness of the TEM thin foil, alignment of through-focus series, and manual curve fitting of the phase shift profile is also included.

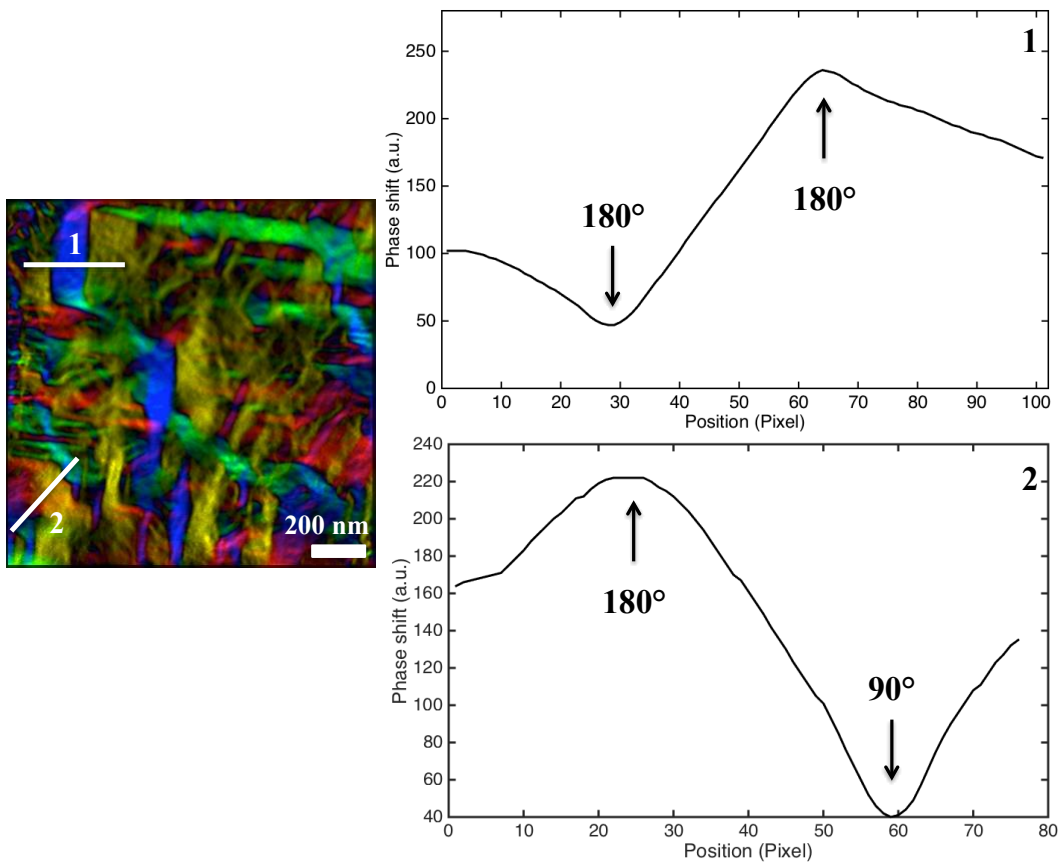


Figure 4.24: Phase shift profile of regions marked by white lines in color induction map of macro-domain walls in Specimen S-40, pixel size is calibrated as 3.70 nm.

Fig. 4.25 shows the phase shift profiles obtained for other microstructures in both the Specimen S-40 and Specimen S-80. The macro-domain walls and the domain walls in the nano-chessboard structure largely yielded smooth phase shift profiles. However, it was challenging to obtain good

profiles for domain walls in the tweed microstructure and the macro-twinned structure because of multiple overlapping contrasts from domain walls tilted at various angles and randomly oriented magnetizations. The domain wall widths obtained for different microstructures are summarized in Table 4.4.

Theoretical magnetic domain wall widths are also calculated using the domain wall width definitions: $\delta=\pi\sqrt{A/K}$ and $\delta=2\sqrt{A/K}$. The second definition is usually applied to domain wall calculations from Lorentz TEM [49]. In addition, wall widths are calculated for two separate sets of exchange stiffness constant (A) and anisotropy constant (K). ' A ' and ' K ' for equiatomic L1₀ CoPt alloy [35] are shown in 2nd row of the table while ' A ' and ' K ' for Co₄₀Pt₆₀ alloy [12] are shown in 3rd row of the table. The experimental wall widths obtained for domain walls in macro-twins, coarse L1₀ grains, and tweed structure match well within the error limit with the theoretical domain wall width of Co₄₀Pt₆₀ alloy while that for domain walls in nano-chessboards matches well with the theoretical domain wall width of an equiatomic CoPt alloy.

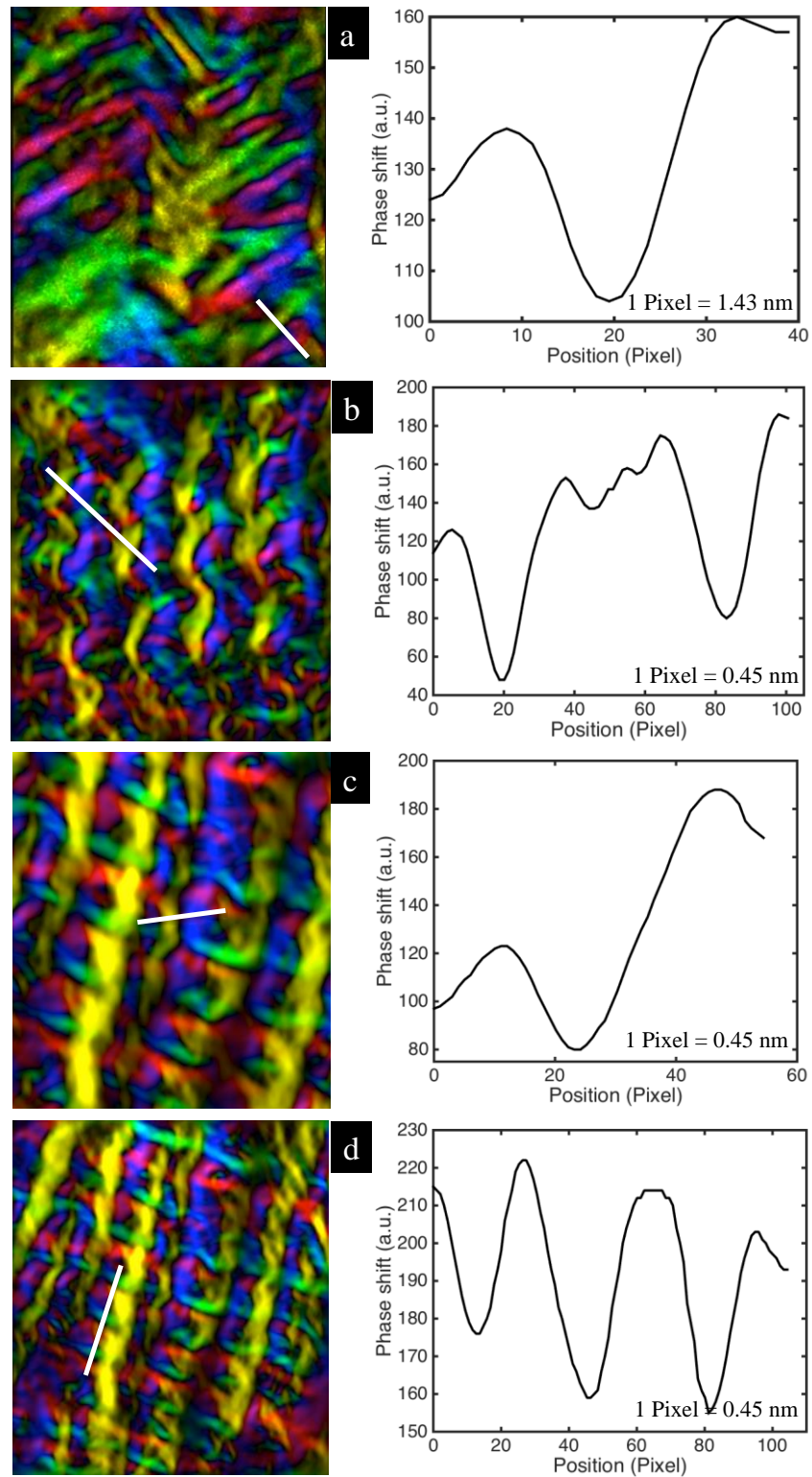


Figure 4.25: Color induction maps and phase shift profiles: (a) 180° domain wall in macro-twins in Specimen S-40, (b) 180° domain walls in nano-chessboard in Specimen S-40, (c) 180° domain wall in nano-chessboard in Specimen S-80, (d) 90° domain walls in nano-chessboard in Specimen S-80. Pixel size shown in each figure.

Table 4-4: Theoretical and experimental magnetic domain wall widths of Co₄₀Pt₆₀ alloys.

A (J/m) K (J/m ³)	Theoretical domain wall width, δ (nm)		Microstructure	Wall type	Experimental domain wall width (nm)	
	$\pi\sqrt{A/K}$	$2\sqrt{A/K}$			S-40	S-80
CoPt $A=1.01\times 10^{-11}$ $K=4.9\times 10^6$	4.5	2.86	Nano-chessboard	180°	3.35 ± 2	4.29 ± 2
				90°	-	3.27 ± 1
			Nano-chessboard	Sideways 180°	3.76 ± 2	-
Co ₄₀ Pt ₆₀ $A=2.5\times 10^{-11}$ $K=1.5\times 10^6$	12.82	8.16	Macro-twins	180°	8.2 ± 3	-
			Coarse L1 ₀ grains	180°	23 ± 7.5	-
				90°	15.02 ± 4.5	-
			Tweed	-	-	20.44 ± 5

Deviations of experimental wall widths from theoretical wall widths and different wall widths for different microstructures can be explained on the basis of following points:

1. Differences in microstructure within a sample indicate a local inhomogeneity in composition, chemical ordering, and/or thermal history. This, in turn, will give rise to varying degrees of magneto-crystalline anisotropy (K) across different regions of the sample. For example, a tweed structure indicates partial ordering or incomplete annealing of the sample. In this case, the magnetic anisotropy should be different as compared to

the well-grown $L1_0$ variants or the fully ordered nano-chessboard structure. Consequently, the magnetic domain wall width, which depends on the combined effect of magneto-crystalline anisotropy and exchange energy, will be different for different microstructures.

2. The theoretical domain wall width is calculated using ' K ' and ' A ' obtained for a bulk sample, which in reality should contain all types of microstructures. The bulk magnetic anisotropy can thus be thought of as an average of all the different anisotropies existing in a single sample. Hence, a deviation of the experimental domain wall width from the theoretical domain wall width can be explained.
3. A part of the error value of domain wall width can be ascribed to a contribution from Lorentz Fresnel images. This is a result of the sample not being perfectly oriented along a zone axis, so that the magnetic domain wall is tilted with respect to the electron beam. The Fresnel images record the projection of a domain wall on the x - y plane, assuming the electron beam travels along z -axis. As a result, a tilted domain wall will give a wrong projection of the actual wall width on the x - y plane. Additionally, microscope aberrations also contribute some error to the phase shift hence the wall width.
4. As shown previously, the small length-scale of $L1_0$ and $L1_2$ tiles of the order of 5-30 nm leads to the formation of an inter phase magnetic domain wall or "IPMDW". The theoretical wall width for this $Co_{40}Pt_{60}$ alloy is around 8-12 nm. It is highly improbable that a wall width of this size can be accommodated inside the $L1_0$ - $L1_2$ nano-chessboard. Additionally, other magnetic phenomena, such as exchange coupling, are also expected between the hard $L1_0$ and the soft $L1_2$ phases, which could considerably change the magnetic environment. The domain wall widths in the nano-chessboards are unusually

small as a result. A very small domain wall width also indicates a higher degree of magneto-crystalline anisotropy in the nano-chessboard structure. This should potentially play a crucial role in determining the coercivity of these alloys.

Apart from the deviations discussed above, differences in wall widths between 90° domain walls and 180° domain walls are also observed. This can be explained using Fig. 4.26. It is assumed that the magnetization angle rotates by a constant angle φ from one atom to the adjacent atom. If it requires a total of $N+1$ atoms or, alternatively, N lattice spacings, for the magnetization to rotate smoothly from one 180° magnetic domain to the other 180° magnetic domain, then following this logic a total of $N/2$ lattice spacings should be required for a rotation of 90° from one domain to the other domain. This explains the difference in the wall thickness obtained for the two profiles. In our case, δ_{180} is greater than δ_{90} , however it is not exactly twice δ_{90} . This suggests that additional magnetic interactions/wall energetics need to be taken into account in the calculation of the theoretical width of a 90° domain wall.

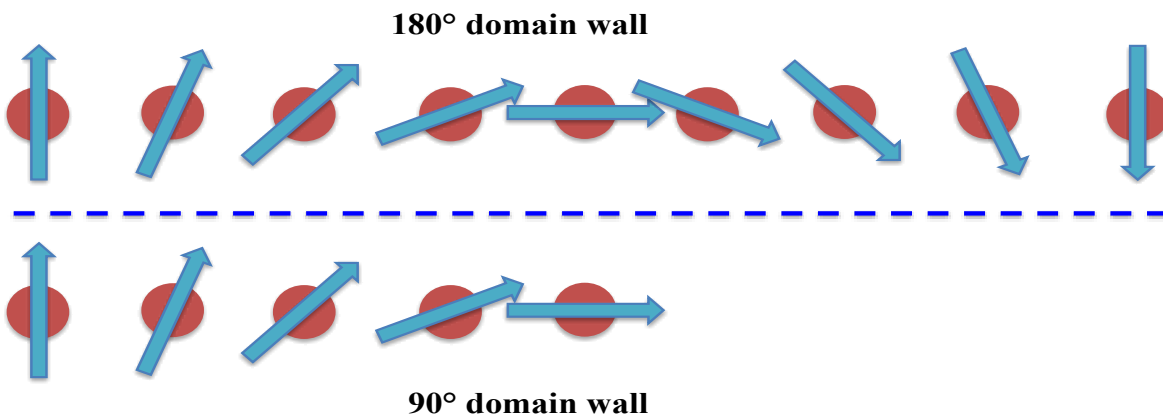


Figure 4.26: Schematic showing rotation of magnetization across a 180° domain wall and a 90° domain wall.

5 Conclusions and Future Work

The interaction of magnetic domain walls and microstructural features was studied and analyzed for Co-Pt alloys for the first time. In particular, we investigated the magnetic domain structure of near-eutectoid $\text{Co}_{40}\text{Pt}_{60}$ alloys by utilizing the Lorentz TEM technique, conventional TEM imaging, phase reconstruction, and image simulations based on micro-magnetic models. This alloy transforms into a unique self-assembled nano-chessboard structure containing $L1_0$ hard magnetic phase and $L1_2$ soft magnetic phase, upon suitable thermal treatments and processing. It has a great potential for high energy density magnetic storage and permanent magnet applications due to the “expected” exchange coupling between the hard and the soft phases at a length-scale of few nano-meters.

Spherical aberration correction in the Lorentz TEM imaging mode was exploited to resolve the nano-scale magnetic features. We have characterized magnetic domain structures associated with different crystallographic microstructures, including tweed structure, macro-twinned structure, coarse $L1_0$ plates, and the nano-chessboard structure in two $\text{Co}_{40}\text{Pt}_{60}$ alloys that were subjected to different annealing treatments. The magnetization configuration of the magnetic domains was deduced from the phase reconstruction of Lorentz Fresnel images. The magnetic easy axes of macro-twinned $L1_0$ plates, $L1_0$ variants and $L1_2$ variants were confirmed by comparing them with the conventional TEM images. Magnetic domain structures of the two samples were

compared with the observed bulk magnetic properties. We also simulated Lorentz Fresnel images and magnetic induction maps in order to appropriately interpret the image contrast associated with the magnetic domain walls in the nano-chessboard structure. In addition, we measured the magnetic domain wall widths of domain walls observed in each of the magnetic domain structures, using the phase shift profile technique. A correlation between the experimentally obtained domain wall widths and magneto-crystalline anisotropies of different microstructures/phases was drawn. The summary of conclusions found in this investigation is discussed in Section 5.1. A potential future work plan for this material is presented in Section 5.2.

5.1 Conclusions

1. Although both the $\text{Co}_{40}\text{Pt}_{60}$ TEM samples (S-40 and S-80) were expected to consist of the nano-chessboard structure throughout, other microstructures e.g. tweed, macro-twinned plates, and coarsened L1_0 plates were also observed. This gave us an opportunity to study and compare magnetic domain walls across different microstructures. The S-40 sample, which was cooled at a slower rate and annealed for a higher time, contained nano-chessboard structure with tiles of the order of 10-30 nm, macro-twinned plates, and coarse L1_0 plates in the L1_2 matrix. The S-80 sample, which was cooled at a higher rate and annealed for lesser time, contained nano-chessboard structure with tiles of the order of 5-15 nm, tweed microstructure, and coarse L1_0 plates in the L1_2 matrix. From these observations, it was concluded that the inhomogeneity in composition and temperature across the samples might have given rise to different microstructures. Additionally, the tweed microstructure was only observed in S-80 while a coarser microstructure was

observed in S-40, this was consistent with the heat treatments, as the tweed structure did not have sufficient time to transform into a coarser microstructure.

2. The macro-twinned structure in S-40 showed several 180° and 90° domain walls that were separating magnetic domains magnetized in different directions. Fine twins were also observed inside the macro-twin bands. The macro-twin boundaries were observed to coincide with 90° magnetic domain walls while the micro-twin boundaries separated magnetic domains with opposite magnetization direction. The magneto-crystalline anisotropy of $L1_0$ tetragonal phase was found to play an important role in dictating the magnetic domain structure of individual twins. The magnetization inside various twins was aligned according to the easy axis of magnetization of the $L1_0$ phase.
3. The coarsened $L1_0$ plates contained straight 180° domain walls conforming to the fact that the $L1_0$ tetragonal phase is a hard uniaxial magnetic phase. The coarsened $L1_2$ grains with $\langle 100 \rangle$ axes as the easy magnetic axes were seen exhibiting a circular magnetization configuration or vortex-type magnetic structure in order to minimize the magnetostatic energy.
4. The tweed structure in S-80 showed several 90° domain walls and it was concluded that these domain walls coincide with the $L1_0$ boundaries between different $L1_0$ variants since the magnetic easy axes of two different $L1_0$ variants are perpendicular to each other (e.g. $[010]$ and $[001]$).
5. In both samples S-40 and S-80, the nano-chessboard structure exhibited a circular magnetic configuration or vortex type magnetic structure. Anti-vortex magnetic structures were found to lie between the two vortex structures. By comparing the Lorentz TEM results with the conventional TEM results, phase shift simulation results, and

theoretical critical size for single magnetic domain particle, it was concluded that the $L1_0$ tiles exist as single magnetic domains with their magnetization directions oriented along the easy axes/c-axes, in the nano-chessboard structure. The alternate easy axes in the neighboring $L1_0$ tiles led to a magnetic arrangement in which the magnetization directions were aligned in such a way that they formed a circular loop in order to minimize the magneto-static energy as well as the magneto-crystalline anisotropy energy. However, the change in magnetization between adjacent $L1_0$ tiles (90° or 180°) necessitated the formation of a domain wall across the $L1_2$ tile/region between the two $L1_0$ tiles to reduce the exchange energy. This type of magnetic domain wall has never been reported before and we propose that this wall is an Inter Phase Magnetic Domain Wall (IPMDW). It was also hypothesized that the magnetization of the soft $L1_2$ tiles is strongly influenced by the hard $L1_0$ tiles due to their close proximity in the nano-chessboard structure at a length scale of few nanometers, which resulted in a smooth transition of magnetization across the $L1_0$ - $L1_2$ phase boundaries and the evolution of IPMDW. As the length-scale of $L1_0$ - $L1_2$ tiles decreased below a critical value, the tiles acquired a perfect vortex magnetic structure. The formation of IPMDW was based on three crucial factors: firstly, the two phases involved should have a coherent interface to ensure a smooth transition of magnetization from one phase to the other phase; secondly, one of the phases needs to be a strong hard phase to be able to influence the magnetization of the soft phase; thirdly, both phases should be below their critical sizes of single magnetic domain particle so that a domain wall does not nucleate within each particle.

6. The simulation of magnetic phase shifts and Lorentz Fresnel images at different beam

tilts inside TEM showed that the contrast of Lorentz Fresnel images and the phase reconstructed maps can change substantially with a change in relative sample-beam orientation inside TEM. A good agreement between the beam-tilted simulated magnetic induction maps and experimental induction maps of the nano-chessboard structure was found.

7. In sample S-40, magnetic domain wall widths (δ) from phase shift profiles were determined to be 3.35 ± 2 nm for 180° domain walls in the nano-chessboard structure, 8.2 ± 3 nm for 180° domain walls in the macro-twinned structure, 23 ± 7.5 nm for 180° domain walls in coarsened grains and 15.02 ± 4.5 nm for 90° domain walls in coarsened grains. In sample S-80, magnetic domain wall widths (δ) were determined to be 4.29 ± 2 nm for 180° domain walls in the nano-chessboard structure, 3.27 ± 1 nm for 90° domain walls in the nano-chessboard structure, and 20.44 ± 5 nm for tweed structure. The domain walls in the nano-chessboard structure were recorded using aberration corrected Lorentz TEM hence errors in these measurements should be minimal. A comparison of the experimental domain wall widths with the theoretical domain wall widths ($\delta = 8-12$ nm) obtained using bulk magneto-crystalline anisotropy (K) and exchange energy (A) constants showed a good agreement within the error range. However, the domain wall widths in the nano-chessboard structure were found to be exceptionally low as compared to the theory and other microstructures. This could be understood since the $L1_0$ and $L1_2$ tiles in the nano-chessboard structure are not large enough to support domain walls of higher thicknesses as suggested by theory. Additionally, it was concluded that the differences in domain wall widths across different microstructures were a result of changes in magneto-crystalline anisotropy across different microstructures. A very low

domain wall width in the nano-chessboard structure suggests a very high magneto-crystalline anisotropy in this region, which should theoretically result in a higher coercivity.

8. The comparison of magnetic coercivity (experimentally obtained) of two samples with the observed magnetic domain structures showed that a higher coercivity in S-80 could be ascribed to the tweed structure and the fine nano-chessboard structure. During the magnetization process, the magnetic domain walls will encounter multiple hindrances in the form of $L1_0$ variant boundaries in a tightly packed tweed structure as opposed to relatively lesser hindrances in the macro-twinned structure in S-40 sample. The magnetic domain walls coinciding with these crystallographic boundaries are usually frozen/pinned and require a high magnetic field to unpin the domain walls from these boundaries. Additionally, a large number of IPMDW in S-80, due to finer nano-chessboards, should also play a crucial role in contributing a higher coercivity to the S-80 sample. The IPMDWs cannot move past $L1_0$ - $L1_2$ phase boundaries hence rotation of magnetization is the only way to magnetize the regions of nano-chessboard structure, which would require a very high magnetic field consequently resulting in higher coercivity.

5.2 Future Work

1. Apart from the nano-chessboard structure in both the $Co_{40}Pt_{60}$ samples, all the other magnetic microstructures were recorded in an un-corrected Lorentz TEM, which resulted in images with poor resolution. The un-corrected Lorentz TEM has a very high spherical aberration giving rise to a good amount of error in the reconstructed phase shift from Fresnel images which often leads to large errors in the measurements of domain wall

widths using phase shift profiles. Thus, it would be beneficial to capture domain wall images in other regions using spherical aberration correction to minimize the errors in wall width calculations as well as interpretation of reconstructed induction maps.

2. While domain wall width measurements were obtained using the reconstructed phase shift, it will be interesting to do similar calculations using the extrapolation method. In this method, several sets of Fresnel images of increasing defocus value are recorded, then the width of the domain wall contrast in the Fresnel image is plotted against the defocus value. The resulting plot is then extrapolated to zero defocus value and the corresponding width is taken as the domain wall width. However, it will be challenging to apply this method for the nano-chessboard structure since the domain walls are barely/faintly visible in the defocussed images and also due to very fine magnetic domains/domain walls. It will also be difficult to apply this method to the tweed and twinned microstructure since multiple overlapping contrasts from various domain walls are seen in the Fresnel images. However, this method can be applied to the coarse $L1_0$ and $L1_2$ grains, which showed relatively wide domain walls and large magnetic domains. The calculations obtained by this method will be useful to evaluate the method based on phase profiles.
3. The present simulation considered a very idealized nano-chessboard structure. It is important to simulate images that are closer to the real nano-chessboard structures. Keeping this in mind, nano-chessboards with tiles of different sizes can be simulated. Nano-chessboards from other orientations can also be included in the simulation. These studies will allow the comparison of the simulated images directly with experimental images.

4. There has been no study on the behavior of magnetic domain walls in response to an external magnetic field in Co-Pt alloys. The movement of domain walls is expected to be different in different microstructures. The pinning effect of various boundaries ($L1_0$ variant boundaries, twin boundaries) can be evaluated by tracking the magnetic field required to move the domain walls away from these boundaries. This could be done in aberration corrected microscope by slightly exciting the objective lens and by tilting the sample to introduce an in-plane magnetic field. This study will further the understanding of interaction between domain walls and the microstructural features.
5. The expected “exchange coupling” between the hard and the soft phases in the nano-chessboard structure is not proven clearly at this time. The recent work by [58] has thrown some light on the behavior of the two phases in the presence of an external magnetic field, using First Order Reversal Curves. They also showed the degree of exchange coupling between the two phases using micro-magnetic simulations [14]. However, there is no data on experimental magnetic microstructural studies to validate their results. It will be thoughtful to do in-situ (magnetic field) imaging in the Lorentz TEM mode to record the real-time behavior of magnetic domains in individual phases. This study could provide more insights about the exchange-coupling phenomenon in this alloy.

Bibliography

- [1] Dhatfield, “www.wikipedia.com,” 2008.
- [2] M. De Graef, *Introduction to Conventional Transmission Electron Microscopy*. Cambridge University Press, 2003.
- [3] J. M. D. Coey, “Hard magnetic materials: A perspective,” *IEEE Trans. Magn.*, vol. 47, no. 12, pp. 4671–4681, 2011.
- [4] B. Zhang and W. A. Soffa, “The structure and properties of L1₀ ordered ferromagnets: Co-Pt, Fe-Pt, Fe-Pd and Mn-Al,” *Scr. Metall. Mater.*, vol. 30, no. 6, pp. 683–688, Mar. 1994.
- [5] K. Watanabe and H. Masumoto, “On the High-Energy Product Fe-Pt Permanent Magnet Alloys,” *Trans. Japan Inst. Met.*, vol. 24, no. 9, pp. 627–632, 1983.
- [6] J. M. Sanchez, J. L. Moran-Lopez, C. Leroux, and M. C. Cadeville, “Magnetic properties and chemical ordering in Co-Pt,” *J. Phys. Condens. Matter*, vol. 1, no. 2, p. 491, 1989.
- [7] M. C. Cadeville, C. E. Dahmani, and F. Kern, “Magnetism and spatial order in Ni-Pt and Co-Pt alloys,” *J. Magn. Magn. Mater.*, vol. 54–57, no. PART 2, pp. 1055–1056, 1986.
- [8] R. Skomski and J. M. D. Coey, “Giant energy product in nanostructured two-phase magnets,” *Phys. Rev. B*, vol. 48, no. 21, pp. 15812–15816, 1993.
- [9] M. E. McHenry and D. E. Laughlin, “Nano-scale materials development for future magnetic applications,” *Acta Mater.*, vol. 48, no. 1, pp. 223–238, 2000.
- [10] F. Liu *et al.*, “Exchange-coupled nanocomposites: chemical synthesis, characterization and applications,” *Chem. Soc. Rev.*, vol. 43, no. 23, pp. 8098–8113, 2014.
- [11] C. Leroux, A. Loiseau, D. Broddin, and G. Vantendeloo, “Electron microscopy study of the coherent two-phase mixtures L1₀ + L1₂, in Co-Pt alloys,” *Philos. Mag. Part B*, vol. 64, no. 1, pp. 57–82, Jul. 1991.
- [12] P. Ghatwai, “Structure-Property Relationships in Ordered Co-Pt Alloys of Near-Eutectoid Compositions,” University of Virginia, Charlottesville, VA, 2015.
- [13] Y. Le Bouar, a. Loiseau, and a. G. Khachatryan, “Origin of chessboard-like structures in decomposing alloys. Theoretical model and computer simulation,” *Acta Mater.*, vol. 46, no. 8, pp. 2777–2788, 1998.
- [14] E. P. Vetter *et al.*, “Lengthscale effects on exchange coupling in Co-Pt L1₀ + L1₂ nanochessboards,” *Apl Mater.*, vol. 4, no. 9, 2016.
- [15] L. Wang, D. E. Laughlin, Y. Wang, and A. G. Khachatryan, “Magnetic domain structure

- of Fe-55 at.%Pd alloy at different stages of atomic ordering,” *J. Appl. Phys.*, vol. 93, no. 10 3, pp. 7984–7986, 2003.
- [16] A. Budruk, C. Phatak, A. K. Petford-Long, and M. De Graef, “In situ lorentz TEM magnetization study of a Ni-Mn-Ga ferromagnetic shape memory alloy,” *Acta Mater.*, vol. 59, no. 12, pp. 4895–4906, 2011.
- [17] A. Budruk, “Microstructural Investigations of Defects and Domains in Magnetic Shape Memory Alloys,” Carnegie Mellon University, 2012.
- [18] W. A. Soffa, D. E. Laughlin, and N. Singh, “Interplay of ordering and spinodal decomposition in the formation of ordered precipitates in binary fcc alloys: Role of second nearest-neighbor interactions,” *Philos. Mag.*, vol. 90, no. 1–4, pp. 287–304, 2010.
- [19] D. A. Porter and K. E. Easterling, *Phase Transformations in Metals and Alloys*, 2nd ed. Chapman & Hall, 1992.
- [20] E. D. Cantando, “Combined Reactions Thermomechanical Processing Applied to Ferromagnetic Fe-Pd Binary Alloys,” University of Virginia, 2011.
- [21] T. Klemmer, D. Hoydick, H. Okumura, B. Zhang, and W. A. Soffa, “Magnetic hardening and coercivity mechanisms in L10 ordered FePd ferromagnets,” *Scr. Metall. Mater.*, vol. 33, no. 10–11, pp. 1793–1805, 1995.
- [22] Q. F. Xiao, E. Brück, Z. D. Zhang, F. R. De Boer, and K. H. J. Buschow, “Phase transformation and magnetic properties of bulk CoPt alloy,” *J. Alloys Compd.*, vol. 364, no. 1–2, pp. 64–71, 2004.
- [23] F. A. Hansen, M. Shunk, *Constitution of binary alloys*. McGraw Hill: New York, 1958.
- [24] Y. S. Shur, L. M. Magat, G. V. Ivanova, A. I. Mitsek, A. S. Yermolenko, and O. A. Ivanov, “Nature of the coercive force of a cobalt-platinum alloy in an ordered state,” *Fiz. Met. i Metalloved.*, vol. 26, p. 241, 1968.
- [25] D. Weller *et al.*, “High K/sub u/materials approach to 100 Gbits/in/sup 2,” *IEEE Trans. Magn.*, vol. 36, no. 1, pp. 10–15, 2000.
- [26] W. D. Callister, *Materials Science and Engineering: An Introduction*, 7th ed. John Wiley & Sons, Inc., 2007.
- [27] C. Leroux, M. C. Cadeville, V. Pierron-Bohnes, G. Inden, and F. Hinz, “Comparative investigation of structural and transport properties of L1 0 NiPt and CoPt phases; the role of magnetism,” *J. Phys. F Met. Phys.*, vol. 18, no. 9, pp. 2033–2051, Sep. 1988.
- [28] D. E. Laughlin, K. Srinivasan, M. Tanase, and L. Wang, “Crystallographic aspects of L10 magnetic materials,” *Scr. Mater.*, vol. 53, no. 4, pp. 383–388, 2005.
- [29] M. De Graef and M. E. McHenry, *Structure of Materials: An Introduction to Crystallography, Diffraction, and Symmetry*. Cambridge University Press, 2007.
- [30] P. Andreatza, V. Pierron-bohnes, F. Tournus, and C. Andreatza-vignolle, “Structure and order in cobalt / platinum-type nanoalloys : from thin films to supported clusters,” *Surf. Sci. Rep.*, vol. 70, no. 2, pp. 188–258, 2015.
- [31] A. S. Darling, “Cobalt -Platinum Alloys,” *Platin. Met. Rev.*, vol. 7, no. 3, pp. 96–104, 1963.

- [32] Y. Ni and A. G. Khachatryan, "From chessboard tweed to chessboard nanowire structure during pseudospinodal decomposition.," *Nat. Mater.*, vol. 8, no. 5, pp. 410–414, 2009.
- [33] B. Zhang and W. A. Soffa, "Magnetic domains and coercivity in polytwinned ferromagnets," *Phys. Status Solidi*, vol. 131, no. 2, pp. 707–725, 1992.
- [34] L. Wang, Z. Fan, and D. E. Laughlin, "Trace analysis for magnetic domain images of L10 polytwinned structures," *Scr. Mater.*, vol. 47, no. 11, pp. 781–785, 2002.
- [35] L. Wang, "Atomic Ordering, Magnetic Domain Structure and Magnetic Properties of L10 Type Ferromagnets," Carnegie Mellon University, 2004.
- [36] B. Zhang, M. Lelovic, and W. A. Soffa, "The formation of Polytwinned Structures in Fe-Pt and Fe-Pd Alloys," *Scr. Metall. Mater.*, vol. 25, pp. 1577–1582, 1991.
- [37] C. Leroux, A. Loiseau, C. Cadeville, M. D. Broddin, and G. Van Tendeloo, "Order-disorder transformation in Co₃₀Pt₇₀ alloy: evidence of wetting from the antiphase boundaries Order-disorder transformation in Co₃₀, Pt₇₀ alloy: evidence of wetting from the antiphase boundaries," *J. Phys. Condens. Matter*, vol. 3479, pp. 3479–3495, 1990.
- [38] Y. Ni and A. G. Khachatryan, "Mechanism and conditions of the chessboard structure formation," *Acta Mater.*, vol. 56, no. 16, pp. 4498–4509, 2008.
- [39] J. M. D. Coey, *Magnetism and Magnetic Materials*. Cambridge University Press, New York, 2010.
- [40] B. D. Cullity and C. D. Graham, *Introduction to Magnetic Materials*. John Wiley & Sons, Inc., 2009.
- [41] R. C. O'Handley, *Modern Magnetic Materials: Principles and Applications*. John Wiley & Sons, Inc., 2000.
- [42] M. E. McHenry and D. E. Laughlin, "Magnetic Properties of Metals and Alloys," in *Physical Metallurgy*, vol. 1, Elsevier, 2014, pp. 1881–2008.
- [43] F. Bolzoni, F. Leccabue, R. Panizzieri, and L. Pareti, "Magnetocrystalline anisotropy and phase transformation in Co-Pt alloy," *IEEE Trans. Magn.*, vol. 20, no. 5, pp. 1625–1627, 1984.
- [44] N. I. Vlasova, G. S. Kandaurova, and N. N. Shchegoleva, "Effect of the polytwinned microstructure parameters on magnetic domain structure and hysteresis properties of the CoPt-type alloys," *J. Magn. Magn. Mater.*, vol. 222, no. 1–2, pp. 138–158, 2000.
- [45] M. E. McHenry and D. E. Laughlin, "Magnetic Moment and Magnetization," in *Characterization of Materials*, Hoboken, NJ, USA: John Wiley & Sons, Inc., 2012.
- [46] W. Grange, I. Galanakis, M. Alouani, M. Maret, J.-P. Kappler, and A. Rogalev, "Experimental and theoretical x-ray magnetic-circular-dichroism study of the magnetic properties of Co₅₀Pt₅₀ thin films," *Phys. Rev. B*, vol. 62, no. 2, pp. 1157–1166, Jul. 2000.
- [47] M. E. McHenry, J. M. MacLaren, and D. P. Clougherty, "Monolayer magnetism of 3d transition metals in Ag, Au, Pd, and Pt hosts: Systematics of local moment variation," *J. Appl. Phys.*, vol. 70, no. 10, pp. 5932–5934, 1991.
- [48] J. M. MacLaren, R. R. Duplessis, R. A. Stern, and S. Willoughby, "First principles calculations of FePt, CoPt, Co₃Pt, and Fe₃Pt alloys," *IEEE Trans. Magn.*, vol. 41, no. 12,

- pp. 4374–4379, Dec. 2005.
- [49] A. Hubert and R. Schafer, *Magnetic Domains: The Analysis of Magnetic Microstructures*. Springer, 2009.
- [50] D. Sellmyer and R. Skomski, *Advanced Magnetic Nanostructures*. Springer, 2006.
- [51] S. S. A. Razee, J. B. Staunton, F. J. Pinski, B. Ginatempo, and E. Bruno, “Magnetic anisotropies of Ni–Pt and Co–Pt alloys,” *J. Appl. Phys.*, vol. 83, no. 11, pp. 7097–7099, 1998.
- [52] S. Ueda, M. Mizuguchi, Y. Miura, J. G. Kang, M. Shirai, and K. Takanashi, “Electronic structure and magnetic anisotropy of L1₀-FePt thin film studied by hard x-ray photoemission spectroscopy and first-principles calculations,” *Appl. Phys. Lett.*, vol. 109, no. 4, p. 42404, 2016.
- [53] B. A. Lilley, “Energies and widths of domain boundaries in ferromagnetics,” *London, Edinburgh, Dublin Philos. Mag. J. Sci.*, vol. 41, no. 319, pp. 792–813, Aug. 1950.
- [54] C. Kittel, “Physical Theory of Ferromagnetic Domains,” *Rev. Mod. Phys.*, vol. 21, no. 4, pp. 541–583, 1949.
- [55] H. Shima *et al.*, “Magnetocrystalline anisotropy energy in L1₀-type CoPt single crystals,” *J. Magn. Magn. Mater.*, vol. 290–291 PA, pp. 566–569, 2005.
- [56] E. F. Kneller and R. Hawig, “The Exchange-Spring Magnet:,” *IEEE Trans. Magn.*, vol. 27, no. 4, pp. 3588–3600, 1991.
- [57] P. Ghatwai, E. Vetter, M. Hrdy, W. A. Soffa, and J. A. Floro, “Evolution of microstructure and magnetic properties in Co-Pt alloys bracketing the eutectoid composition,” *J. Magn. Magn. Mater.*, vol. 375, pp. 87–95, 2015.
- [58] E. Vetter, P. Ghatwai, W. Soffa, and J. Floro, “Evolution of First-Order Reversal Curves during Self-Assembly of the Co_{40.2}Pt_{59.8} Nano-Chessboard Structure,” *IEEE Magn. Lett.*, vol. 6, 2015.
- [59] M. Knoll and E. Ruska, “The Electron Microscope,” *Z. Phys.*, vol. 78, pp. 318–339, 1932.
- [60] Z. Wang *et al.*, “Atom-resolved imaging of ordered defect superstructures at individual grain boundaries,” *Nature*, vol. 479, no. 7373, pp. 380–383, Nov. 2011.
- [61] J. Spence, “Achieving atomic resolution,” *Mater. Today*, vol. 5, no. 3, pp. 20–33, 2002.
- [62] J. N. Chapman, “The investigation of magnetic domain structures in thin foils by electron microscopy,” *J. Phys. D Appl. Phys.*, vol. 17, no. 4, pp. 623–647, 1984.
- [63] F. Bitter, “Experiments on the nature of ferromagnetism,” *Phys. Rev.*, vol. 41, no. 4, pp. 507–515, 1932.
- [64] S. Egelkamp and L. Reimer, “Imaging of magnetic domains by the Kerr effect using a scanning optical microscope,” *Meas. Sci. Technol.*, vol. 1, pp. 79–83, 1990.
- [65] Y. Martin and H. K. Wickramasinghe, “Magnetic imaging by ‘force microscopy’ with 1000 Å resolution,” *Appl. Phys. Lett.*, vol. 50, no. 20, pp. 1455–1457, 1987.
- [66] A. K. Petford-Long and M. De Graef, *Lorentz Microscopy*. John Wiley & Sons, Inc., 2002.

- [67] W. H. Bragg and W. L. Bragg, “The Reflection of X-rays by Crystals,” *Proc. R. Soc. London A*, vol. 88, pp. 428–438, 1913.
- [68] D. B. Williams and C. B. Carter, *Transmission Electron Microscopy: A Textbook for Materials Science*. Springer, 2009.
- [69] K. Tsuno and T. Taoka, “Magnetic-Field-Free Objective Lens around a Specimen for Observing Fine Structure of Ferromagnetic Materials in a Transmission Electron Microscope,” *Jpn. J. Appl. Phys.*, vol. 22, no. 6, pp. 1041–1047, 1983.
- [70] M. De Graef, “Lorentz microscopy: Theoretical basis and image simulations,” in *Experimental Methods in the Physical Sciences*, 36th ed., M. De Graef and Y. Zhu, Eds. 2001, pp. 27–67.
- [71] S. Tandon, “Theoretical and Experimental Study of Shape Effects on Magnetic Nanoparticles using Simulation-Assisted Lorentz Microscopy,” Carnegie Mellon University, 2004.
- [72] Y. Aharonov and D. Bohm, “Further considerations on electromagnetic potentials in the quantum theory,” *Phys. Rev.*, vol. 123, no. 4, pp. 1511–1524, 1961.
- [73] J. D. Jackson, *Classical Electrodynamics*, 2nd ed. Wiley, 1975.
- [74] M. Mansuripur, “Computation of electron-diffraction patterns in Lorentz electron microscopy of thin magnetic films,” *J. Appl. Phys.*, vol. 69, no. 4, pp. 2455–2464, 1991.
- [75] M. Beleggia and Y. Zhu, “Electron-optical phase shift of magnetic nanoparticles I. Basic concepts,” *Philos. Mag.*, vol. 83, no. 8, pp. 1045–1057, 2003.
- [76] M. Beleggia, Y. Zhu, S. Tandon, and M. De Graef, “Electron-optical phase shift of magnetic nanoparticles II. Polyhedral particles,” *Philos. Mag.*, vol. 83, no. 9, pp. 1143–1161, 2003.
- [77] D. Paganin and K. A. Nugent, “Noninterferometric phase imaging with partially coherent light,” *Phys. Rev. Lett.*, vol. 80, no. 12, pp. 2586–2589, 1998.
- [78] A. Bleloch and Q. Ramasse, “Lens Aberrations: Diagnosis and Correction,” in *Aberration-Corrected Analytical Transmission Electron Microscopy*, R. Brydson, Ed. John Wiley & Sons, Ltd., 2011, pp. 55–87.
- [79] M. Haider, H. Rose, S. Uhlemann, E. Schwan, B. Kabius, and K. Urban, “A spherical-aberration-corrected 200 kV transmission electron microscope,” *Ultramicroscopy*, vol. 75, no. 1, pp. 53–60, 1998.
- [80] C. Phatak, “On the use of phase reconstructed vector field electron tomography for the 3-d study of magnetic materials,” 2009.
- [81] P. Ghatwai, “Structure-Property Relationships in Ordered Co-Pt Alloys of Near-Eutectoid Compositions,” University of Virginia, Charlottesville, VA, 2015.
- [82] Y. Le Bouar and A. Loiseau, “Strain-induced microstructure development due to a wetting phenomenon in the Co-Pt system,” *Acta Mater.*, vol. 49, no. 14, pp. 2679–2690, 2001.
- [83] C. Phatak and M. De Graef, “Imaging of Domains and Vortices in Multifunctional Materials,” in *Mesoscopic Phenomena in Multifunctional Materials*, vol. 198, A. Saxena and A. Planes, Eds. Springer Series in Materials Science, 2014, pp. 137–158.

- [84] T. Sannomiya, J. Shi, Y. Nakamura, and O. Nittono, "Correlation between magnetization performance and magnetic microstructure of patterned permalloy films fabricated by microcontact printing," *J. Appl. Phys.*, vol. 96, no. 9, pp. 5050–5055, 2004.
- [85] S. P. Venkateswaran, N. T. Nuhfer, and M. De Graef, "Anti-phase boundaries and magnetic domain structures in Ni₂MnGa-type Heusler alloys," *Acta Mater.*, vol. 55, no. 8, pp. 2621–2636, 2007.
- [86] T. Mehaddene *et al.*, "Lattice dynamics and migration enthalpies in CoPt₃ and FePd," *Phys. Rev. B*, vol. 69, no. 2, p. 24304, Jan. 2004.
- [87] I. Kashyap and M. De Graef, "Magnetic Domain Imaging of Ni-Mn-Ga Heusler Alloys Using Lorentz TEM," *Microsc. Microanal.*, vol. 22, no. S3, pp. 1720–1721, 2016.
- [88] S. Hua, "Magnetic Domain Imaging: A Comparison Between Lorentz Transmission Electron Microscopy and Magnetic Force Microscopy," 2015.
- [89] S. J. Lloyd, J. C. Loudon, and P. A. Midgley, "Measurement of magnetic domain wall width using energy-filtered Fresnel images," *J. Microsc.*, vol. 207, no. 2, pp. 118–128, 2002.